Curvy polymer crystals : Why crystalline lamellae twist during growth

Martin Rosenthal

UNIVERSITÉ DE HAUTE ALSACE

CURVY POLYMER CRYSTALS: WHY CRYSTALLINE LAMELLAE TWIST DURING GROWTH

By
MARTIN ROSENTHAL

Diplomingenieur für Werkstoffwissenschaften
Martin Luther Universität Halle-Wittenberg, Germany
2005

Dissertation
submitted to the Faculty of the
Université de Haute-Alsace
Mulhouse

in partial fulfillment of
the requirements for
the Degree of

DOCTOR OF PHILOSOPHY

June, 2010

Mulhouse

THÈSE

Présentée pour obtenir le titre de

DOCTEUR DE L'UNIVERSITÉ DE
HAUTE-ALSACE

Spécialité :
Chimie des Matériaux

Par
Martin ROSENTHAL

Sujet:

CURVY POLYMER CRYSTALS: WHY CRYSTALLINE LAMELLAE TWIST DURING GROWTH

Composition du jury:

Prof. Dr. Sergei N. CHVALUN: Rapporteur
Dr. habil. Georg BAR: Rapporteur
Prof. Dr. Jean-François GÉRARD: Examinateur
Dr. Patrick DAVIDSON: Examinateur
Dr. Bassel HAIDAR: Examinateur
Dr. Dimitri A. IVANOV: Promoteur

To my Mother

ACKNOWLEDGEMENTS

Most cordially I want to thank my supervisor Dr. Dimitri A. Ivanov for his encouragement, guidance and support throughout my PhD project. I want also to thank him for sharing his scientific knowledge, for his patience, for teaching me how to write scientific proposals, reports and papers, for giving me freedom in my research even if sometimes I was quite away from the final goals of the project. It was really a great chance and always a pleasure for me to work with him. I am also particularly grateful to Dr. Georg Bar for making all this possible by giving me the right direction before starting this challenge. Thank you both of you for being good friends and mentors.

I am grateful to my colleagues, past and present, which were extraordinarily helpful for me. Especially I am deeply indebted to Dr. Denis Anokhin who helped me with structure modeling and sharing the office with me for a long time. I will never forget the "Russian" nights in your kitchen and the exhausting but great moments we had at the ESRF. I also want to thank Dr. Valeriy Luchnikov for the helpful discussions on computer simulations and Yaroslav Odarchenko for measuring the last data point while I was already writing the thesis. I also want to thank Nelly Piazzon for translating the final resume into French.

In addition I want to thank Dr. Wim Bras and Dr. Giuseppe Portale from the Dutch Belgium beam line BM26 (DUBBLE) as well as Dr. Christian Riekel, Dr. Manfred Burghammer and Dr. Richard Davies from the micro-focus beam line ID13 at the ESRF, Grenoble, for providing measuring time and scientific support. I also want to thank Dr. Sérgio Funari from the A2 beamline of the HASYLAB Hamburg for providing measuring time on an exceptionally short notice being extremely valuable to finalize the project.

Apart from my colleagues and collaborators, I would like to thank my family. Especially I want to thank my wife Carola for the permanent support throughout all these years emotionally as well as in the daily life. I also want to thank my brother Stefan and his wife Nadine for giving me such a pleasant time while writing up the thesis. I will never forget the cheerful moments with Tarja and Marvin in your place. I am also grateful to my cousin Ilka and friends together with my unkles whole family for cheering me up and giving me a place to stay when I was crossing Germany in the last month of the writing. You are all part of this thesis.

I would also like to thank the members of my jury for reading this manuscript. I would like to acknowledge financial support from the European Community's "Marie-Curie Actions" under contract MRTN-CT-2004- 504052 [POLYFILM].

PREFACE

The availability of materials has always been one of the main factors determining the human history. As *Rubinstein* and *Colby* nicely put it in their "Polymer Physics" textbook (Oxford 2003): "… history is divided into eras named after the primary materials used: the Stone Age, the Bronze Age and the Iron Age. Similarly, we can assert that in the 20th century we entered the Polymer age. …" However, learning how to use polymers is in many aspects equivalent to understanding their structure-property relationships, which are far from being trivial. In particular, comprehending the molecular details of the hierarchical structure of the semicrystalline polymers can still be considered as the main challenge in the field.

As far as the largest organization scale of the semicrystalline polymers is concerned, banded polymer spherulites has been one of the most intriguing and extensively discussed problems in polymer physics over the last decades, starting from the early 1960s with the pioneering works of *Keith* an *Padden* [*J.Appl. Phys.*, 1964, *Polymer*, 1984] and the later findings of *Lotz* and *Cheng* [*Polymer,* 2005] and *Toda* [*Macromolecules,* 2008]. Spectacular patterns of concentric extinction rings have been observed early on in polarized optical micrographs of polymer spherulites. These regular patterns, which can reach several millimeters and even centimeters in size, were tentatively assigned to highly correlated twisted growth of lamellar crystals [Keller *Polym. Sci.,* 1959; Price *J. Pol. Sci*., 1959; Keith and Padden *J. Pol. Sci.,* 1959]. Although spherulites are not a specific morphological feature of polymers, the microstructure of banded polymer spherulites is notoriously difficult to address. One of the major experimental problems in such studies is due to the fact that, contrary to inorganic materials exhibiting curvy crystal habits [*García-Ruiz Science* 2009], the individual constitutive blocks of the semicrystalline structure such as the crystalline lamellae cannot be simply extracted from the bulk of material for study. The reason is that in a polymer sample composed of sufficiently long chains all constitutive elements are inter-connected via the so-called "tie"-chains crossing several lamellae [Geil "Polymer Single Crystals", 1963; *Wunderlich* "Macromolecular Physics" 1973]. Therefore one has to explore the details of the micro-structure and spatial arrangement of the crystalline lamellae without physically disassembling them. This task proved to be beyond the limits of classical optical microscopy, which however was and remains the most used technique for observation of polymer morphology. Thus, apart from identification of the lamella twist sense and fast crystal growth axis, determination of other

morphological parameters such as the chain tilt with respect to the basal lamella plane is not feasible with optical microscopy. A combination of optical microscopy with more recent and continuously developing techniques of scanning and transmission electron microscopy, as well as atomic force microscopy, helped circumventing the diffraction resolution limit of visible light and provided a wealth of information on the lamellar micro-structure. However, the latter techniques are severely limited with regard to the thickness of sample amenable to analysis and are therefore unable to address the bulk polymer morphology where the lamella twisting behavior is mostly observed.

In the present work, we employ a newly-developed technique of micro-focus X-ray diffraction, which combines the power of conventional structural analysis by X-rays with the enhanced spatial resolution required for studies of individual morphological features of banded spherulites. It has been recently shown that the use of modern X-ray optics to focus the X-ray beam to a spot under few microns can provide a lot of morphological detail such as the local-scale crystal orientation and regularity of crystal rotation [*Gazzano, Macromol. Chem. Phys.* 2001; *Biomacromol.* 2004]. The present thesis is an attempt to use this novel technique to unveil the mechanisms of the twisted lamella growth in polymers. In particular, we target at developing a molecular-scale model of the twisting lamellae allowing rationalizing their twisting behavior.

It is noteworthy that the model of the twisted lamella growth that will be mostly discussed in this work is due to *Keith* and *Padden*, who initially suggested that it is the unbalanced stress appearing on the lamellar surface which is mainly responsible for the lamellar twist. The pattern of the stress distribution supposedly appearing on the lamellar surface is complex, and was never addressed experimentally so far. To tackle this problem, we have chosen a semicrystalline polymer exhibiting banded spherulites, poly(trimethylene terephthalate), which has a particularity of the crystal lattice important for our analysis, i.e. its unit cell has a low symmetry. This feature is just a means to maximize the structural information to be extracted from the micro-focus X-ray experiments. We thus believe that the results obtained on this polymer are of sufficiently general character and are by no means characteristic of only this particular polymer.

The present script is organized as follows:

In the first chapter, a brief introduction into polymer crystallization is given. The extended- and folded-chain lamellar crystals are introduced being the dominate building blocks in the spherulitic polymer crystallization. The secondary nucleation theory initially

put forward by *Hoffman* and *Lauritzen* is briefly discussed together with the regimes of polymer crystallization for the chain-folded lamellar crystals. In a second part of the chapter, the banded spherulite morphology is described, and structural models accounting for the lamellar twist are critically reviewed. In the last part of the chapter, the mechanisms of the lamella branching and splaying leading to the formation of common spherulitic morphology are summarized.

In the second chapter, the materials and main experimental techniques used in the work are briefly discussed. The relevance of the applied techniques to studies of the semicrystalline polymer structure is specifically addressed. In this work, a combination of different experimental techniques has been used to characterize the structure and morphology of the semicrystalline polymer materials.

Chapters 3 through 5 are the main chapters of this work dealing with the structural analysis of the twisted lamellar crystals of polytrimethylene terephthalate crystallized at various temperatures. In chapter 3 the methodology of analyzing the data derived by the micro-focus X-ray scattering is described for the lamellar twisting apparent in films of melt-crystallized PTT to extract information on the banded spherulitic structure and morphology. Chapter 5 is the central chapter of the thesis. Here the temperature dependence of the lamellar twisting for the case of PTT is described in detail. In addition a correlation will be drawn for these specific structural features to a molecular model being able to explain the complex crystallization temperature dependence of the lamellar twisting. In chapter 6 an analytical and computer simulation approach is applied for the case of the twisted crystalline lamellae.

In the last chapter the most important results of the topic chapters are summarized and correlated to each other leading to general conclusions for the lamellar twisting in PTT.

TABLE OF CONTENTS

GLOSSARY

List of abbreviations, acronyms and symbols

Materials	
PE	Polyethylene
PEA	Poly ethylene adipade
PHB	Polyhydroxy butyrate
PBT	Polybutylene terephthalate
PET	Polyethylene terephthalate
PTT	Polytrimethylene terephthalate
PVDF	Poly vinylidene fluoride
UHMWPE	Ultra-high molecular weight polyethylene
Techniques	
WAXS	Wide-Angle X-ray Scattering
SAXS	Small-Angle X-ray Scattering
TEM	Transmission Electron Microscopy
SAED	Selected-Area Electron Diffraction
SEM	Scanning Electron Microscopy
SFM	Scanning Force Microscopy
POM	Polarized optical microscopy
DSC	Differential Scanning Calorimetry
CTFMP	Confined Thin-Film Melt-Polymerization
Other general abbreviations	
ESRF	European Synchrotron Radiation Facility
DESY	Deutsches Elektronen Synchrotron
HASYLAB	Hamburg Synchrotron Laboratory
NSLS	National Synchrotron Light Source
Other notations	
LH-theory	Lauritzen-Hoffman theory
KP-model	Keith-Padden model
I, II, III	Regimes of crystal growth
$\mathbf{B_I}$, $\mathbf{B_{II}}$, $\mathbf{B_{III}}$	Temperature intervals of spherulitic banding
$\mathbf{B_o}$	Temperature onset of lamellar twisting
$\mathbf{B_i}$	Temperature for the inversion of the lamellar twist direction
$\mathbf{B_{sp}}$	Temperature for the band spacing singularity
a, **b**, **c**	Vectors of the direct space unit cell
α, β, γ	Angles of the direct space unit cell
g, ***-g***	Lateral growth vector
G, ***-G***	Growth vector (first chirality parameter, general definition)
a, -a	Growth vector (first chirality parameter for the case of PTT)
L, *R*	Sense of the lamellar twist (second chirality parameter)
L_c	Crystal thickness of the lamellar ribbon
L_B	Long period

I. GENERAL CONSIDERATIONS

In this chapter, a brief introduction into polymer crystallization is given. The extended- and folded-chain lamellar crystals are introduced being the dominate building blocks in the spherulitic polymer crystallization. The secondary nucleation theory initially put forward by Hoffman and Lauritzen is briefly discussed together with the regimes of polymer crystallization for the chain-folded lamellar crystals. In a second part of the chapter, the banded spherulite morphology is described, and structural models accounting for the lamellar twist are critically reviewed. In the last part of the chapter, the mechanisms of the lamella branching and splaying leading to the formation of common spherulitic morphology are summarized.

I.1 Polymer Crystallization

The first evidences of polymer crystallization started to appear in the 1920's when the novel technique of X-rays initiated by the *Braggs* was first applied to synthetic and natural polymers [1]. In contrast to inorganic materials and low- molecular weight substances, the reflections generated by polymer materials revealed a rather diffuse appearance indicating on smaller and less perfect crystals. This can be understood from the fact that, in the melt, the polymer chains adopt a random coil conformation with multiple chain entanglements, which impedes ordering the chains on a regular crystal lattice upon cooling. The first structural concept of a crystalline polymer was the so-called fringed micelle model introduced by *Abitz*, *Gerngross* and *Herman* [2]. The authors supposed that the crystalline domains act as physical crosslinks of the polymer chains, as depicted in Figure I.1.1 (left). The model is able to explain several experimental observations such as the fact that the density of crystalline polymers is lower than expected from their unit cell density. Also it provided explanations as to why the crystalline polymer materials swell in solvents and why they generate diffuse *Bragg* reflections in X-ray scattering experiments.

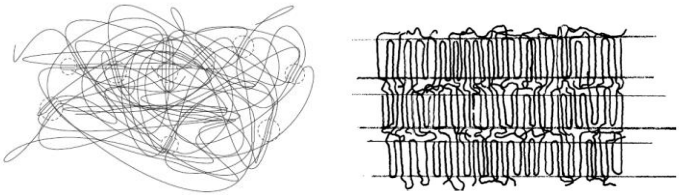

Figure I.1.1. Schematic representation of the fringed micelle model (**left**) and folded-chain crystal (**right**) reprinted from [3].

As simultaneously observed by *Till*, *Keller* and *Fischer* in 1957, when polyethylene crystallizes from dilute solutions, it forms single crystals, which have the shape of thin platelets (termed lamella) of about 10nm thick [4-6]. Afterwards, these types of experiments were reproduced on a great number of other polymers [7], and this type of crystallization was documented to be general for polymer crystallization from dilute solution. It was found that the regularity, shape and growth rate of the lamellar crystals strongly depends on the crystallization conditions such as temperature, solvent and concentration. The existence of chain folding in the polymer single crystals was demonstrated in 1957 by *Keller* [6] who employed the newly-established transmission electron microscopy (TEM) and associated selected-area electron diffraction (SAED)

allowing to simultaneously examine the sample in direct and reciprocal space with high lateral resolution. From these combined TEM/SAED studies, *Keller* concluded that the chain axis of macromolecules is close to the normal to the crystal basal plane. Since the length of the polymer chain by far exceeds the thickness of the lamellar crystal it has to fold back and forth during crystallization. Therefore, the folded-chain lamella model, as sketched in Figure I.1.1 (right), has been put forward.

Generally, polymer crystallization in the form of single crystals with well-defined habits is found to be limited to undercooled dilute solutions. When crystallized from concentrated solutions or from the melt the lamellar morphology reveals more complex hierarchical structures such as dendrites, axialites or spherulites, which are formed by radially growing lamellar stacks. The existence of the latter can be explained by the chain overlapping and entanglements creating topological problems which cannot be solved during crystallization. With accumulation of experimental observations on the melt crystallization the question on how the chains are folded in the crystalline lamella has become central to polymer crystallization. Several models of the crystal-amorphous interphase have been proposed in the 60s and 70s.

The “random re-entry” model, also termed “switchboard” model was suggested by *Flory* [8]. It consists of chains, which randomly fold back onto the same lamellar crystal or even participate in adjoining lamellae. Thus, the upper and lower surface of the lamellar crystal consists of loops (folds) of varying size as well as connecting chains entering the adjoined crystal with formation of the so-called “tie”-chains in- between the neighboring lamellae, resulting in a diffuse boundary between the crystalline and amorphous regions.

Contrasted to the above-described model, the smooth-surface model was developed by *Lauritzen* and *Hoffman* [9]. It allocated a sharp phase boundary to the lamellar crystals. In this case, the mode of re-entry into the lamella always takes place at the closest crystallographic position along the growth plane allowing only for multiple nucleation events or chain-end defects. Recognizing that this model was too ideal to describe the real melt-crystallization, a few years later *Lauritzen* [10] proposed a slightly modified version of the model in which he allowed for the fold surface to be rough. Here the chain still re-enters the lamella in the nearest crystallographic position, though large variations in the fold length may exist on a local scale. Multiple nucleation events and chain-end defects will contribute to additionally roughen the surface.

I.1.1 Theories of polymer crystallization

Various equilibrium theories were suggested to explain the chain folding in terms of a free energy minimum at a particular crystal thickness. Thus staring from the equilibrium concept, *Peterlin*, *Fischer* and *Reinhold* [11] elaborated analytical expressions for the length and period of the folding to correspond to the free energy minimum of the crystal at a given crystallization temperature. However, these theories have not been generally accepted. Therefore, another approach was independently pursued by *Lauritzen* and *Hoffman* [9] emphasizing the kinetic aspects of the crystallization process.

Thermodynamic consideration

From the general thermodynamic considerations, it is clear that a polymer chain will adopt the state of the lowest possible free energy *G*, also referred to as the Gibbs free energy. The temperature dependence of the free energy is schematically drawn in Figure I.1.2 for the liquid and crystalline state of a polymer.

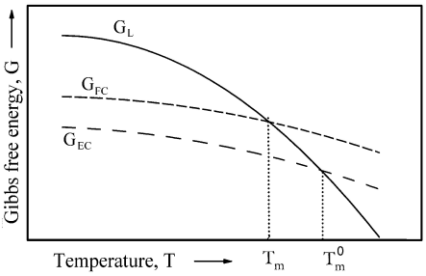

Figure I.1.2**.** Gibbs free energy *G* variation with temperature for the liquid state *L* (black), folded-chain FC (short dashes) and extended-chain EC (long dashes) polymer crystal.

From the plot it is obvious that the polymer chain should adopt the state of the extended-chain crystal when cooled below the thermodynamic melting temperature T_m^0 where the free energy of the crystal becomes smaller than that of the liquid phase. However, this general picture does not take into account the morphological pathway of the crystallizing chain, e.g. the fact that the interpenetrated random coils hinder the chains re-arrangement in the extended-chain crystal. Therefore, the chains adopt the thermodynamically unfavorable but kinetically preferred folded-chain conformation. This fact can be explained when looking on the activation energy barriers which have to be overcome during transition from the molten state to the crystal.

As schematically depicted in Figure I.1.3, the energetic barrier for extended-chain crystal (EC) is higher than the barrier towards the folded-chain crystal. In addition, the Gibbs free energy *G* of folded-chain crystals is higher than in the case of equilibrium extended-chain crystals, and they will accordingly melt at a lower temperature as shown in Figure I.1.2

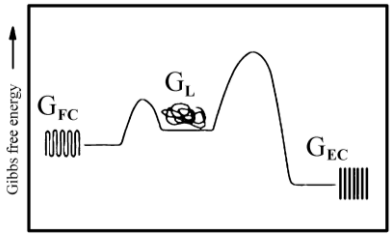

Figure I.1.3. Free energy of the folded-chain (FC) vs. extended-chain (EC) crystal.

This leads to a depression of the theoretical melting temperature. The actual melting temperature T_m of the folded-chain crystal depends on the fold length. From this it can be concluded, that the actual lamellar thickness achieved at a certain crystallization temperature is determined by the crystal growing fastest at this temperature, which is not necessarily the thermodynamically most stable one.

Regarding the liquid-solid transition itself, the necessary criterion for a spontaneous transition is the reduction of the Gibbs free energy being expressed in a negative value of ΔG, which is the thermodynamic driving force for crystallization $\Delta G = G_L - G_{EC}$ at crystallization temperature T_c written as

$$\Delta G = \Delta H - T\Delta S \qquad \text{(E. I.1.1)}$$

where ΔH is the change of the enthalpy during the transition while ΔS denotes the entropy change. At the equilibrium melting temperature T_m^0 the change of the Gibbs free energy $\Delta G = 0$ by definition. Therefore, it can be given as

$$T_m^0 = \frac{\Delta H}{\Delta S} \qquad \text{(E. I.1.2)}$$

Thus both enthalpic and entropic terms determine the equilibrium melting temperature for any polymer crystal. While a higher value of ΔH leads to a higher equilibrium melting

temperature the entropic effects cannot be ignored. Assuming that the enthalpy and entropy are slow functions of temperature, the change of the free energy ΔG at a specific temperature T is written as

$$\Delta G = \frac{\Delta H (T_m^0 - T)}{T_m^0} \qquad \text{(E. I.1.3)}$$

The driving force of the transition is the undercooling being defined as

$$\Delta T = (T_m^0 - T) \qquad \text{(E. I.1.4)}$$

I.1.2 Lauritzen-Hoffman theory

The finding that the growth rate behaves proportional to the exponent of the inverse undercooling exp(-1/Δ*T*) indicates that the crystallization is a nucleation controlled process. The two main theories accounting for the kinetics of the polymer crystallization are the "secondary nucleation theory" proposed by *Hoffman* and *Lauritzen* [9,10], in this work referred to as the *LH*-theory, and the "entropic theory" proposed by *Sadler* [12] ("rough surface theory"). Although both kinetic models are based on calculation of a free energy barrier, the nature it is considered differently. The advantage of the *LH*-theory compared to the entropic theory is that for the polymer crystallization both nucleation and growth are taken into account. In the *LH*-theory the lateral surface of a lamellar crystal is considered to be even, as illustrated in Figure I.1.4.

The first step in the secondary nucleation process is the attachment of a part of a chain, or a stem, onto the smooth crystal surface, and constitutes the activated state of the surface. Thus, the nucleus produces two new lateral surfaces of thickness *b* and height l_c leading to an overall increase of the free energy of the system by

$$\Delta\phi_1 = 2bl_c\sigma \qquad \text{(E. I.1.5)}$$

Here σ corresponds to the surface energy of the lateral surface of the lamellar crystal. In the *Lauritzen-Hoffman* model this step is associated with the highest energy barrier as visualized in Figure I.1.5 and therefore the rate determining step. The height of this barrier increases with increasing lamellar thickness l_c.

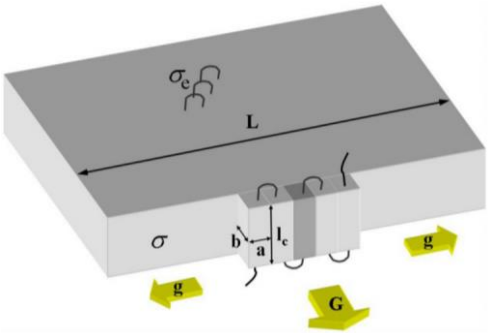

Figure I.1.4. Cartoon depicting the basics of the *Hoffman-Lauritzen* secondary nucleation theory describing successive nucleation and growth of a chain-folded lamellar crystal. *G* indicates the rate of growth accessible in the experiment, while *g* is the propagation rate of the nucleus in the lateral direction until it reaches a dislocation or impinges on another nucleus; *L* stands for the so-called persistence length of the lamellar crystal while l_c is the fold length of the lamella; *a* and *b* are the lateral dimensions of a crystalline stem; σ_e and σ are the surface energies for the fold and lateral surface, respectively.

The nucleated stem now arranges in a crystallographic register releasing a certain free energy of

$$\Delta\phi_2 = -ab/\Delta G_f \qquad \text{(E. I.1.6)}$$

where *a* corresponds to the width of the crystalline stem. The nucleation step is followed by subsequent folding back of chain to deposit another stem adjacent to the nucleated stem. This successive process lowers the overall free energy of the system by

$$\Delta\phi_2 = (\nu - 1)ab(2\sigma_e - l_c\Delta G_f) \qquad \text{(E. I.1.7)}$$

where ν is the number of stems deposited at the lateral lamellar surface while σ_e is the energy of the fold surface.

The evolution of the overall free energy of the crystallizing system is schematically given in Figure I.1.5. It is clear that the free energy reduction by packing the stem in the crystalline register always exceeds the free energy loss while producing a new surface in each step a new stem is added.

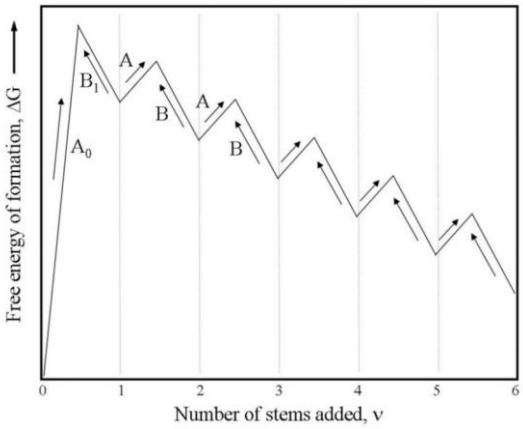

Figure I.1.5. Free energy evolution corresponding to the formation of a chain-folded surface nucleus according to the *Hoffman-Lauritzen* theory. The rate constants of attachment and detachment of the stems A_0, B_1, A and B are given in relationship to the free energy involved in the crystallization process.

Using the Arrhenius expression the rate constants for the attachment of subsequent steps can be obtained according to

$$A_0 = \beta \exp\left(-\frac{2bl\sigma}{kT}\right) \qquad \text{(E. I.1.8)}$$

and

$$A = \beta \exp\left(-\frac{2ab\sigma_e}{kT}\right) \qquad \text{(E. I.1.9)}$$

The rate constant for the detachment of the stem into the melt is given by

$$B_1 = B = \beta \exp\left(-\frac{abl(\Delta G)}{kT}\right) \qquad \text{(E. I.1.10)}$$

Here β accounts for the retardation of the reaction due to the chain segments transport from or towards the growth front and ΔG corresponds to the free energy of fusion at a given crystallization temperature. The flux of stems having the length of *1* over the nucleation barrier can be written as

$$S(l) = N_0 A_0 [(A-B)/(A-B+B_1] = N_0 A_0 (1-B/A) \qquad \text{(E. I.1.11)}$$

where N_0 corresponds to the number of reacting units being defined as

$$N_0 = C_0 \nu_L \qquad \text{(E. I.1.12)}$$

In equation (E. I.1.12), C_0 denotes the configuration path degeneracy and ν_L corresponds to the number of stems having the width *a*. The net flux can be derived according to *Hoffman* and *Lauritzen* using

$$S_T = \frac{1}{l_u} \int_{2\sigma_e/\Delta G}^{\infty} S(l) dl \qquad \text{(E. I.1.13)}$$

where l_u stands for the monomer length. The nucleation rate is defined as

$$i \equiv \frac{S_T}{L} = \frac{S_T}{n_L a} \qquad \text{(E. I.1.14)}$$

The average lamellar thickness $\langle l \rangle$ can be found by taking the statistical mechanical average using the flux as weight

$$\langle l \rangle = l_g = \frac{\frac{1}{l_u} \int_{2\sigma_e/\Delta G}^{\infty} l S(l) dl}{S_T} \qquad \text{(E. I.1.15)}$$

Equation (E. I.1.15) can be rewritten as

$$l_g = \frac{2\sigma_e}{\Delta G} + \delta \qquad \text{(E. I.1.16)}$$

with δ being defined as

$$\delta = \frac{KT}{2b\sigma} \left(\frac{\Delta G + 4\sigma/a}{\Delta G + 2\sigma/a} \right) \qquad \text{(E. I.1.17)}$$

For moderate undercoolings, δ can be approximated by

$$\delta = \frac{KT}{b\sigma} \qquad \text{(E. I.1.18)}$$

According to equations ((E. I.1.16) to ((E. I.1.18), the *LH*-model predicts that the initial lamellar thickness (i.e. the originally formed crystal before thickening) evolves linearly with the inverse undercooling $1/\Delta T$. The substrate completion rate $\boldsymbol{g}$ as visualized schematically in Figure I.1.4 can be expressed as

$$g \equiv a(A - B) \qquad \text{(E. I.1.19)}$$

According to equations ((E. I.1.8) and ((E. I.1.9) the expression for g can be rewritten

$$g = a\beta\left[\exp\left(\frac{-2ab\sigma_e}{KT}\right) - \exp\left(\frac{-abl\Delta G}{KT}\right)\right] \qquad \text{(E. I.1.20)}$$

At this point it needs to be mentioned that in the early versions of the *Lauritzen Hoffman* model the entropic character of the nucleation step was ignored, treating the attachment of the stems onto the crystalline surface and subsequent lateral completion of the row as a one-step event. In a review of the *LH*-model [10] the lateral surface free energy was correlated to the characteristic ratio C_∞ thereby considering the entropic origin of the free surface energy barrier.

During completion of the lateral rows, the only free energy barrier to overcome is the one associated with the chain folding on top and bottom surface of the crystal since there is no additional lateral surface created during this process. Here the free energy of the newly-created fold surface corresponds to σ_e. It is not correlated to the lamellar thickness indicating that the row completion process depends only weakly on the undercooling as compared to the surface nucleation event, which depends exponentially on the degree of undercooling.

The advantage of the *Lauritzen-Hoffman* theory is that it addresses the kinetics of the crystallization process for linear flexible macromolecules forming folded-chain lamellar crystals from the molecular viewpoint.

I.1.3 Crystal growth regimes

Independently of the *Lauritzen-Hoffman* theory three different regimes of crystallization can be observed as a function of the undercooling used. The schematic models elucidating the details of the regimes are given in Figure I.1.6.

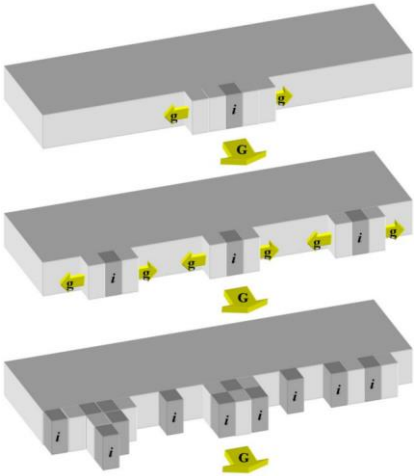

Figure I.1.6. Schematics of the secondary nucleation corresponding to growth regimes **I** through **III** (from **top** to **bottom**).

At low undercooling the growth rate is dominated by the nucleation rate of the chain stem onto the growth front. This proceeds at such slow rate that, on the average, only one nucleus is attached at the growth front while the completion of the lateral width of the lamellar crystal proceeds at much higher rate. This growth regime **I** is also referred to as mononucleation regime. Here the corresponding growth rate G_I can be expressed by

$$G_I = biL \qquad \text{(E. I.1.21)}$$

In the second regime, the rate of the secondary nucleation is faster, reaching a level when the laterally spreading nuclei start to impinge on each other. Several nuclei can be present simultaneously on the growth front. Thus, the overall growth rate G_{II} is also a function of the row completion rate g being expressed as

$$G_{II} = b\sqrt{(2ig)} \qquad \text{(E. I.1.22)}$$

It is inherent to both regimes that, due to the lateral completion of the row before adding a new layer, the folds should be mainly oriented laterally to the adjacent neighbor respectively. In contrast to growth regimes **I** and **II**, growth regime **III** takes place at large undercooling, and is dominated by fast addition of new nuclei onto incomplete layers producing a rough growth surface. Thus the growth rate is determined by the nucleation rate, similarly to regime **I**.

The growth rate G_{III} can be expressed by

$$G_{III} = biL \tag{E. I.1.23}$$

Here the orientation of the chain folds is not anymore strictly lateral but also partially oriented in the growth direction. Using the expressions for i and g, the overall growth rates can be calculated according to

$$G = G_j^0 \exp\left(-\frac{U^*}{R(T - T_m^0)}\right)\exp\left(\frac{K_{gi}}{T\Delta T}\right) \tag{E. I.1.24}$$

with K_{gi} being defined as

$$K_{gi} = \frac{jb\sigma\sigma_e T_m}{\Delta h_f k} \tag{E. I.1.25}$$

In equation (E. I.1.25), U^*corresponds to the activation energy of reptation, G_0 is a pre-factor that can be defined experimentally, T_∞ stands for the thermodynamic transition temperature where the reptation motion ceases completely. The index (i) indicates the particular growth regime, i.e. **I**, **II** or **III**. The factor f is a correction coefficient for the temperature dependence of the enthalpy of fusion given as

$$f = \frac{2T_c}{(T_m^0 + T_c)} \tag{E. I.1.26}$$

The advantage of this approach compared to a purely Arrhenius type of expression is that it takes the diffusion motion into account, which can be rather important for certain crystallization conditions such as crystallization from the glassy state.

I.2 Twisting and scrolling of polymer crystals

Formation of non-planar polymer crystals and, in particular, twisting and scrolling of polymer crystals, constitutes one of the oldest experimental observations in the field of polymer crystallization [7]. Even if the manifestation of the lamellar twisting is well known by now, the origin and nature of the phenomenon leading to the lamella twisting and scrolling are not yet clear. Thus, despite extensive studies conducted in this field, it is still a topic of ongoing interest and controversy.

Generally, lamellar twisting is easier to observe experimentally than scrolling. It is mostly manifested by the appearance of concentric rings in polymer spherulites when examined by polarized optical microscopy. Since the early days, lamellar twisting has been identified as a phenomenon occurring at the crystal growth front. It has also been recognized as a feature of individual lamella crystal or lamella stack. Several typical examples of banded spherulites are given in Figure I.2.1.

Multiple theories have been put forward to explain the origin of this spectacular morphological feature. They refer for example to non-linear diffusion processes leading to rhythmic growth, as proposed by *Kyu* et al. [13], or to self-induced compositional or mechanical fields generated near the growth front as postulated by *Schultz* [14]. Other ideas explaining the lamellar twist are based on cumulative reorientation of lamellae via successive isochiral screw dislocations, as suggested by *Toda* et al. [15-19], or on unbalanced surface stresses on opposite fold surfaces of the lamellae induced by differential congestion of the chain folds, as proposed by *Keith* and *Padden* [20]. It is noteworthy that these are just a few of the numerous explanations of the lamellar twist provided in the last decades.

In fact, twisting and scrolling of lamellar crystals are not only limited to organic polymer materials but are abundantly observed in inorganic materials such as selenium [21,22], asbestos [23] and nanocrystals of Ba or Sr embedded in amorphous silica [24]. To our knowledge, at the present time, there is no unifying theory of the lamellar twist designed. For a comprehensive review of the state of the art in this field the reader is referred to the publication by *Lotz* and *Cheng* [25]. The rest of the chapter, partly based on this review, will shortly summarize the main ideas and observations for the cases of twisting and scrolling polymer crystals.

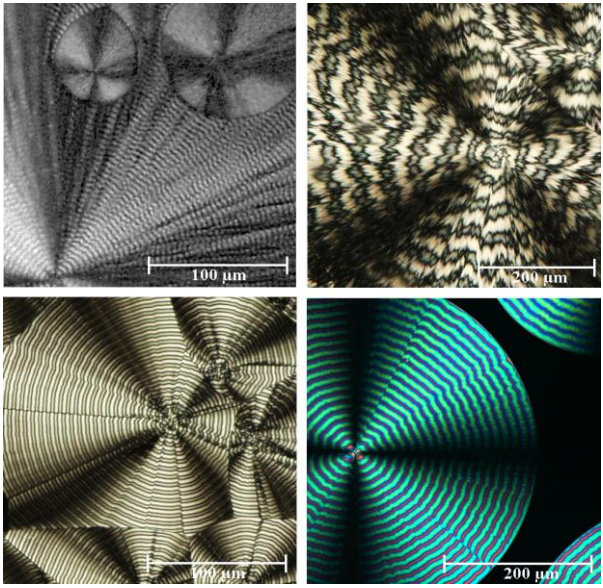

Figure I.2.1**.** Banded polymer spherulites are characterized by lamellar twist occurring cooperatively and in phase during crystal growth (**top left**). Optical micrograph of a banded spherilite of poly(vinylidene fluoride) (PVDF) α-phase crystallized at 165°C; the co-existing γ-phase exhibits non-banded spherulites. (**Top right**) Chiral poly(3-hydroxy butyrate) (PHB) crystallized at 100°C shows banded spherulites with strongly jagged bands. Regular banding in poly(ethylene adipate) (PEA) crystallized from the melt at 25°C (**bottom left**) and poly(trimethylene terephthalate) (PTT) (**bottom right**) crystallized from the melt at 170°C is observed in conventional polarized optical microscopy. The majority of polymers reveal a mono-axial indicatrix, which gives rise to single banded patterns in crossed polars. By contrast for a biaxial indicatrix such the one characterizing the unit cell of PTT, the banded textures can reveal more complex features such as double banding [26,27]. The details of the banded textures addressable by the optical microscopy are analyzed in detail by *Keith* and *Padden* [29] and *Keller* [31].

I.2.1 Experimental manifestations of the lamellar twisting in bulk materials

The banded polymer spherulites were described already in the early 1950s by *Point* [28], *Keith* and *Padden* [29,30], *Keller* [31] and *Price* [32], who showed that the concentric bands indicate an in-phase rotation of the optical indicatrix of the lamellar crystal about its radial direction (cf. Figure I.2.2).However, the optical properties of the crystal can only give an integral indication on the crystal orientation in the spherulite. Since the adequate tools were missing at the time when most of the models of the lamellar twisting appeared, the correlation of the banded texture to the inner structure of these multilamellar aggregates has remained a challenge.

An interesting approach originally developed by *Palmer* and *Cobbold* [33] using etching techniques based on fumic nitric acid was later on employed by *Keller* and *Sawada* [34] to reveal the lamellar structure of multilamellar aggregates in PE spherulites. A mild etching technique introduced by *Olley* and *Basset* [35,36] using a permanganic acid, provided a wealth of details about the lamellar shape (i.e., the description of the corrugated S- or C-shapes) and their spatial organization (i.e., dominant vs. subsidiary lamellae) within the polymer spherulites.

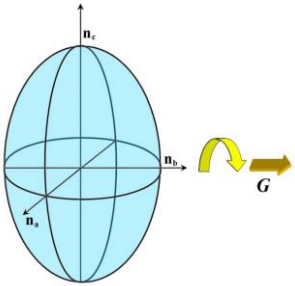

Figure I.2.2**.** Cartoon depicting the ellipsoid of the optical indicatrix built up by the refractive indices n_a, n_b *and* n_c. The yellow arrow indicates the rotation of the optical indicatrix when the lamellar crystals propagate along their spherulitic growth direction (i.e., the **b**-vector in the case of PE [29]).

It is noteworthy that the etching techniques provide morphological information only on the super-lamellar structures such as spherulites but do not give any information on the molecular level, which is the key for comprehending the nature and origin of the lamellar twist. In this respect, even the *in-situ* observations of the crystal growth such as performed by *Ivanov* [37] and *Toda* [38] show the growth process at the lamellar scale but can give only hints as to the molecular orientation within the lamellae. Therefore, the analysis of the lamellar twisting makes it necessary to use the experimental techniques such as selected area electron diffraction (SAED), which is operational exclusively on thin films or single crystals.

However, the sample geometries amenable to SAED do not necessarily correspond to the case of the bulk material. Thus, it is clear that single polymer crystals grown from solutions do not always represent the molecular structure formed in the course of the melt crystallization in the bulk. Therefore, the structural results obtained by SAED and TEM have to be evaluated carefully by taking into account the particularities of the techniques and required preparation steps of the investigated material.

The two main features inherent to the lamellar twist are the twist periodicity and twist sense. While the periodicity can be easily determined using polarized optical microscopy by measuring the distance between two successive concentric rings (i.e., the half period of a full turn of the lamella) the twist sense is much harder to tackle. To address the latter feature special tilting stages (e.g., *Fedorow* stage) for the optical microscopy were used in the past. The basics of this technique were recently reviewed by *Saracovan* and *Padden* [39]. A more technically advanced microscopy stage has been described in a recent publication [40]. Another semi-analytical approach to identify the twist sense in polymer spherulites was introduced by *Lustiger* and *Lotz* [41] using the shape of the lamellar crystal when intersected with the film surface. However, the latter method is simple only when a classical helicoidally-shaped lamella with a straight rotating section is considered.

A more straightforward technique to analyze the twist sense and the micro-structure of the twisted lamellar crystal is micro-focus X-ray diffraction employing synchrotron radiation. The use of modern X-ray optics to focus the X-ray beam on a sample to a spot under few microns can provide a wealth of structural information on the local scale such as the crystal orientation and chain tilt with respect to the lamella basal plane. In most micro-focus X-ray experiments, the super-lamellar structure is analyzed by scanning the banded spherulite along the fast crystal growth direction (i.e., the spherulite radius). This technique was used by *Gazzano* et al. to study the twisting of chiral biopolymers such as poly(3-hydroxy butyrate) [42] and poly(L-lactic acid) [43]. However a detailed analysis of the chain orientation within the lamellar crystal and its correlation to the twist sense is still missing in the literature. *Nozue* et al. [44] used this technique to identify the sense of the crystal rotation while scanning along the radial axis of a banded polycaprolactone/polyvinyl butyrate spherulites using the finite curvature of the *Ewald* sphere, the approach which will be discussed later.

I.2.2 Lamellar twisting in non-chiral polymers

The explanations accounting for the lamellar twisting in non-chiral polymers, i.e. polymers that do not contain any chiral groups in their chemical structure, can be divided in two main groups. The first one correlates the twisting with transient processes and features only existing during the crystal growth process itself, such as the rhythmic supply of crystallizable material as assumed by *Kyu* et al. [13], or the self-induced concentration or mechanical fields in the vicinity of the growth front as assumed by *Schultz* [14]. The

second group is based on morphological or structural features of the growing crystal itself, namely regular and isochiral screw dislocations as proposed by *Bassett* [16-19] and *Toda* [15], as well as surface stresses induced by differential congestion of the chain folds as proposed by *Keith* and *Padden* [45]. These theories will be considered in more detail in the following.

Lamellar twisting caused by supply of material to the growth front

Self-induced field models

These models assume transient phenomena taking place during the growth process invoking features taking place near to or at the crystal growth front having a temporary and transient nature.

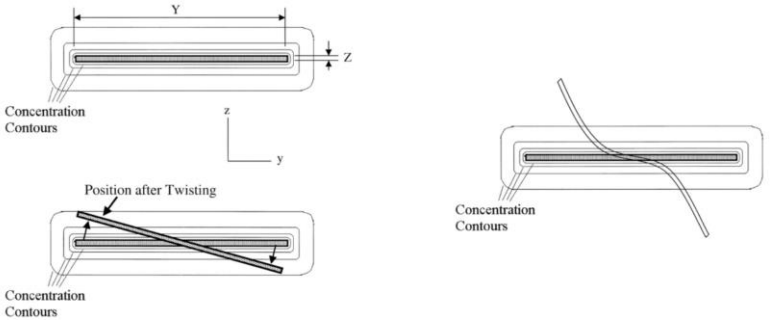

Figure I.2.3**.** Sketch of the field contours in the proximity of the lamellar growth surface (**left**). Lamellar crystal before twisting (**left top**), crystal growth surface after twisting about the growth axis (**left bottom**). Schematic drawing of an S-shaped lamella in reference to its original shape, position and field contours (**right**). Reprinted from [14].

The mechanical field concentrations as proposed by *Schultz* [46] and *Goldenfeld* [47,48] do not refer particularly to polymers. Rather, they can describe general features of any crystallization process. In summary all these theories are based on the assumption that, during the crystallization process, the crystallizable material is more depleted in the plane of the lamellar crystal ahead the growth front. Therefore, the lamellar growth front curvature is induced to reach the domains richer in "nutrients" above and below the lamellar plane. This typically results in deformation out of the initial lamella plane, giving rise to banding or twisting motion of the crystallization front forming scrolls or twisted ribbons, respectively.

Models describing the rhythmic supply of material to the growth front

As far as rhythmic growth is concerned, already *Keith* [20] suggested that it can be observed sporadically when crystallization proceeds in thin films. This suggestion was supported by the experimental findings of *Kawashima* et al. [49] who reported on "rhythmic" crystallization of poly(ethylene succinate). In this case, the observations were performed on a single crystal exhibiting a lozenge shape. The authors detected formation of successive thicker and thinner growth fronts generated by diffusion of the polymer melt towards the growing lamellar tips.

The process was found to repeatedly produce a thin depletion layer ahead of the growth front where the lamellae were constrained to grow in the flat-on orientation, which was revealed by the absence of birefringence in polarized optical microscopy. When the lamella growth proceeds further, the lamellar tip reaches again a thicker region where more "nutrient" material is available. The subsequent repetition of such fluctuation of the growth geometry leads to alternation of birefringent and non-birefringent layers described as a "fake" banding, as was documented for crystallization of poly(ε-caprolactone) [50]. However, the specificity of this case cannot be transposed on bulk crystallization, and remains a particular case of thin-film crystallization.

An explanation for the "rhythmic" growth of the lamellar crystal is based on the observation of the twisting in polyethylene reported by *Bassett* [17] and in the α-form of polyvinylidene fluoride observed *Lovinger* [51] in combination with the observations made by *Briber* and *Khoury* [52], and later, by *Okabe* et al. [53] on blends of polyvinylidene fluoride with polyvinyl acetate. In both cases the lamella are observed to grow flat for some time before it abruptly rotates halve a turn. This abrupt twist is explained by the successive accumulation of stresses in the lamellar surface being released in an "explosive" way when a certain saturation level is reached. *Briber* and *Khoury* [52] proposed that this switch-like twist can be accompanied by "fanning out" of the lamella leading to an abrupt increase of growth tips followed by an overall lateral extension of the growth front. However, clear structural evidences supporting these models are still lacking since the twist of these materials takes place on a very small scale, which is hardly addressable using conventional microscopy or scattering techniques.

Furthermore, if these models are taken as basis, twisting and scrolling should be an inherent and universal feature of lamellar growth being incapable to account for a large structural diversity existing in polymer crystallization. One feature amongst others is the

fact that many polymers reveal crystalline polymorphs which are sometimes coexisting. A typical example is poly(vinylidene fluoride) (PVDF) where the α-crystal exhibits tight lamellar twist when analyzed with optical microscopy [54] while the γ-crystal formed in the same temperature range reveals a scrolled lamellar morphology which can be revealed by scanning force microscopy [51].

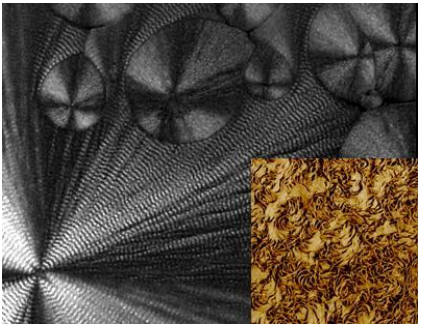

Figure I.2.4. Polarized optical micrograph of a PVDF (SOLEF 6010) film isothermally crystallized at 162.5°C. The morphology exhibits large banded spherulites assigned to the α-phase while the smaller spherulites reveal a curled lamellar morphology as shown in the insert. AFM micrograph (5x5μm²) of the PVDF γ-spherulite morphology(**Insert)**.

An interesting example of a polymer with rich polymorphism is poly(1-butene), which exhibits three different crystal modifications. As shown by *Lotz* and *Thierry* [55] the spherulites grown in form III have an orthorhombic unit cell and exhibit lamellar twisting, while the lamellae formed by the tetragonal polymorph (i.e., form II) are not twisted.

Another group of polymers exhibiting twisting are polyamides and polyesters. Here the spherulite banding morphology sometimes changes drastically with crystallization conditions passing from banded to non-banded patterns [56-58]. Magnificent patterns of banded spherulites provide members of the family of aromatic semirigid-chain polyesters including polytrimethylene terephthalate [59] and polyoctamethylene terephthalate [60], which were extensively studied in the recent years.

These cases clearly show that the crystal twisting and scrolling depends on the crystallography of the lamella. It shows that non-planar lamellar habit is not a universal feature of the lamellar crystallization. Therefore, the details of the crystal structure and its correlation to the inner spherulite morphology have to be taken into account. More specifically, one has to consider the growth axis, which is the radial direction of the spherulite, as well as the direction of scrolling for the case of scrolled crystals.

Correlating the lamellar twisting to the micro-structure

Two main theories linking the lamellar twisting and micro-structure have been developed over the last decades. Both of them were applied to the case of PE trying to link the twisted morphology with screw dislocations and surface stresses caused by extensive chain folding. These two theories will be briefly described in the following.

Lamellar twisting as a result of screw dislocations

The idea of screw dislocation being the cause of the lamellar twist was first proposed by *Basset* and *Hodge* [16] based on observations of the PE morphology. The model suggests that the twist results from successive isochiral screw dislocations leading to an isochiral splaying and twisting of the lamellar crystal. In this case, each screw dislocation contributes to the overall deviation by a quantum increment. Here the isochirality of the screw dislocation is defined by the chain tilt of the crystalline stems within the lamellar crystal with respect to its normal [17]. Based on this assumption, a correlation between the stem inclination and twisting of the lamellar crystal is deduced, which is expected to contribute to the relief of stresses in the fold surfaces [18]. *Toda* et al. [15,61] elaborated further this approach, searching to correlate the chain tilt in the lamellar crystal and the sense of the screw dislocation (i.e., left- or right-handed).

In the frame of a simple mechanical model accounting for the energy of torsion [62], the lamellar twist period P can be described as a function of the lamellar thickness l_c, the elastic modulus G and the excess of the surface tension due to the inherent stress γ_e according to

$$P = \frac{\pi}{6}\left(\frac{G}{\gamma_e \delta}\right) l_c^2 \qquad \text{(E. I.2.1)}$$

In equation (E. I.1.2), δ stands for the thickness of the surface region in which the stress is acting. Assuming that δ is not a rapid function of crystallization temperature, one can visualize the dependence of γ_e on the lamellar thickness (c.f. Figure I.2.5.).

According to *Toda* et al. [76], the mechanism of the axial screw dislocation generation could be the origin of the lamellar twisting in PE as it is expected in the case described by *Eshelby* [63] where sequential creation of screw dislocations of the same handedness evolves to a macroscopic twist.

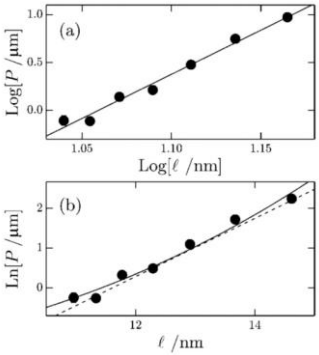

Figure I.2.5**.** Twisting period of polyethylene spherulites versus lamellar thickness: (**a**) double-logarithmic and (**b**) semi-logarithmic plots. The solid line in (**a**) represents $P \propto l_c^{2.9}$ and in (**b**) $P \propto \exp(C_{dis} l_c^3 / k_B T_c)$ reprinted from [76].

If the dislocations are created by thermal fluctuations, the ring period, P, will be determined by the probability of such fluctuation, which is exponentially dependent on the strain energy and the cube of the lamellar thickness [64]

$$P \propto \exp\left(\frac{C_{dis} l_c^3}{k_b T}\right) \qquad \text{(E. I.2.2)}$$

In equation (E. I.2.2), C_{dis} denotes to the coefficient proportional to the elastic modulus of the crystal, *K*, being a measure for the energy of the dislocation. C_{dis} can be described as

$$C_{dis} = \frac{K}{4\pi} \ln\left(\frac{R}{r_0}\right) \qquad \text{(E. I.2.3)}$$

where the constant *K* is determined by the elastic modulus of crystal a for the screw dislocation in the thickness direction; *R* and r_0 represent the size of the region undergoing the elastic deformation and that of the dislocation core, respectively.

To be considered as the origin for the lamellar twist the screw dislocations have to be located very close to the growth front to be able to affect the crystal growth of the lamella in a bulk material [20]. Even if the existence of screw dislocations at the very tip of the growth front was proved by *Toda* [15,61], they are too rare at this location, while the majority of screw dislocations are produced at the lateral edges of the crystals as shown by

Keith and *Cheng* [65]. Another argument against the theory of the screw dislocations is regarding the sense of the lamellar twist in some chiral polymers. Here only one sense of lamellar twisting was observed while the screw dislocations of both handednesses could be found. Therefore, the sense of lamellar twist is not explicitly related to the sense of the screw dislocation.

However the strongest argument against the screw dislocation theory was formulated by *Lotz* and *Cheng* [25] being the existence of twisted single lamellar crystals. Here they point to the work done by *Kunz* et al. [66] where twisted single lamellae were observed in physical gels of ultra-high molecular weight PE (UHMWPE). Indeed, if screw dislocations are involved in lamellar twisting, the twist can only be apparent in multi-lamellar stacks. From this observation the authors drew conclusion that the origin of the lamellar twist is in the lamella itself, and is manifested in the form of stresses at the fold surface.

Lamellar twist as a result of surface stresses

The idea that surface stresses can lead to lamellar twisting goes back to the early 1960s when *Geil* [67] analyzed the impact of the crystal surface on the lamellar geometry pointing to the fact that the lamellar crystal will bend when a surface strain is present. However, the origin of the surface stresses can be in principle caused by different things. *Yoffe* [68] and *Lehmann* [69] report that the unit cell parameters can be dilated close to the fold surface with respect to the lamellar core generating a negative pressure in the crystal surface, which can be reduced by a twist-like deformation of lath-like crystals. Another origin for the stresses in the lamellar surface is proposed by *Hoffman* and *Lauritzen* [70] suggesting that the spatial constraints associated with formation of folds will result in a stress acting within the fold surface.

According to *Geil* [7] an analogy can be drawn between a lamellar crystal and a tri-metallic stripe where a core is sandwiched between two surface layers having smaller expansion coefficients compared to the core. On heating, negative pressure will build up at the surfaces. The sandwich will compensate for the difference in stresses by deforming the flat sandwich into a helicoidal shape, changing the surface volume ratio in favor of the volume. However the weak point of this analogy is that the sense of the twist the sandwich will take cannot be predicted since both twists are equally favorable for such a symmetric system. Since in the polymer lamella the twist the sense is not arbitrary some other internal structural features need to be present dictating the sense of the twist.

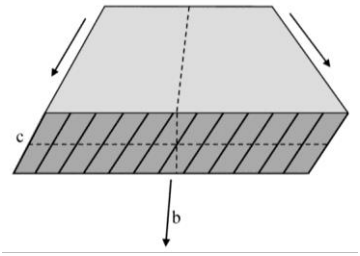

Figure I.2.6. Schematic illustration of a polyethylene lamella where the stems are inclined by a significant angle to the right. When viewed along the crystallographic **b**-axis, such lamella exhibits an inversion point.

A model suggesting the existence of unbalanced surface stresses was first introduced by *Keith* and *Padden* [45], who developed it specifically for the case of PE. However, the basic principles of the model are transferable to other polymer systems and are thus of general nature. In the case of PE the fast growth direction for a lamellar crystal forming spherulitic morphology is identified to be the crystallographic **b**-axis. According to *Lotz* [25], the crystalline stems and thus the orthorhombic unit cell are inclined by a significant angle in the **ac**-plane, perpendicular to the growth direction. When viewed along the growth direction the sectional shape of the lamellar crystal corresponds to a parallelepiped as sketched in Figure I.2.6.

Here the crystalline stems make an obtuse angle on one fold surface while it is acute on the other. This may result in different fold conformations on both surfaces. Geometrically, it is clear that there is no mirror plane within the **ac** lamellar plane, suggesting that the stresses can be unbalanced. Instead, the lamellar section in the form of a parallelepiped implies that there is point symmetry through the center of the lamellar cross section when the 2D section is considered.

When considering only the geometry of the lamella it is not clear how differential compression or dilation stresses are exerted on the lamellar surface since in the equilibrium system they should be balanced. Therefore, the kinetics of the growth process has to be taken into account. When the lamellar crystallization proceeds in growth regime **I** or **II**, as described by *Hoffman* and *Lauritzen* [9], where the linear growth rate is limited by deposition of one or several new nuclei on the growth front followed by a successive lateral completion of the added crystal row, a transient difference in the surface stresses can exist. This behavior is schematically depicted in Figure I.2.7. Here the surfaces having different stresses are indicated by the red and blue color, where the red color stays for the

lamellar surface exhibiting a positive lateral pressure with regard to the surface marked in blue. The direction of stresses is marked by the red and blue arrows on the top and bottom sides of the lamellar crystal revealing a centro-symmetric unbalanced pattern, as mentioned above. The indicated surface stresses $\boldsymbol{\sigma}(+)$ and $\boldsymbol{\sigma}(-)$ should not be considered as the absolute value of the surface stresses. Rather they only depict the relative values.

According to *Keith* and *Padden* [45], the fold conformation consumes more space when the chain overhanging the growth front, or has to fold around an acute angle, leading to a positive pressure (red region of the lamellar surface). By contrast, it is assumed to consume less space when folding around an obtuse angle (blue region). The qualitative arguments of *Keith* and *Padden* [45] and their explanations supporting this view are far from being rigorous, and were criticized in the literature [25].

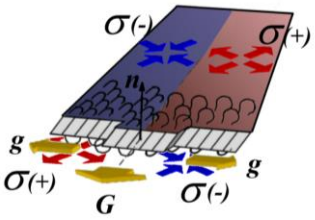

Figure I.2.7. Cartoon depicting the model of a twisted crystalline lamella according to *Keith* and *Padden* [20,45], where the twist is generated by surfaces stresses having opposite signs on both fold surfaces and both longitudinal halves of the lamella.

Since the lamellar crystal can theoretically grow along both **b**- and (-**b**)- directions, a mirror symmetry (mirror plane ***M***) can be deduced, as shown in Figure I.2.8. However, this only holds if the unit cell of high symmetry such as cubic or orthorhombic are considered. If the unit cell is of low symmetry, e.g. triclinic, as it is the case for the aromatic polyester being subject of this script, such construction is not geometrically strict anymore. However, the departure from the mirror symmetry will not change the main conclusions.

In Figure I.2.8, the mirror plane is drawn through the nucleation point of the lamella growing simultaneously in $\boldsymbol{G}^{+}$ and $\boldsymbol{G}^{-}$ directions. When the two halves of the lamella are considered independently from each other, i.e. notional; they are split. Therefore both lamellar halves would bend according to the surface stresses. Thus, the left lamella half would bend upwards, while the right one would bend downwards. In reality, both halves stay of course connected.

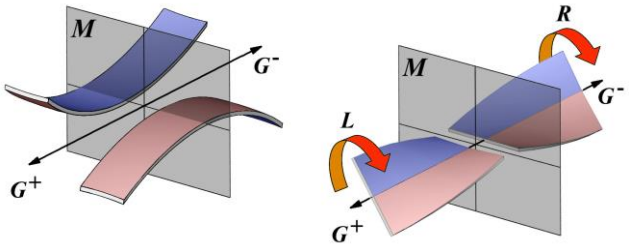

Figure I.2.8. Cartoon showing bending of two disconnected ribbons having opposite surface stresses according to the *Keith* and *Padden* model [25] (**left**). The positive surface pressure is depicted in the red overlay while the negative surface pressure is given in blue. The bending deformation keeps the mirror symmetry defined by the mirror plane ***M*** as well as point symmetry. Resulting torsional deformation of the ribbons when connected along the center line due to the unbalanced longitudinal surface stresses (**right**). The sense of deformation depends on the growth direction *G*. In the indicated stress distribution the positive growth direction G^+ is linked to a left-handed torque, while the negative growth direction G^- is linked to a right-handed torque keeping the symmetry operations discussed above.

Therefore, the opposite bending moments on the two lamella halves will impose a torque which results in a twisting of the entire lamella around the growth axis. Herby it is interesting to note that the sense of the torque and thus the handedness of the twist is different for the positive or negative growth axis polarity, being left-handed when growing in the positive direction $\boldsymbol{G}^+$ while being right-handed when growing in the negative direction $\boldsymbol{G}^-$. From this it can be concluded, that the sense of twist is directly correlated with the direction of the chain tilt adding "chirality" in the growing and twisting process.

The effect of the unbalanced surface stresses leading to a torque and thus to a twist were "recreated" by *Keith* and *Padden* [45] using partially swollen rubber bands. The rubber strips were partially sealed with a non-swelling surface layer on the opposite surface halves. Therefore, the solvent could penetrate only through the non-sealed surfaces leading to an unsymmetrical swelling of the rubber stripe and therefore producing unbalanced stresses within the stripe. To relieve the stresses, the rubber stripe starts to twist, and takes the form of a helicoid when each rubber band has exactly one half of its surface masked. If sealing of the surface is different, a more complex shape is taken by the rubber such as helices and scrolls. Importantly, the swelling produces isotropic surface stresses within the unsealed surface halves forcing the stripe to bend also in the lateral direction of the lamella. Thus, the cross-section of the rubber stripe takes the form of a weak "S", as it was observed already by *Bassett* for the PE lamellae [16-19]. Such shape exemplified in Figure I.2.9.

The mechanical analysis of the lamellar twisting proposed by *Keith* and *Padden* suggests that at the origin of the twist are the surface stresses acting within the surface plane of the lamellar crystal rather than normal to the plane as was advocated by *Bassett* [16]. However the stresses normal to the lamellar plane would only take effect in lamellar stacks (as discussed above) and could account for the successive splaying of the lamella in screw dislocations. The main assumption here is that the inclination of the stems is in a plane perpendicular to the fast growth direction. However, this only holds for the specific case of PE but as it will be shown later it is rather the direction of the molecular segment protruding the surface of the lamellar crystal than the chain tilt being defined as the direction of the c-parameter of the particular unit cell.

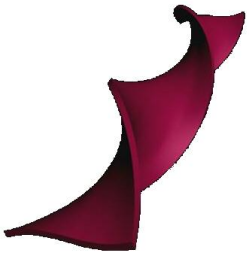

Figure I.2.9**.** Cartoon of an S-shaped helicoid with a left-handed twist. The direction of the S-shape is linked to the sense of twist by the direction of the surface stresses so that it appears that the lamellar ribbon "scoops" the melt.

The main difficulty in choosing the adequate theory is that, although both groups of theories remarkably differ in the explanation of the origin of the lamellar twist, they are hard to judge *a posteriori*, i.e. from the resulting semicrystalline morphology. Indeed, the former does not leave any traces in the structure of the lamellae except for the lamellar twist itself, which is postulated to arise from them. By contrast, the latter is supposed to be addressable in at least an indirect way, since it should leave traces in the internal lamellar structure. However, as mentioned in the above discussion, the experimental evidence is still missing since the experimental and analytical tools to study the local-scale structure are inadequate.

I.3 Branching during crystal growth and its relation to twisting

I.3.1 General remarks on crystal branching and splaying

The mechanism of splaying and branching of lamellar crystals in the course of formation of polymer spherulites is still a matter of controversy. Since the lamellae have a fast growth direction the geometry of a spherical superstructure implies that the space needs to be continuously filled by multiplying lamellar crystals. Mostly the filling of space by lamellar branches is considered to a non-crystallographic reorientation of the continuing lamellar crystal, as proposed by *Bassett* et al. [17,71,72]. Since the branching frequency will determine the lateral width of lamellar crystals at the growth front, the branching can be seen as an important factor for continuous twist when the twist angle is limited by the lateral width, as recently suggested by *Muthukumar* [73].

The origin of the lamellar branching was speculated to be the possibility of morphological instability caused by the diffusion field of non-crystallizing fractions at the growth front of polymer spherulites [74]. The basic idea of this model is that parts of the growth front overhangs the average position will feel larger driving forces for the crystallization, which will lead to an additional enhancement of this fluctuation. The characteristic length of growth front is proposed to be in proportion to the diffusion length,

$$\delta = \frac{D}{G}, \qquad \text{(E. I.3.1)}$$

being a measure for the gradient of the diffusion field with the diffusion coefficient, D, and the growth velocity, G. Thus, δ corresponds to the critical width of lamellar crystals at which they start to branch.

Experimental studys of the lamellar morphology in melt-crystallized polymers have been performed by *Bassett* and *Hodge* [17] and *Keith* and *Padden* [75] for the case of banded spherulites of polyethylene and by *Bassett* and *Olley* [71] and *Bassett* and *Vaughan* [72] for non-banded spherulites of isotactic polypropylene and isotactic polystyrene, respectively. However none of these experimental investigations could confirm the expected relationship, though *Keith* and *Padden* [75] found a consistent change in the characteristic size of a leading lamella comparing the radial dominant lamellae with the lamellar stacks oriented perpendicular to it.

For the correlation between the characteristic length formed by the morphological instability and the diffusion length, *Goldenfeld* [48] proposed the stabilizing effect of surface tension of the lamellar crystal. Here the critical length is determined by the balance of the competing effects of the gradient of the compositional field having a destabilizing effect and the surface tension. As suggested by *Goldenfeld* [48], the linear growth of polymer spherulites including the branching instability at the growth front can be controlled by a combination of the diffusion field model together with the kinetic model of the crystallization effect taking place.

Very recently, *Toda* et al. [76] proposed a mechanism for the variation of the periodicity of twisting by incorporating the spontaneous twist originated by surface stresses together with the branching instability at the growth front of individual crystals. In his model, the effect of compositional gradient is combined with the possibility of mechanical (pressure) gradient in a viscous liquid [77,78] originating from a necessary flow balancing the density difference between the crystal and the melt based on the self-induced field of pressure gradient in polymer crystallization, as pointed out by *Schultz* [79]. They report on the lamella tip splitting at the growth front of single crystals of polyethylene grown from the melt induced by the destabilization of the growth front of the polymer crystals giving a direct evidence of the branching instability of growth front. It is proposed that the lamellar crystals undergo a branching instability at a critical lateral width of the lamellar crystal followed by a reorientation according to the direction of the torsion stress induced by the unbalanced surface stresses discussed above.

I.3.2 Lamellar branching and reorientation

The multiplication of lamellae with increasing radial distance from the spherulitic center can be explained based on the branching instability at the growth front and subsequent reorientation of the branches due to the torsion stresses in the lamella generated by the unbalanced surface stresses. It was supposed [76] that the branching instability limits the lateral width L of the lamellar crystal at the growth front to maximum λ_c at which, when reached, the lamellar crystal starts to split into a pair of daughter lamellar branches, as shown in Figure I.3.1.

At this moment, the torsion stress in the lamella will create a torque on each of the daughter lamellae independently from each other reorienting the two branches at an angle $\Delta\varphi$ while keeping the handedness of twisting. The latter is obviously the same as the

handedness of the screw dislocation generated. When separated, both branches can be counted as individual lamellae twisting independently. In addition, the reorientation makes it possible that both daughter lamellae start to widen in lateral direction allowing shifting themselves onto each other. The two branches will continue to grow radially and laterally until they reach the critical lamellar width where again the next branching event will be initiated, as depicted in Figure I.3.1. By repeating this mechanism of consecutive branching and reorientation at high frequency, the 3D- space in the spherulite is filled.

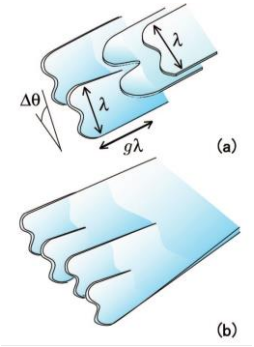

Figure I.3.1. Cartoon depicting the evolution of the crystal branching at a critical width λ (**top**) and subsequent reorientation of the daughter branches (**bottom**), reprinted from [76].

In a recent experimental evidence obtained by *Toda*, et al. [76] single crystals of polyethylene grown from the melt revealing an interesting growth front pattern, i.e. splitting at the growth face into small branches at certain distances which individually twist forming spiral terraces of the same sense. Using this it is possible to explain the close packing of helicoidal lamellar crystals forming large stacks as experimentally observed in SAXS experiments [59] not being explainable when the packing of whole infinite helicoids is considered.

I.3.3 Lamellar Branching due to a Gradient Field

The basic principle of the branching and reorientation models is the existence of a gradient in the chemical potential ahead the growth front of the lamellar crystal in the liquid polymer phase. It is supposed by *Mullins* and *Sekerka* [80] that the gradient field builds up spontaneously ahead of a stack of lamellar crystals growing parallel to each other as depicted in Figure I.3.2. Here each lamellar crystal feeling the gradient field sustained by the surrounding lamellar crystals undergoes the branching individually.

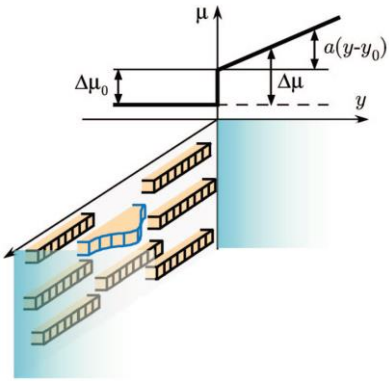

Figure I.3.2**.** Cartoon depicting the gradient field spontaneously generated ahead the growth front of a stack of lamellar crystals as proposed by *Mullins* and *Sekerka* [80]. The corresponding change of the chemical potential Δμ by the gradient is indicated, reprinted from [76].

The gradient field causing the branching is supposed to be generated by a gradient in composition and/or temperature in the liquid polymer melt ahead the growth front of the lamellar crystal as proposed by *Mullins* and *Sekerka* [80]. Although the original model supposes only diffusion processes, the model is also able to describe the growth determined by both the diffusion gradient and the crystallization kinetics. This is involved in the growth process as suggested by *Goldenfeld* [48] allowing to predict the branching instability of the interface.

In polymer crystallization, the thermal diffusion length is controlled by the thermal diffusion coefficient and the growth rate. According to this the thermal diffusion length can become larger than the spherulite itself indicating that the growth face is supposed to be stable against a weak temperature gradient. However, synthetic polymers are known to have the characteristic of multi component systems based on the polydispersity in the molecular weight and defects in the chain structure introducing a distribution in the melting temperatures and thus of the undercooling behavior of the polymer crystallization. This idea was confirmed by Bassett [81] showing that branched polyethylene reveals cellulation of the spherulite due to segregation of branches in the polyethylene chain.

REFERENCES

1 Storcks, K. H. 1938 J. Am. Chem. Soc., 60, 1753.
2 Abitz,W.; Gerngross, O.; Hermann, K. 1930 Nature, 18, 754.
3 Yves Gnanou and Michel Fontanille, Organic and Physical Chemistry of Polymers, ,p. 127, John Wiley & Sons, Inc., Hoboken, New Jersey, 2008.
4 Till, P. H. 1957 J. Polym. Sci., 24, 301.
5 Fischer, E. W. 1957 Z. Naturforsch. Teil A, 12, 753.
6 Keller, A. 1957 Philos. Mag., 2, 1171.
7 Geil, P. H., Polymer Single Crystals, Interscience, New York/London, 1963.
8 Flory, P.J. 1962 J. Amer. Chem. Soc., 84, 2857.
9 Hoffman, J.D. and Lauritzen, J.I., Jr. 1961 J. Research NBS, 65A, 297.
10 Hoffman, J.D. 1964 SPE Transactions, Oct, 315.
11 Peterlin, A.; Fischer, E.W. and Reinhold, C. J. 1962 Ghent. Phys., 37,1403.
12 Sadler, D. M.; Gilmer, G. H. 1986, Phys. Rev. Lett., 56, 2708.
13 Kyu T., 1999 Phys Rev Lett., 83, 2749.
14 Schultz J.M. 2003 Polymer, 44, 433.
15 Toda A., Arita T., Hikosaka M. 2001 Polymer, 42, 2223.
16 Bassett D.C., Hodge A.M. 1979 Proc R Soc Lond., A359, 121.
17 Bassett D.C., Hodge A.M. 1981 Proc R Soc Lond, A377, 61.
18 Bassett D.C., Hodge A.M. 1978 Polymer, 19, 469.
19 Bassett D.C. 2003 J Macromol Sci., B42, 227.
20 Keith H.D. 2001 Polymer, 42, 9987.
21 Ryschenkow G. and Faivre G., 1988 J. Cryst. Growth, 87, 221.
22 Ryschenkow G. 1991 J. Cryst. Growth, 110, 889.
23 Monkman LJ. In: Applied fiber science, vol. 3. NewYork: Acad. Press; 1979. p. 163.
24 García-Ruiz J.M., Melero-García E. and Hyde S.T., 2009 Science, 323, 362.
25 Lotz B., Cheng S.Z.D., 2005 Polymer 46, 577.
26 Chen Y.-F, Woo E.M. and Li S.-H., 2008, Langmuir, 24, 11880.
27 Woo E.M. and Chen Y.-F., 2009, Polymer, 50, 4706.
28 Point J.J. 1953 Bull Acad R Bel,41, 982.
29 Keith H.D., Padden F.J. 1959 J Polym Sci, 39, 101.
30 Keith H.D., Padden F.J. 1959 J Polym Sci, 39,123.
31 Keller A. 1959 J Polym Sci, 39, 151.
32 Price F.P. 1959 J Polym Sci, 39, 139.
33 Palmer R.P., Cobbold A.J. 1964 Makromol Chem.,74, 174.
34 Keller A., Sawada S. 1964 Makromol Chem., 74, 190.
35 Olley R.H., Hodge A.M., Bassett D.C. 1979 J Polym Sci, Polym Phys Ed, 17, 627.
36 Bassett D.C., Olley R.H. 1984 Polymer, 25, 935.
37 Ivanov D.A., et al., 2008 Macromolecules, 41, 9224.
38 Toda A., et al., 2010 Macromolecules, 43, 3837.
39 Saracovan J, et al., 1999 Macromolecules, 32, 8918.
40 Iwata T., et al., 2009 Macromolecules 42, 694.
41 Lustiger A., Lotz B., Duff T.S. 1989 J. Polym. Sci., B: Pol. Phys., 27, 561.
42 Gazzano M., et al., 2001 Macromol. Chem. Phys. 202, 1405.

REFERENCES

43 Gazzano M., et al., 2004 Biomacromol., 5, 553.
44 Nozue Y., et al., 2004 Polymer, 45, 8299.
45 Keith H.D., Padden F.J., 1984 Polymer, 25, 28.
46 Schultz J.M. "Polymer crystallization" Oxford, UK: Oxford University Press; 2001.
47 Ben-Jacob E., et al., 1986 Phys Rev Lett, 57, 1903.
48 Goldenfeld N.J., 1987 J. Cryst. Growth, 84, 601.
49 Kawashima K, et al., 2003; J. Macromol. Sci. B42, 889.
50 Alfonso G.C. et al., 2008 Macromolecules 41, 7584.
51 Lovinger A.J. 1980 J Pol. Sc., Pol. Phys. Ed.,18, 793.
52 Briber R.M., Khoury F. 1993 J Pol. Sc., Pol. Phys. Ed, 31, 1253.
53 Okabe Y., Kyu T., Saito H., Inoue T. 1998 Macromolecules, 31, 5823.
54 Vaughan A.S. 1993 J Mater Sci., 28, 1805.
55 Lotz B., Thierry A. 2003 Macromolecules, 36, 286.
56 Khoury F. 1958. J Pol. Sci., 33, 389.
57 Magill J.H. 1966 J Pol. Sci. A2, 4, 243.
58 Wang B.J., et al., 2001 Polymer, 42, 7171.
59 Ivanov D.A., et al., 2008 Macromolecules, 41, 9224.
60 Chen Y-F., et al., 2008 Langmuir, 24, 11880.
61 Toda A., Keller A. 1993 Colloid Pol. Sci., 271, 328.
62 Okano K., 1953 Jpn. J.Appl. Phys., 24,176.
63 Eshelby, J.D. 1964, J. Appl. Phys., 3, 351.
64 Schultz, J.M. and Kinloch D.R., 1969 Polymer, 10, 271.
65 Keith H.D., Chen W.Y. 2002 Polymer, 43, 6263.
66 Kunz M., Dreschler M., Möller S. 1995 Polymer, 36, 1331.
67 Geil P.H. Polymer single crystals. New York: Wiley; 1963. Chapter 4, p. 225.
68 Yoffe V.S. 1944 Uspekhi Chimii, 13, 144.
69 Lehmann O. Molekularphysik, Bd. 1, Leipzig, Wilhelm Engelmann,1888.
70 Hoffman J.D, Lauritzen Jr. J.I. 1961 J Res Natl Bur Stand (US), 65A, 297.
71 Basset D.C., Olley R.H., 1984 Polymer, 25, 935.
72 Basset D.C., Vaughan A.S., 1985 Polymer, 26, 717.
73 Muthukumar M., presented at the 234th ACS National Meeting.
74 Keith H.D.Jr., 1963 J. Apl. Phys., 34, 2409.
75 Keith H.D.Jr., 1987 J. Pol. Sci. Part B: Pol. Phys, 25, 2371.
76 Toda A., et al., 2008 Macromolecules, 41, 2484.
77 Saffman P.G., Taylor G.I., 1958 Proc. R. Soc. London, Ser.A., 245, 312.
78 Fields R.J., Ashby M.F., 1976 Philos. Mag., 33, 33.
79 Schultz J.M., Polymer Crystallization; Oxford University Press: Oxford,2001.
80 Mullins W.W., Sekerka R.F. 1963 J. Appl. Phys., 84, 601.
81 Basset D.C. et al., 1998 Macromolecules, 31, 7800.

II. METHODOLOGY

In this chapter, the materials and main experimental techniques used in the work are briefly introduced. The relevance of the applied techniques to study the semicrystalline polymer structure is specifically addressed.

In this work, a combination of different experimental techniques has been used to characterize the structure and morphology of the semicrystalline polymer materials. These include direct-space techniques such as Polarized Optical Microscopy (POM) and Atomic Force Microscopy (AFM), as well as reciprocal-space techniques such as Wide- and Small- Angle X-ray scattering in conventional as well as in micro-focus setup.

II.1 Poly(trimethylene terephthalate) PTT

II.1.1 Characteristics of PTT

Poly(trimethylene terephthalate) (PTT) is a typical semirigid-chain aromatic polyester characterized by excellent mechanical properties. It contains an "odd"-number alkyl spacer, and is usually synthesized by polycondensation from 1,3-propanediol (PDO) with dimethyl terephthalate or terephthalic acid. PTT is one of the three high-melting polyesters introduced by *Winfield* and *Dickson* in 1941 [1]. The PTT structure completes the row between the "even"-numbered poly(ethylene terephthalate) (PET) and poly(butylene terephthalate) (PBT). The chemical structure of PTT is given in Figure II.1.1. The commercial grade (Corterra LP 509200, Shell) used in this study has a number average molecular weight M_n of about 17300 g/mol and a weight average molecular weight M_w of 35200 g/mol. Therefore it has a polydispersity index of about $M_w/M_n = 2$. It is noteworthy that it is only in 1998 that PTT became commercially available due to development of a new production technology of PDO *via* hydro formulation of ethylene oxide [2].

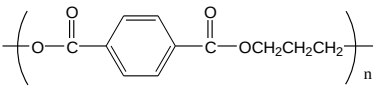

Figure II.1.1. Chemical structure of poly(trimethylene terephthalate)

II.1.2 Thermal behavior of PTT

Upon crystallization of PTT its glass transition temperature, T_g, is shifted to higher temperatures. This feature is typical of the semirigid-chain semicrystalline polymers. The temperature shift of T_g can be as high as 60°C, depending on crystallization conditions [3,4]. Moreover, from the variation of specific heat capacity in the glass transition region, a rigid amorphous fraction was inferred in the semicrystalline structure of PTT. This fraction was however found to be smaller than those in PET and PBT [5].

Moreover, PTT is characterized by complex melting behavior. The thermodynamics of the PTT crystals and their structure were extensively studied in the recent years using calorimetric [2-11] and microscopic [12-16] techniques. PTT exhibits several thermal events clearly visible in the DSC traces, which are exemplified in Figure II.1.2. The

mechanism of this complex melting behavior is still subject of an ongoing debate in the literature. However, several models have been put forward to explain the multiple melting behavior of PTT and similar semirigid-chain polymers [17-19]. One of the interpretations is based on a structural model including crystals of different degree of perfection, which brings about an earlier melting of less perfect crystals and their subsequent re-crystallization to form more perfect and thermodynamically stable crystals. An alternative explanation suggests that each melting event can be assigned to a different population of crystalline entities, i.e. parts, or whole of, the crystalline lamellae.

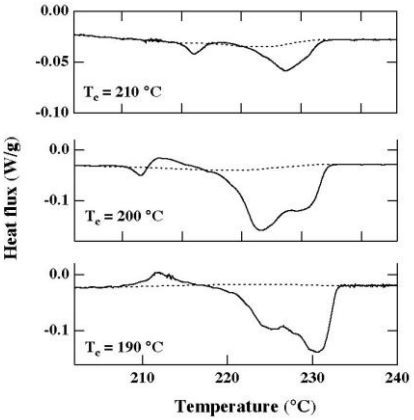

Figure II.1.2 DSC traces of poly(trimethylene terephthalate) as a function of isothermal crystallization temperature T_c. The curves reveal a complex pattern of melting/recrystallization events. Heating rate is 1°C/min. [20].

However, to our knowledge none of these models has been shown to possess the required generality [21,22]. In addition, there are evidences that the thermodynamics of polymer crystals is not only determined by the crystal thickness, as in the classical Gibbs-Thomson picture, but may also depend on some other parameters such as the interlamellar amorphous layer thickness [23].

II.1.3 Banding in PTT spherulites

Interestingly, in the literature the multiple melting behaviour of PTT is sometimes associated with the banded spherulite structure [12,13], which is exemplified in Figure II.1.3. The circular bands in the spherulites indicate that the lamellar twist during growth is cooperative and in phase. Significant efforts have been directed since more than half a

century to understanding of the relationship between the semicrystalline morphology and the crystal growth mechanisms, but many unsolved problems persist [10]. Although it has been well documented that the banding period resulting from synchronous lamellar twist during crystal growth [24-27] crucially depends on the crystallization temperature, the details of the formation mechanisms of the twisted lamellae remain an topic of ongoing debate in the literature [24-27].

When one examines the banded textures of PTT in crossed polars, they first strike by their colorful appearance. Importantly, the color patterns are observed without addition of any light retardation elements. Such behavior is in fact not typical for polymers forming banded spherulites and is explained by the high birefringence of PTT, which has been previously discussed by *Yun* et al. [28,29] and *Chen* et al. [30].

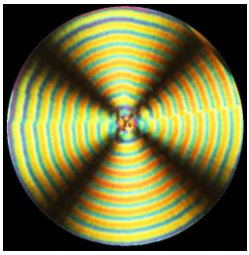

Figure II.1.3 Banded spherulite of melt-crystallized PTT, as viewed between crossed polars.

As far as correlations of the banded spherulite textures with crystallization temperature are concerned, there were already attempts to describe the dependence of the band spacing with the power-law function. Thus, *Chuang*, et al. [31] found that the critical exponent equals 0.5, which can be compared to the well-known critical exponent of the order parameter in the mean-field theory of equilibrium phase transitions [32,33]. However, not everything is set in the description of the banding behavior of PTT itself. Indeed, *Chuang*, et al. observed that the banded-nonbanded transition (BNB) for PTT occurs at 195°C on the low-temperature side and at ca. 215°C on the high-temperature side [34]. The results of *Chuang and Hong* [31, 34] are however strongly different from other reports on PTT. Thus, *Wu* and *Woo* [35] reported the BNB transitions of PTT to occur at 150 and 215°C. By contrast, in the work of *Wang*, et al. [36], the temperature window of the banded morphology is reduced to within 135 and 165°C. Therefore for unknown reasons the existing literature data on the PTT banding is far from being consistent.

II.1.4 Crystal structure of PTT

The crystal structure of PTT has been extensively discussed in the literature. In general, the authors converge on assignment of the PTT crystalline lattice to triclinic symmetry with P-1 space group, whereby the unit cell hosts two monomers (see Figure II.1.4). However, the exact parameters slightly vary in different reports, depending on the nature of the sample, its processing history and the used analysis technique [36-38].

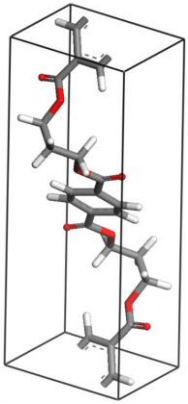

Figure II.1.4. Molecular structure of the poly(trimethylene terephthalate) unit cell.

The unit cell parameters measured by wide-angle X-ray scattering (WAXS) and selected-area electron diffraction (SAED) on fibers, thin films and bulk samples are summarized in Table II.1.1. [40-44]. It is noteworthy that the unit cell of PTT is large along the **c**-parameter (2 nm), especially when it is compared to the typical thickness of the PTT lamella (ca. 5nm) [19]. According to *Cheng*, et al. [39], the best estimates of the PTT unit cell parameters were given by *Hall* [43]. The latter will be used for the calculation of the crystallographic reflections in this work.

Table II.1.1. Unit cell parameters of poly(trimethylene terephthalate)

	a, Å	b, Å	c, Å	α, deg	β, deg	γ, deg	ρ, g/cm³
Poulin-Dandurand [40]	4.637	6.266	18.640	98.4	93.0	111.1	1.387
Desborough [41]	4.620	6.200	18.300	98.0	90.0	112.0	1.427
Tadokoro [42]	4.580	6.220	18.120	96.9	89.4	111.0	1.430
Hall [43]	4.600	6.220	18.360	97.8	90.8	111.3	1.414
Ho [44]	4.630	6.120	18.600	97.5	92.1	110.0	1.400

Most of the literature data on the PTT crystallography was obtained using wide- angle X-ray diffraction on fibers [40-43]. Obviously this approach does not allow identifying the crystalline stem inclination within the folded-chain crystals. Selected-area electron diffraction (SAED) data collected by *Poulin-Dandurand* [40] and co-authors on PTT single crystals formed from dilute solution showed that the dominating growth axis corresponded to the **a**-vector [40], similarly to what was found for the PTT melt crystallization [44].

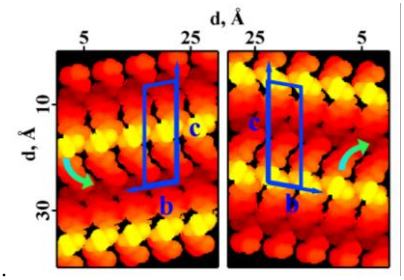

Figure II.1.5**.** Calculated topography of the PTT crystal **bc**-plane reveals two different chiral conformations when viewed along the positive and negative crystallographic **a**-axis. (**left**) view on the negative **bc**-plane, (**right**) view on the positive **bc**-plane,

It is noteworthy that the polymer chain conformation in the crystal shows no overall chirality. However, when analyzed with more scrutiny, the conformation reveals helical structures of alternating chirality, i.e. one monomer adopts a right-handed helical conformation while the other one is left-handed. The alternating helical sense of the chain is visible when looking along the fast crystal growth direction, i.e. the **a**-axis. The topography of the molecular chain calculated from the fractional coordinates listed in Table II.1.2 is shown in Figure II.1.5.

Poulin-Dandurand and co-authors [40] also report on a perpendicular orientation of the PTT crystalline stems with respect to the lamellar basal plane. The latter finding is in contradiction with report of *Ho* et al. [44] who addressed the melt-crystallized PTT films with transmission electron microscopy (TEM) combined with SAED. In this work, the authors identified the PTT lamellar basal plane as the **ab**-plane.

Therefore, the chain tilt with regard to the normal to the lamellar basal plane corresponds in this case to crystallographic angle **α** minus 90 deg, giving the resulting inclination angle of about 8 deg. In contrast to this result, *Wang* et al. [36] found by SAED that, for the case of confined thin-film melt-polymerized (CTFMP) PTT, the chain tilt was

as large as 24 deg, and the crystalline stems were tilted in the direction of the crystallographic **a**-vector. It is appropriate to emphasize that the unit cell of the CTFMP PTT was also triclinic, with lattice parameters that are rather close to the one reported by Hall [43]. However, besides almost identical unit cell parameters, these findings can be hardly compared to those obtained on melt- or solution-crystallized PTT due to its particular polymerization method.

Table II.1.2. Fractional atomic coordinates of the PTT unit cell [40]

Atom	x	y	z
O(12)	-0.4287	0.0404	0.1525
O(12')	-0.4862	-0.1459	0.3316
O(11)	-0.1057	0.4076	0.1508
O(11')	-0.3742	-0.4629	0.3414
C(16)	-0.1322	-0.2392	-0.0246
C(11)	-0.0978	0.0998	0.0606
C(17)	-0.2077	0.2016	0.1257
C(18)	-0.553	0.1208	0.3163
C(38)	-0.7961	-0.0918	0.2357
C(18')	-0.6711	-0.262	0.262
C(17')	-0.352	-0.2661	0.365
C(11')	-0.1688	-0.1306	0.4356
C(16')	-0.0111	-0.2233	0.4788
C(12)	-0.23	-0.1394	0.036
C(12')	-0.1578	0.0947	0.4579
H(121)	-0.396	-0.2401	0.0619
H(161)	0.2277	0.4119	0.0424
H(181)	-0.3835	0.1573	0.2577
H(182)	-0.6495	0.2336	0.2048
H(381)	-0.9194	-0.0434	0.2728
H(381')	-0.9595	-0.1734	0.1933
H(182')	-0.8469	-0.4062	0.2684
H(181')	-0.5381	-0.3036	0.2262
H(161')	-0.0191	-0.3879	0.4626
H(121')	-0.2716	0.163	0.4268

II.2 Methods

II.2.1 Direct-space techniques

Polarized Optical microscopy (POM)

Optical microscopy is a relatively simple and useful tool for investigations of the semicrystalline polymer morphology. The most common geometry of optical microscopy applied to semicrystalline polymers is in transmission. In this case, the light from the condenser lens is transmitted through the specimen. Further on, it passes through the objective lens system, which provides magnification of the image. The limitations in transmission-light microscopy are not that much related to magnification as they are to resolution, illumination and contrast. The resolution, d, of conventional optical microscopy depends on the wavelength of light, λ, and aperture, A, of the objectives as follows

$$d = \frac{\lambda}{A} \qquad \text{(E. II.2.1)}$$

In equation (E. II.2.1), d is the minimal distance between separately reproduced image points (cf. the Rayleigh resolution criterion). Thus the highest possible resolution in visible-light microscopy is about 0.5 μm. However, a drastic improvement of illumination and contrast can be achieved by modification of light microscopy such as phase contrast or differential interference contrast microscopy.

The predominant contrast mechanism in conventional transmission light microscopy is based on the selective light absorption within the object. A limitation for all optical light microscopic techniques is the decreasing depth of focus with increasing magnification. In polarized optical microscopy (POM) the birefringence of the material is used to discriminate the different morphological features. Birefringence, also referred to as double refraction, is an inherent property of materials to rotate the polarization plane of linearly-polarized light when it passes through it. The birefringence is given as

$$\Delta n = n_e - n_o \qquad \text{(E. II.2.2)}$$

where n_e and n_o are refractive indices corresponding to the two perpendicular directions. This specific optical behavior is originated from the fact that the electric field vector $\boldsymbol{E}$ and

the dielectric displacement ***D*** are not parallel in anisotropic media resulting in an anisotropic propagation of light along two different directions of the indicatrix (e.g., the crystallographic axes of the crystalline materials). In materials where the birefringence is high, as it is the case of PTT, the phase shift between the two pathways of light can be in the order of $\lambda/4$. Thus, the linearly polarized light will be circularly polarized while passing through the sample, resulting in additional interference effects [45,46].

In this work, POM observations have been carried out using an Olympus BX51 microscope equipped with Olympus DP70 digital color camera. The camera employs a single-chip charge-coupled device (CCD) sensor with Bayer RGB primary color filtration. The two-thirds-inch CCD chip incorporates 1.45 million effective pixels, which can be piezo-shifted during image acquisition to obtain a maximum effective resolution of 12.5 mega pixels. The camera-user interface allows the time and interval variables to be entered, and a series of images to be captured. To study the crystallization kinetics of the semicrystalline polymers the microscope was equipped with a Mettler heating stage [47].

Scanning Force Microscopy (SFM)

Scanning force microscopy (SFM) belongs to the group of scanning probe microscopy techniques (SPM) and is dedicated to analysis of surfaces, similarly to SEM. The general principle of all SPM techniques is rastering of a very fine probe across the sample surface while measuring the probe-material interaction.

In the case of scanning force microscopy often referred to as atomic force microscopy (AFM), a tiny sharp tip mounted on a miniature cantilever is the probe which is scanned using high resolution manipulators. The force between the sample surface and the tip strongly depends on the separating distance, and is measured by deflection of the cantilever. In the common SFM techniques, the interacting force is kept constant by adjusting the distance between probe and surface using a PID control. The control signal for adjusting the distance is monitored and provides information about the surface topography. The basic principle of SFM is illustrated in Figure II.2.1.

The maximum vertical displacement is limited to a few microns while the lateral scanning dimensions are limited to 100 µm in conventional instruments. Due to the highly sensitive adjustment, the resolution in the vertical direction is in the sub-nanometer range. The lateral resolution strongly depends on the sample surface morphology and on the radius of the tip. For very flat specimens with periodic lattice, e.g. mica, the true atomic

resolution is in principle achievable [48]. Therefore dynamic modes such as Tapping Mode AFM (TMAFM) are used for determination of the phase morphology. The basic principle of all dynamical SFM methods consists in modulation of the interaction between the sample surface and probe. In TMAFM, also referred to as intermittent contact mode, the modulation is a harmonic oscillation of the probe driven at a frequency near to the fundamental resonant frequency of the cantilever.

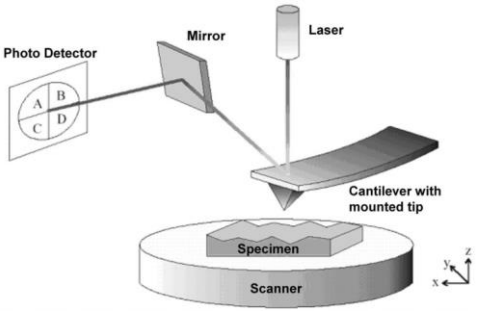

Figure II.2.1. Schematic drawing of principal components of AFM reprinted from [49].

In TMAFM, the cantilever enters in contact with the surface during each oscillation period. The characteristic parameters of the oscillation such as amplitude, phase shift and resonant frequency are functions of the interaction with the sample surface, reflecting the local mechanical properties of the polymer material such as stiffness, viscoelasticity, adhesion, and others.

In the present work, AFM imaging was performed using a commercial Multimode microscope equipped with a Nanoscope IV controller (Digital Instruments/Veeco Metrology Group). AFM Images have been taken with a J-type piezo-scanner (max. scan size is 120x120 μm^2). The microscope was operated in Taping Mode using conventional non-contact-mode cantilevers from Nanosensors having a resonant frequency of about 170 kHz.

Scanning Electron Microscopy (SEM)

Scanning electron microscopy (SEM) is a very powerful tool for examination of surface morphology of polymers. To get information on the bulk structure, the sample preparation includes sectioning, cryo-fracture, grinding, etc. A disadvantage of this

technique is the necessity to have a conductive surface, which requires metal sputtering for the case of non-conductive polymers.

In SEM, the surface area of interest is scanned by a fine electron probe focused on the sample surface. The electrons are generated by means of an electron gun with a tungsten or Lanthanum Hexaboride (LaB_6) filament or by field emission and subsequent electron lenses for demagnification of the electron cross-over. The elastic and inelastic interactions of the primary electrons of the electron beam with the atoms in the close-up range of the sample surface lead to emission of secondary electrons, back-scattered electrons and characteristic X-rays that are collected by special detectors and converted into a corresponding images while scanning the probe in a rectangular pattern across the sample surface. The brightness of each pixel within the image corresponds to the intensity of the detected signal at the corresponding point at the sample surface.

The interaction volume of the electron beam with the sample is determined by the energy of the primary electrons and the atomic number of the involved material. The higher the accelerating voltage and thus the energy of the electron beam and the smaller the average atomic number, the larger is the interaction volume. The resolution of SEM is determined by the spot size of the electron beam and the size of the leaving area on the sample surface of the different interaction products. In general all three interaction products described above are used for imaging. Nevertheless, for microscopy on polymers mainly the image information provided by the signal of the secondary electrons is used [50,51].

II.2.2 Reciprocal-space techniques

During the last decades, applications of X-ray scattering have significantly broadened due to the development achieved in both, powerful detectors as well as X-ray optics allowing to focus the beam down to the sub-micron scale while keeping a small divergenceof. Soft matter structural analysis using synchrotron radiation sources has enforced its role as a fundamental tool in materials science. In this work, the X-ray diffraction experiments were performed using exclusively synchrotron radiation sources at the European Synchrotron Radiation Facility (ESRF, Grenoble), the Deutsches Elektronen- Synchrotron (DESY, Hamburg) as well as at the National Synchrotron Light Source (NSLS, Brookhaven National Laboratory, Upton, USA) [52].

Wide- and Small-Angle X-ray Scattering using synchrotron radiation

A typical layout of a synchrotron is sketched in Figure II.2.2. In contrast to conventional in-house X-ray machines where the X-rays are produced by decelerating electrons in the anode material such as copper, the synchrotron radiation is generated by deflecting the trajectory of fast electrons in a static magnetic field.

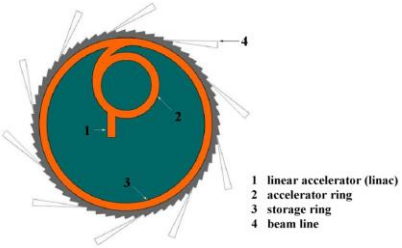

Figure II.2.2. Cartoon schematically depicting the main features of a synchrotron [52].

Therefore the electrons emitted by an electron gun are first accelerated in a linear accelerator (linac) and feed in an accelerator ring reaching for reaching their final energy. The latter is approximately 6GeV for the ESRF and 4.5GeV for DESY. When the final energy is reached the electron packages are injected in the large storage ring circulating in a high vacuum environment. The storage ring is composed of curved and linear sections (cf. Figure II.2.3). Electrons are driven with magnetic fields generated by bending magnets, focusing magnets and undulators. The cross- sectional shape of the electron beam is kept using focusing magnets acting like magnetic lenses. In the curved sections the electron beam is deflected from a straight path by strong static bending magnets forcing the electrons on the trajectory of a circular arc while emitting synchrotron radiation tangentially.

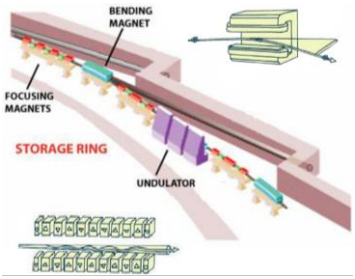

Figure II.2.3. Outline of the storage ring at the ESRF and its components [52].

When the electron beam passes undulators located in the straight sections of the ring the electrons are forced to oscillate due to the alternating poled static magnets emitting highly intense synchrotron radiation. In contrast to the bending magnets the magnets in the undulators can be varied changing the characteristic of the synchrotron radiation spectra. The synchrotron radiation leaving the storage ring at specific locations is guided to the tangentially aligned beamlines. Each beamline consists of three main modules comprising the optics, experimental and control sections as shown in Figure II.2.4.

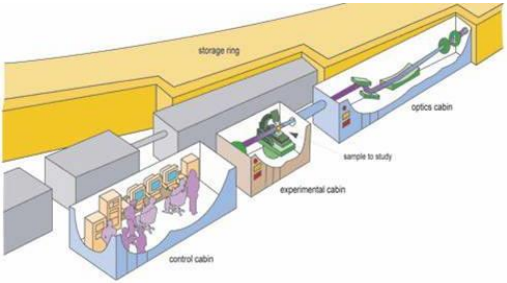

Figure II.2.4. Schematic drawing of a layout of a conventional beamline at the ESRF [52].

In the optics section the synchrotron beam is shaped to fit the experimental conditions in energy, flux and size when it is possible. The typical setup of an optics hutch is depicted in Figure II.2.5 Therefore the beam is sent through a double-crystal monochromator for adjusting the desired monochromatic energy followed by a focusing mirror adjusting the sagittal and meridional focus of the beam. The slits operation allows cutting the parasitic reflections and excess of flux.

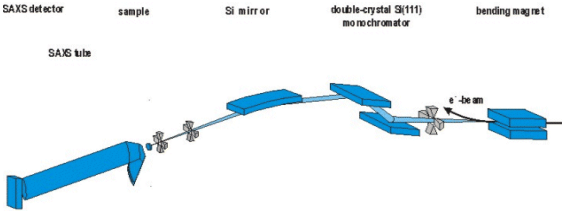

Figure II.2.5. Cartoon depicting the optics of the BM 26B beamline at the ESRF [52].

The “shaped” beam is the guided to the experimental section, where the sample environment and data collecting systems are located. Since the ionizing radiation used is highly harmful to the health, the controlling of the experimentation is located in an extra-control cabin separated by a lead wall from the experimental section.

BM26B beamline at the ESRF

The ESRF Dutch Belgium beamline (DUBBLE) is mainly dedicated to small- and wide-angle X-ray Scattering (SAXS/WAXS). It is operated at a variable energy ranging from 5 to 30 keV. The source of X-ray is generated by a bending magnet. Although the line can be operated at different wavelengths, 10 keV X-rays were typically used in our work corresponding to the wavelength λ of 1.24Å. Since different setups were used, they will be discussed in more detail in the experimental part of the corresponding chapters.

The beamline is equipped with a Frelon CCD camera mainly used for 2D WAXS experiments. The gas wire detector used in SAXS experiments is characterized by an active area of 133mm x133mm and spatial resolution of about 250μm. The detector irregularities were corrected by measuring the sensitivity pattern using a Fe^{55} source. For performing variable-temperature experiments the sample fixtures were equipped with a Linkam heating stage coupled to a temperature controller and a liquid nitrogen pump.

A2 beamline, HASYLAB/DESY

The experimental setup is shown in Figure II.2.6. The beamline is operated at a fixed wavelength of λ=1.5 Å. The beam is focused on the SAXS detector by a series of successive segmented mirrors placed after the Si (111) monochromator. An ionization chamber is installed upstream the sample to monitor the intensity of the primary beam.

Figure II.2.6**.** Setup of the A2 beamline at HASYLAB/DESY (**left**) showing the vacuum-compatible chamber containing the sample stage with the vacuum heating stage (**right**).

The data are recorded using a MARR CCD camera at a distance of 1.2m downstream the sample. The sample temperature is controlled using a specially designed heating stage compatible with the vacuum chamber to avoid parasitic air scattering.

ID13 beamline at the ESRF

The ID13 microfocus beamline at the ESRF provides an extremely small focal spots of the X-ray beam allowing spatially resolved X-ray scattering experiments. The beamline uses an 18 mm period in-vacuum undulator optimized for 13 keV. The incident photon energy can be varied between approx. 5 keV (cut-off of beryllium windows) and 17 keV (mirror cut-off). Higher energies are accessible without focusing.

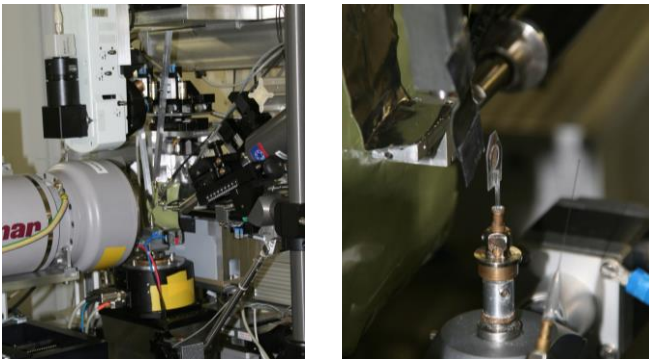

Figure II.2.7. Experimental setup (**left**) and the sample stage (**right**) at the ID 13 beam line.

The monochromatic X-ray beam is focused first by the use of beryllium lenses. The crossed-Fresnel optics in combination with an extremely long focusing distance up to 50m allows to achieve a high flux combined with a small divergence of the beam and to focus the monochromatic X-ray beam down to the sub-micron range along both axes. For experiments requiring scanning of a sample, an x-y piezo gantry can be installed. Since the lateral move of the specimen requires high precision, the moved sample complex needs to be extremely light and small to prevent overshooting during the stepwise motion

The navigation on the sample is controlled by an on-axis optical microscope installed downstream the sample (cf. Figure II.2.7). Beam monitors in form of ionization chambers installed upstream the sample provided dose-monitoring for online exposure normalization. A Frelon fast CCD, with a pixel size of 50 microns (not rebinned) and a 16-bit readout can be installed downstream the sample at variable distances allowing to select the desired scattering range for the experiment.

X13B beamline at the NSLS

The X33 micro-focus beamline is used to perform X-ray scattering experiments on soft and hard materials. The energy ranges from 6.5 to 19 keV. An X-ray beam is generated using a bending magnet. The views of the beamline and setup are given in Figure II.2.8

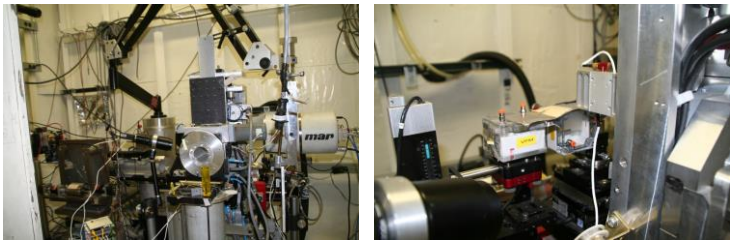

Figure II.2.8. Setup of the X13B experimental hutch (**left**) and the KB-crystals focusing the X-ray beam (**right**).

The optical system is composed of a monochromator of Si (111) channel-cut located at a distance of 10 m from the source. The focusing mirror is a rhodium-plated bent cylindrical Si single crystal for 1:1 focusing on the sample and located at 11.3 m from the source. The beam is focused on the sample by a set of two KB crystals of 100 mm located upstream the sample allowing the spatial resolution of 10µm at the sample. The detector used in the experiment was a MARR CCD camera. The sample was scanned by means of an x-y-gantry using motors with a precision of 1 micron.

II.2.3 Data reduction and analysis

The results of the scattering experiments do not directly address the structural details as it is the case for direct-space methods like microscopy, but need a more involved data processing. In this section, the procedures and methods of data reduction and processing are briefly introduced and described.

Preliminary data reduction for a 2D scattering pattern

The first step in the reduction of 2D X-ray pattern comprises a mathematical treatment dealing with the various possible detector inhomogeneities such as differences in the local sensitivity. Therefore, a sensitivity pattern is collected using a homogenous radiating

source such as Fe^{55}. A typical sensitivity pattern showing the wire grid characteristic of wire gas detectors is given in Figure II.2.9.

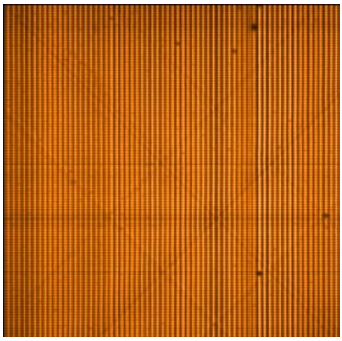

Figure II.2.9. Typical detector sensitivity pattern showing various inhomogenities and a grid structure characteristic of wire gas detectors used in the SAXS experiments.

The data matrix I_{raw} is normalized by the sensitivity matrix I_{sens} according to

$$I_M = \frac{I_{raw}}{I_{sens}} \qquad \text{(E. II.2.3)}$$

In equation (E. II.2.3) I_M stands for the sensitivity-corrected intensity of each pixel. It a real experiment, a background signal is added to the recorded scattering signal, which is inherent to the electronic nature of the specific detector. This particular background does not depend on the experimental conditions but only on the detector itself. Therefore, for each particular acquisition time, it is required to record a dark-count image which will be subtracted from the collected raw data matrix before any further data treatment, similar to the sensitivity correction, applies.

Another correction required for measurements performed on synchrotron beam lines is the normalization of each image to the intensity of the primary X-ray beam. Since the current of electrons in the storage ring is decaying with time, the intensity of the primary beam decays as well. Therefore, ion-chambers are placed upstream the sample allowing dose monitoring during the data acquisition. To account for the signal added to the scattering of the sample itself by the use of sample windows or other transmitted media, the corresponding “empty cell” measurements are collected accounting for the sample setup. After normalization for the sample transmission, the “empty cell” intensities can be subtracted from the sensitivity-corrected raw data matrix according to equation (E. II.2.4)

$$I_{cor} = E_{2M}\left(\frac{I_M}{E_{1M}} - \frac{I_B}{E_{1B}}\right) \qquad \text{(E. II.2.4)}$$

where I_{cor} stands for the corrected pixel intensity in the data matrix, I_M and I_B correspond to the collected pixel intensities for the measurement of the sample and background (i.e. "empty cell"), respectively, and E corresponds to the beam intensity measured upstream E_1 and downstream E_2 the sample for the particular measurement.

The integration of 2D X-ray patterns are performed using home-made procedures designed in the Igor Pro® environment with built-in mathematical libraries. The designed procedures include data handling capabilities allowing to process individual patterns as well as arrays of 2D data in a batch mode. They also allow to perform pattern centering, calibration and integration as a function of the norm of the scattering vector or azimuthal angle.

As a part of the data reduction, the 2D data matrix needs to be corrected for possible image distortions for example due to inclination of the detector normal with respect to the incident beam, which results in elliptical deformation of the diffraction rings on the detector plane. In this case, since the ellipses are not concentric, it makes it the data not straightforward. Another reason for distortion of the pattern can be some lateral inhomogenities of the sensitive elements of the detector, which generate anisotropic deformation of the image. While the elliptical deformation due to the inclination of the detector can be addressed analytically, the distortion due to the inhomogenities cannot. If there is no distortion map provided for the specific detector, it can be derived using an isotropic standard as used for example for the d-spacing calibration. In this case the distances of the diffraction peaks are mapped as a function of the azimuthal angle of the pattern. The distortion map is calculated by using the deviation of the mapped distances as a function of the azimuthal angle. Figure II.2.10 shows the effect of the applied distortion correction on a silver behenate pattern measured using the Photonioca CCD at the BM26 beam line of the ESRF.

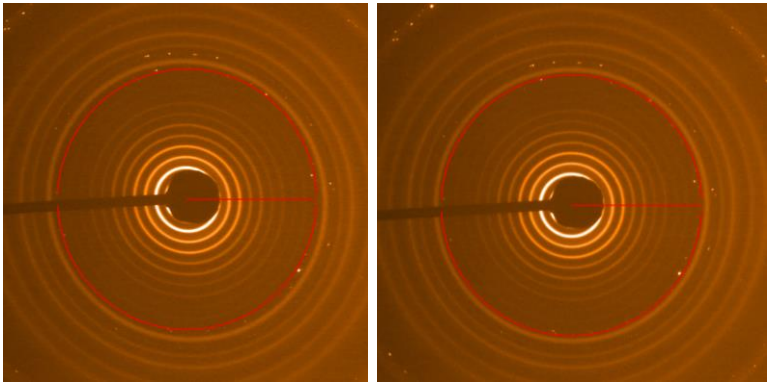

Figure II.2.10. 2D diffraction patterns of silver behenate: raw pattern (**left**) and the same pattern after correction for the image distortions (**right**). The black circle highlights the deformation of the diffraction ring in the uncorrected pattern as compared to the corrected one.

The calibration of the d-spacings on the pattern is performed using several orders of reflection of a known standard sample such as benzoic acid or corundum for wide-angle measurements and silver behenate or collagen for small-angle measurements. In both cases the Bragg formula reads

$$s = \frac{2}{\lambda}\sin(\theta) \qquad \text{(E. II.2.5)}$$

where s is the modulus of the scattering vector. The diffraction angle θ for the specific reflection is derived from simple geometrical considerations

$$\theta = \frac{1}{2}\arctan\left(\frac{r}{d}\right) \qquad \text{(E. II.2.6)}$$

where *r* corresponds to the distance from a particular reflection to the center of the pattern and *d* stands for the sample-to-detector distance. After radial integration of the 2D pattern, the intensity of the scattering curve is plotted versus the modulus of the scattering vector s. The first piece of information to be extracted is the position of intensity peak maxima as a function of *s*.

Further data reduction for SAXS data analysis

For a lamellar system comprising alternating layers of different electron density the average nearest neighbor distance of the similar layers is denoted as long period L_B. For small angles $\sin\theta \cong \theta$, the L_B can be roughly obtained from the first order peak maxima by $L_B = 1/s$. The spatial resolution of the SAXS method is limited to about >0.5 nm in direct space [53].

SAXS data analysis based on the two-phase approach

Since small-angle X-ray scattering operates in the reciprocal space, it does not directly provide the structure in the direct space. Therefore, the interpretation of the measured signal is dependent on the structural model used in the analysis. The one- dimensional two-phase model employed in this work is conventional for the case of lamellar semicrystalline polymers.

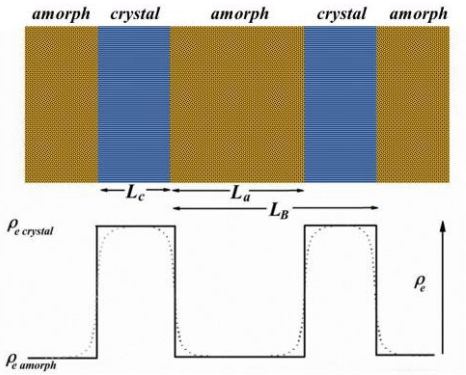

Figure II.2.11**. Top**: Schematic model of an ideal two-phase lamellar system comprising crystalline lamella separated by amorphous layers. **Bottom**: schematics showing the electron density profile for the case of a sharp boundary (solid line) and a sigmoidal-gradient transition layer [54-56].

The electron densities of the two phases ρ_e have distinct values while the boundary between is considered to have a relatively small thickness indicating strong phase segregation, as depicted schematically in Figure II.2.11. In the sketch, the dense lamellar crystals are separated by less dense amorphous layers (cf. the electron density profile depicted in the solid line).

One-dimensional auto-correlation function $\gamma_1(r)$

The one-dimensional auto-correlation function $\gamma_1(r)$ of the electron density profile is defined as [57]

$$\gamma_1(r) = \frac{\int_0^\infty I_c(s)s^2 \cos(2\pi sr)ds}{\int_0^\infty I_c(s)s^2 ds} \qquad \text{(E. II.2.7)}$$

where I_c denotes the corrected scattering intensity. Thus it can be stated that the 1D correlation function is simply the real part of the Fourier transform of the *Lorentz* corrected intensity $I_c(s)$. For the case of isotropic sample the *Lorentz* correction compensates for the fact that the scattering intensity is distributed over the whole surface of the *Polanyi* sphere having the radius s [58]. Since the area of the *Polanyi* sphere increases as s^2, the experimentally measured scattering intensity needs to be multiplied with the same factor.

In the experimental data treatment, several other corrections have also to be considered before performing the Fourier operation. Thus, because of the finite measurement range the experimental data may require be extrapolation to both the zero scattering angle s = 0 and also to the large values of s. The extrapolation to zero can be performed for example by using the *Debye–Bueche* approach [59] given as

$$I(s) = \frac{C}{(1+4\pi^2\xi^2 s^2)^2} \qquad \text{(E. II.2.8)}$$

In equation (E. II.2.8), ξ denotes the inhomogeneity length and C is a constant. The C and ξ can be derived from the plot of the square root of the scattering intensity as a function of s^2 in the low s-region. However, this correction affects only the very low frequencies corresponding to large spacings in the correlation function and therefore has not been considered in the analysis. The extrapolation to the infinite values of s is done using the *Porod* law. As assumed by *Porod* [60] the scattering from an ideal two-phase system decays as one over the fourth order of the modulus of the scattering vector s.

$$\lim_{s\to\infty} I(s) = \frac{K_P}{s^4} \qquad \text{(E. II.2.9)}$$

The constant K_p is denoted as the *Porod* constant, which is related to the specific area of the interface separating the two phases within the irradiated volume. Mathematically it can be expressed by

$$K_p = \frac{(\Delta\rho)^2 S}{8\pi^3} \qquad \text{(E. II.2.10)}$$

with S being the specific inner surface and Δρ the electron density contrast.

In the described approach the interface between the regions having different electron densities is put to be infinitely small. In the real situation it can happen that the electron density variation is spread over a certain distance. Therefore, the approach accounting for the electron density gradient (cf. solid and dotted lines in the bottom panel of Figure II.2.11) was derived by *Porod* and *Ruland* [61]

$$\lim_{s\to\infty} I(s) = \frac{K_P}{s^4}\exp(-4\pi^2 s^2\sigma^2) \qquad \text{(E. II.2.11)}$$

The exponential term in equation (E. II.2.11) corrects for the contribution from the interphase, the width of which is given by σ. For semicrystalline polymers it is related to half width of the transition layer between crystalline and amorphous regions. *Ruland* [62] placed the low-angle limit for the validity of *Porod* law between the first and third order of the main interference peak of a quenched LDPE sample, which is around 0.012 Å [5].

Evaluation of the auto-correlation function $\gamma_1(r)$ As discussed above, the original contribution of *Vonk* and *Kortleve* [63] addressed the one dimensional auto-correlation function approach, which was dedicated to the analysis of ideal two-phase systems such as given in Figure II.2.12 (top). The corresponding auto-correlation function is given below in the dotted line. It exhibits a series of triangles starting at $r = 0$ and then repeated in a sequence at distances proportional to L_B. These features reflect the correlations of the lamellae to the next and further neighbors within one lamella stack.

The structural parameters such as L_1, L_2 and L_B can be derived directly from the correlation function. L_1 and L_2 correspond to the intersection of the linear regression in the auto-correlation triangle (LRAT) with the base line of the $\gamma_1(r)$.

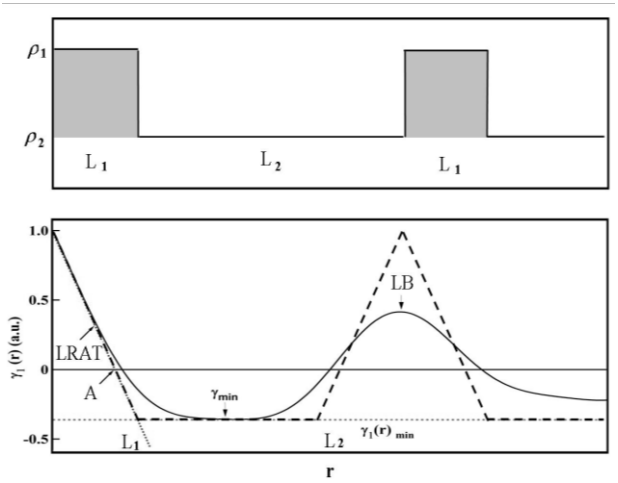

Figure II.2.12. Model 1D-correlation function for an ideal two-phase system and the corresponding structural parameters derived.

The long period L_B can be derived from the position of the first maxima in the $\gamma_1(r)$ function while the local volume fraction Φ_L can be extracted from the minimum γ_{min} of the correlation function according to

$$\gamma_{min} = \frac{-\Phi_L}{1-\Phi_L} \quad \text{for } \Phi_L < 0.5; \text{ and} \qquad \text{(E. II.2.12a)}$$

$$\gamma_{min} = \frac{1-\Phi_L}{-\Phi_L} \quad \text{for } \Phi_L > 0.5 \qquad \text{(E. II.2.12b)}$$

In real experiments such perfect shapes are rarely observed due to the fact that the thicknesses of the layers are distributed varying around a certain mean. The correlation function corresponding to the case where the local layer thickness varies within a certain distribution is exemplified in Figure II.2.12 bottom (solid line). An alternative approach to calculate Φ_L is the result of the quadratic expression given by

$$A = \Phi_L(1-\Phi_L)L_B \qquad \text{(E. II.2.13)}$$

where A corresponds to the intersection of the LRAT with the abscissa. The two possible solutions of this equation correspond to the two situations for Φ_L connected as $(1-\Phi_L)$ and

Φ_L. The intersection of the LRAT with the ordinate gives the total scattering power Q being an invariant which can be expressed according to *Vonk* [64] by

$$Q = \int_0^\infty I(s)s^2 ds \qquad \text{(E. II.2.14)}$$

If the model having a finite interphase is considered, the scattering intensity needs to be corrected for the interlayer term where I_{cor} is expressed by

$$I_{cor}(s) = I(s)e^{(4\pi^2\sigma^2 s^2)} \qquad \text{(E. II.2.15)}$$

The Interface Distribution Function approach

The interface distribution function (IDF) contains the information about the distribution of the interfaces in the material structure. The analysis of SAXS curves using the IDF was developed by *Ruland* [62]. The IDF can be numerically calculated by two different methods based on the same analytical form. However, when applied to discrete experimental data, some differences can be observed.

Calculation of the Interface Distribution Function $g_1(r)$

The interface distribution function denoted in this manuscript as $g_1(r)$, can be calculated as the second derivative of the correlation function $\gamma_1(r)$ introduced above.

$$g_1(r) = \frac{\delta^2(\gamma_1(r))}{\delta r^2} = \gamma_1''(r)\ . \qquad \text{(E. II.2.16)}$$

One has to exercise caution when analyzing the experimental data having a discrete nature. Thus the numerical double differentiation can make problematic the end points of the data points array. This effect can lead for example to strong discrepancies at the lower limit of the r-range, which is the most interesting region containing the information about the lamella and inter-lamellar thickness.

Another approach to obtain the $g_1(r)$ function is to calculate the Fourier transform of the interference function $G_1(s)$

$$g_1(r) = \int_0^\infty G_1(s)\cos(sr)ds \qquad \text{(E. II.2.17)}$$

where $G_1(s)$ is defined as

$$G_1(s) = K - I_c(s)s^4 \exp(4\pi^2\sigma^2 s^2) \qquad \text{(E. II.2.18)}$$

In equation (E. II.2.18), $I_c(s)$ is the background-corrected scattering intensity. The advantage of the latter approach is the fact that the Fourier transform is applied to the already pre-processed data and no differentiation is used.

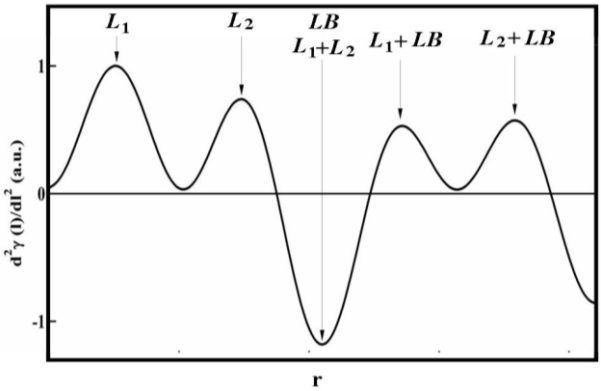

Figure II.2.13. Interface distribution function for a 1D-structure.

The interface distribution function $g_1(r)$ represents the probability distribution of finding two interfaces such as the one between a crystal and the adjacent amorphous region in the case of semi crystalline materials separated by a distance r.

$$g_1(r) = A_p \sum_{i=1}^{m} w_i h_i(r - r_i) \qquad \text{(E. II.2.19)}$$

where w_i stand for the weights of the distribution function h_i centered at r_i.

The values of $g_1(r)$ are negative if the sequence of the phases is the same at both considered interfaces, as it is for example in the case of the distance representing the long period (cf. Figure II.2.13). If the sequences are opposite as it is the case of the lamellar or

amorphous thickness the distributions become positive. As shown by *Stribeck* and *Ruland* [65] the structural parameters can be either estimated from the IDF directly or extracted by performing a more sophisticated analysis.

Evaluation of the Interface Distribution Function

According to *Ruland* [65], the IDF function of a two-phase lamella system can be considered as a series of distance distribution functions h_i, as given by Eq**.** (E. II.2.19)**.** If normalized Gaussian distributions are considered, h_i can be written as

$$h_i = \frac{1}{\sigma_i \sqrt{2\pi}} \exp\left(-\frac{(r - r_0)^2}{2\sigma_i^2} \right) \qquad \text{(E. II.2.20)}$$

The positions of the center value r_i of the distribution functions are correlated starting from i = 3 since they are higher harmonics of the first distribution functions. The correlations can be expressed as

$$r_i = n(r_1 + r_2) \quad \text{for } i=3n \qquad \text{(E. II.2.21a)}$$

$$r_i = n(r_1 + r_2) + r_1 \quad \text{for } i=3n+1 \qquad \text{(E. II.2.21b)}$$

$$r_i = n(r_1 + r_2) + r_2 \quad \text{for } i=3n+2 \qquad \text{(E. II.2.21c)}$$

The weight functions for a finite stack can be described by [65]

$$w_i = \exp(-r_i/t) \quad \text{for } i \neq 3n \qquad \text{(E. II.2.22a)}$$

$$w_i = -2\exp(-r_i/t) \quad \text{for } i=3n \qquad \text{(E. II.2.22b)}$$

where t is the average height of the stack. The finite stack size results in an exponential decay of the harmonics intensity. However, not only the area under the higher harmonics will change but also the standard deviation σ_i will change according for example to the paracrystalline model [66].

Generally, there are two main models used to describe the paracrystalline stack structure. The first one assumes independent thickness distributions of r_1 and r_2 of phases 1 and 2, respectively. This can be imagined by stacking alternating layers in a successive

manner while the thickness of each layer follows its corresponding distribution function. For this case the relationships for the σ_i values read as follows

$$\sigma_i^2 = n(\sigma_1^2 + \sigma_2^2) \qquad \text{for} \quad i=3n \tag{E. II.2.23a}$$

$$\sigma_i^2 = n(\sigma_1^2 + \sigma_2^2) + \sigma_1^2 \quad \text{for} \quad i=3n+1 \tag{E. II.2.23b}$$

$$\sigma_i^2 = n(\sigma_1^2 + \sigma_2^2) + \sigma_2^2 \quad \text{for} \quad i=3n+1 \tag{E. II.2.23c}$$

The other possibility is to assume that the layer thicknesses within a given stack oscillate around a certain mean value, i.e. the variances of r_1 and r_L are independent. In this case σ_L corresponds to the convoluted distribution of peak 1 and 2 at position $r_L = r_1 + r_2$. Therefore the general expression for the distribution width reads as follows

$$\sigma_i^2 = n(\sigma_1^2 / 2 + \sigma_L^2) \quad \text{for } i=3n\pm1 \text{ and } i=3n \text{ for } (n>1) \tag{E. II.2.24}$$

Remarks on the calculation and interpretation of the CF and IDF

The extrapolation of the scattering intensity to large s-values using *Porod* law is often necessary since the resolution of the Fourier-transformed data is proportional to the inverse of the number of points in the data set. However, the resulting direct-space information should not be over-interpreted. Special caution has to be exercised when considering the values of the function corresponding to low r-values because it may happen that the experimental curve contains little or virtually no information in this range. Furthermore, the fit of the *Porod* law to the experimental curve requires careful adjustments of the fit parameters because a minor kink or step in the curve will result in of spurious harmonics in the CF and especially in the IDF, as the latter is more sensitive.

REFERENCES

1 British Patent 578,079 (1964).

2 Chuah H. H., 2001 Pol. Eng. Sci., 41, 308.

3 Cheng S.Z.D. and Wunderlich B. 1968 Macromolecules, 19, 1868.

4 Cheng S.Z.D., 1988 Macromol. Chem., 189, 1579.

5 Pyda M., 1998 J. Pol. Sci. B:Pol. Phys., 36, 2499.

6 Hong P.-D., 2002 J. Appl. Pol. Sci., 83, 2426.

7 Hong P.-D., 2002 Polymer, 43, 3335.

8 Woo E. M., 2002 J. Pol. Sc. B: Pol. Phys., 40, 1571.

9 Suppaphol P., 2003 Euro. Pol. J., 40, 599.

10 Suppaphol P., 2004 Therm. Chim. Act., 409, 63.

11 Chen X., 2007 Pol. Test., 26, 144.

12 Woo E.M., 2003 J. Pol. Sc. B: Pol. Phys., 41, 80.

13 Hong P.D., 2004 Polymer, 45, 2413.

14 Kuboyama K., 2006 Polymer, 47, 1715.

15 Kuboyama K., 2006 Polymer, 47, 4831.

16 Woo E. M., 2007 Matt. Let., 61, 4911.

17 Srimoaon, P., Dangseeyun, N. and Supaphol, P. 2004 Eur. Pol. J., 40, 599.

18 Wu, P.-L.; Woo, E.M. 2003 J. Pol. Sci. Part B: Pol. Phys., 41, 80.

19 Ivanov D.A., et al., 2008 Macromolecules, 41, 9224.

20 Amalou Z., "Contribution à l'étude de la structure semi-cristalline des polymères à chaînes semi-rigides", Dissertation, ULB Bruxelles Belgium, 2006.

21 Supaphol, P. 2004 Eur. Pol. J., 40, 599.

22 Wu, P.-L. and Woo, E.M. 2003 J. Pol. Sci. Part B: Pol. Phys., 41, 80.

23 Ivanov, D.A. 2004 Eur. Phys. J. E, 13, 363.

24 Keith, H.D. and Padden, F.J., 1959 J. Pol. Sci., 39, 123.

25 Lotz, B. and Cheng, S.Z.D. 2005 Polymer, 46, 577.

26 Keith, H.D. 2001 Polymer, 42, 9987.

27 Shultz, J.M. 2003 Polymer, 44, 433.

28 Yun J.H., et al., 2006, Polymer, 47, 4831.

29 Yun J.H., Kuboyama K. and Ougizawa T., 2006, Polymer, 47, 1715.

30 Chen Y-F., Woo E.M., Wu P-L., 2007, Mat. Lett., 61, 4911.

31 Chuang W.-T., Hong P.-D. and Chuah H.H., 2004 Polymer, 45, 2413.

32 Sornette D. "Critical phenomena in natural science" New York: Sprinter: 2000.

33 Auyang S.Y., "Foundations of complex system theories" New York: Cambridge University Press: 1998.

34 Hong P.-D., Chuang W.-T. and Hsu C.-F., 2002, Polymer, 43, 3335.

35 Wu P.-L. and Woo E.M., 2002 J. Pol. Sci. Part B: Pol. Phys., 40, 1571.

36 Wang B., et al., 2001, Polymer, 42, 7171.

37 Ho R.M. et al., 2000 Macromolecules, 33, 7529.

REFERENCES

38 Geil P.H., 2001 Polymer, 42, 7181.

39 Cheng S.Z.D., et al., 2000 Polymer, 42, 7181.

40 Poulin-Dandurand S., 1979 Polymer, 20, 419.

41 Desborough I.J.,1979 Polymer, 20, 545.

42 Tadokoro H., "Structure of crystalline polymers" Wiley-Interscience, New York:1979, p. 369.

43 Hall I.H., Structure of crystalline polymers London: Elsevier Appl.Sci. 1984, p.39.

44 Ho R.M., 2001 Polymer, 42, 7171.

45 Keith H.D., Padden F.J.Jr. 1959 J.Pol. Sci., 39, 101.

46 Keith H.D., Padden F.J.Jr. 1959 J.Pol. Sci., 39, 123.

47 Olympus and Mettler Toledo general and technical information (www.olympus.com/, www.mt.com).

48 Klinov, D. and Magonov, S., 2004 Appl. Phys. Lett., 84, 2697.

49 Delineau L., "Dynamic der Spitze-Probe Wechselwirkung bei der Rasterkraftmikroskopie an Elastomeren", Dissertation, Albert Ludwigs Universität Freiburg im Breisgau 2001.

50 Flegler S.L. "Elektronenmikroskopie – Grundlagen, Methoden, Anwendungen", Spectrum Akademischer Verlag GmbH Heidelberg, Berlin, Oxford: 1995.

51 Schmidt P.F., "Praxis der Rasterelektronenmikroskopie und Mikrobereichsanalyse", Expert-Verlag, Berlin: 1994.

52 ESRF and NSLS general and technical information (www.esrf.eu/, www.nsls.bnl.gov/).

53 Stribeck X-ray scattering of soft matter. Springer, Berlin: 2007.

54 Koberstein J.T., Stein R.S., 1983 J. Pol. Sci. Pol. Phys. Ed.. ,21, 1439.

55 Koberstein J.T., Stein R.S., 1983 J. Pol. Sci. Pol. Phys. Ed.., 21, 2181.

56 Koberstein J.T., Stein R.S., 1984 Pol. Eng. Sci. 24, 293.

57 Vonk C.G. and Kortleve G., 1967 Kolloid Z Polym. 220, 19.

58 Polanyi, M. 1921 Z. Phys. 7, 149.

59 Debye P. and Bueche A.M., 1949 J. Appl. Phys. 20, 518.

60 Strobl G., The Physics of Polymers, Springer Berlin Heidelberg New York: 1997.

61 Ruland W., 1971 J. Appl. Cryst. 4, 70.

62 Ruland W., 1977 Colloid Pol. Sci., 255, 417.

63 Vonk C. G. and Kortleve G., 1967 Kolloid Z Polym, 220, 19.

64 Vonk C. G.; 1973 J Appl. Cryst., 6, 81.

65 Ruland W., 1978 J. Appl. Cryst., 11, 535.

66 Hosemann R., Bagchi S.N. Direct Analysis of Diffraction by Matter, North Holland: Amsterdam (1962).

III. BANDED SPHERULITES OF POLY(TRIMETHYLENE TEREPHTHALATE): MICRO-FOCUS X-RAY DIFFRACTION DATA ANALYSIS

Martin Rosenthal[1], Denis V. Anokhin[1], Richard Davies[2], Manfred Burghammer[2], and Dimitri A. Ivanov[1]

1) Institut de Sciences des Matériaux de Mulhouse, CNRS LRC7228, 15 rue Jean Starcky, 68057 Mulhouse, France

2) European Synchrotron Radiation Facility (ESRF), 6 rue Jules Horowitz, 38043 Grenoble, France

Abstract

Micro-beam X-ray diffraction has been used to address the texture of banded spherulites of melt-crystallized poly(trimethylene terephthalate), PTT, formed in films of approximately 20 to 40 µm thickness. The WAXS micro-diffraction patterns show that, on a local scale, the PTT texture is close to that of a single crystal. In agreement with previous studies by Selected-Area Electron Diffraction conducted on thin PTT films, it is shown that the fast crystal growth direction is parallel to the ***a****-axis of the unit cell. When plotted as a function of the distance to the spherulite center, the intensity of different diffraction peaks reveals the same periodicity. This means that the lamellar twist is strictly uniform and regular. The latter observation is more compatible with the model explaining the twist as a result of unbalanced surface stresses (KP-model) [1] than that of isochiral giant screw dislocations [2]. In agreement to the first postulate of the KP-model, a correlation of the twisting sense of the lamella with the growth axis polarity is observed. However, a very faint chain tilt in the plane perpendicular to the growth direction calls into question the second postulate of the KP-model identifying this parameter as the main cause of the unbalanced surface stresses leading to the twisted crystal deformation.*

III.1 Introduction

The banded polymer spherulite constitutes one of the most spectacular morphological patterns encountered in polymer science. Formation of banded spherulites has been attracting the interest of researchers since the very discovery of these magnificent morphological patterns characterized by long-range order. They can be observed with polarized light microscopy as concentric alternating dark and bright rings overlaying the conventional Maltese cross texture (cf. Figure III.1.1, top left).

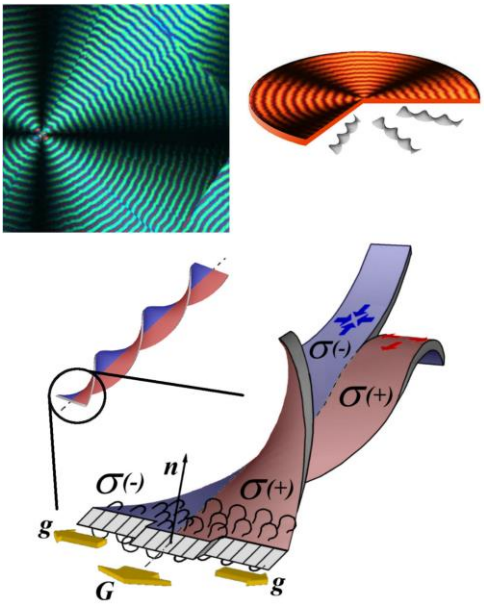

Figure III.1.1. Polarized optical micrograph of a banded spherulite of polytrimethylene terephthalate (**top left**). The colors in polarized light appear due to the three-axial indicatrix resulting in additional circular polarization of light. Cartoon depicting a quasi-2D spherulite with bands due to synchronous helicoidal twist of the crystalline lamellae (**top right**). Cartoon depicting the model of a twisted crystalline lamella according to *Keith* and *Padden* [1], in which the twist is generated by unbalanced surfaces stresses having different signs on opposite fold surfaces and on both longitudinal halves of the lamella (**bottom**).

The spatial scale of these patterns is undoubtedly unmatched in polymer science. Thus, the banded spherulites may be as large as several millimeters in diameter, whereas the band width varies with crystallization temperature from approximately one to several hundred microns. Here the appearance of spherulitic bands is attributed to propagation of synchronously twisting crystalline lamellae forming a locally *chiral* supramolecular

arrangement comprised of *chiral* or *non-chiral* macromolecules growing outward from the center of a "quasi-2D" schematically depicted in Figure III.1.1 (top right). In this case the dimensionality of the spherulite reflects the simple fact that the spherulite diameter is much bigger than its thickness. These racemic arrays of chiral lamellae are reminiscent of chiral packing motifs observed in liquid crystals [1,5], conglomerates [3], and nanofilaments[4] composed of non-chiral mesogens.

Identification of the mechanisms of the lamellar twist is notoriously difficult [4]. In their seminal papers [1,5], *Keith* and *Padden* proposed explanation of synchronously twisted lamellar growth based on unbalanced mechanical stresses generated on the lamellar surface. Most of the previous studies in the field were performed on thin films using Transmission Electron microscopy in imaging and diffraction mode. However, it is clear that the polymer microstructure in the bulk can be strongly different from that in thin films, which are amenable to electron diffraction. In particular, the spherulite banding might not be sufficiently developed in thin films, which makes the thin films studies not always directly relevant. Apart from the electron microscopy, *in-situ* observations of the banded spherulite microstructure and time-resolved development of the bands can be performed non-destructively with Atomic Force microscopy (AFM). In the past, AFM allowed temperature- and time-resolved imaging of the spherulite growth and provided structural information as to the shape and spatial organization of the crystalline lamellae [6,7,8,9]. Notwithstanding numerous extensive studies performed on banded polymer spherulites, quite a number of important questions remain open. For example, it is still unclear what the exact 3D shape of the twisted lamellae is and whether it can be well approximated by a helicoid characterized by a regular twist about its fast growth axis. To answer this question, a detailed analysis of banded spherulites in 3D space is badly needed. From this point of view, the 2D images resulting from surface-sensitive microscopy techniques such as Scanning Electron Microscopy and AFM can hardly suffice to fully characterize the spatial organization of the crystalline lamellae in the bulk.

Micro-beam X-ray diffraction has been intensively used to address the micro-structure of banded spherulites already starting from 1960s [10]. In more recent years, the technique has been implemented on modern synchrotron beam lines and was significantly improved in terms of spatial resolution and automatization of the experiment [11,12]. For studies of the banded spherulites, the main advantage of the X-ray micro-diffraction as compared to conventional Selected-Area Electron Diffraction (SAED) is that it can handle the samples that are thick enough to exhibit spherulite banding typical of the bulk. The information on

the 3D shape and packing of the twisted lamellar crystals is encoded in the details of the micro-diffraction intensity distribution such as the diffraction peaks asymmetry and angular broadening. Previously, arcing of the off-meridional reflections in the SAED patterns was used to address the shape of isolated helicoidal ribbons of a chiral polyester [13]. However, a more quantitative analysis of X-ray micro-diffractograms of twisted lamellar crystals in the perspective of their shape reconstruction in 3D still has to be developed.

The following chapter describes an unequivocal micro-beam X-ray diffraction analysis to disclose the nature and the origin of the spherulitic banding in poly(trimethylene terephthalate) in correlation to the seminal model of *Keith* and *Padden* denoted hereafter as *KP*-model [1]. In the *KP*-model lamellar twist was posited to result from a tilt of the chains relative to the basal lamella plane, which in turn, results in differential congestion of the chain folds on the lamella surfaces. The resulting positive (σ^+) and negative surface stresses (σ^-) induce twisting of the planar lamella crystal to alleviate stress. In Figure III.1.1(bottom right), we depict a lamellar crystal growing along its long axis |**a**| by condensing rows of folded chain stems into successive facets normal, or inclined at some angle to, |**a**| (with propagation rate ***g***) accreting fold surface on either side of the lamella giving overall growth rate ***G***. If one were to cut the crystalline lamella along |**a**|, the resulting strips would bend either up or down, depending on the sign of the surface stresses. Hence, the contiguous lamella reduces its mechanical energy by adopting a twisted helicoidal shape. Moreover, the *KP*-model implies that the handedness of the helicoid depends on the polarity of the crystal growth direction; e.g., left-handed when the chains are tilted to the left with respect to the lamellar normal ***n*** (looking in the growth direction (Figure III.1.1, bottom). In order to confirm the *KP*-model, one has to correlate the handedness of the lamellar helicoids with the growth axis polarity. But the determination of the latter is possible only for crystal lattices with low symmetry. For example, for polyethylene the discrimination between **b** and **-b** axes from diffraction experiments alone is impossible. Consequently this challenge has never been addressed for polymer spherulites.

The main idea of this chapter is to validate if the two main postulates from the *Keith* and *Padden* (*KP*)-model are applicable to the lamellar twisting in PTT, or if other models for twisting are possible i.e. that successive giant screw dislocations generated near the growth front are the origin of the lamellar reorientation.

The *KP*-model postulates that (1) the lamellar twisting is originated in unbalanced surface stresses rather than be generated by successive giant screw dislocations. (2) The origin of the unbalanced surface stresses is a difference in the chain folding in the lateral direction of the lamellar surface originated by obtuse and acute angle of the chain segment protruding the fold surface due to the inclination of the stem (chain tilt) in the lateral direction of the lamellar crystal.

A direct consequence of the second postulate from the *KP*-model is that the sense of the lamellar twisting needs to be opposite for the positive and negative growth direction, respectively. This originates from the fact that the chirality introduced by the lateral inclination of the stems is mirror-symmetric about the plane normal to the growth vector.

III.2 Experimental

III.2.1 Sample preparation

Poly(trimethylene terephthalate) (PTT) (Corterra CP 509200, Mw = 35200 g/mol, Mw/Mn = 2) films were prepared by crystallization from the melt at 170°C between cover glass slides resulting in films of approximately 40 µm thickness. Free-standing films were obtained by floating the films off on the water after immersion in 1% HF for 24 hrs. The unit cell of PTT is triclinic with the following parameters [14]: a=4.60, b=6.22, c=18.36, α=97.8°, β=90.8°, γ=111.3°. The space group is P-1 and the measured mass density of the unit cell is 1.35 g/cm^3.

III.2.2 Micro-beam X-ray diffraction

Micro-beam X-ray diffraction experiments have been carried out using an X-ray micro-beam diffraction facility at the ID13 beamline of the European Synchrotron Radiation Facility (ESRF) (Grenoble, France). The measurements were performed in transmission with the sample surface normal to the X-ray beam using the crossed-Fresnel optics and the wavelength of 1.0 Å. A MARCCD 165, with a pixel size of 80 microns (not rebinned) and a 16-bit readout was employed to record the 2D X-ray patterns. The spot size of the monochromatic X-ray beam at the focus point was 500nm along both axes. The norm of the scattering vector s ($s=2\sin(\theta)/\lambda$) was calibrated using several diffraction orders of silver behenate. The region of interest was selected with an on-axis optical microscope operated in reflection mode. Further refinement of the beam position on the sample was carried out using the azimuthal angles of the diffraction peaks on 2D diffractograms. A beam monitor installed upstream the sample provided dose-monitoring for online exposure normalization. The sample was scanned by means of an x-y gantry. The diffraction patterns were collected using a step of 1.0 µm. The data reduction and analysis including geometrical and background correction, visualization and the radial as well as the azimuthal integration of the 2D diffractograms were performed using home-build routines within the IgorPro® software package.

III.3 Results and Discussion

III.3.1 General characteristics of a twisting crystal

Figure III.3.1 (top right) displays a micro-focus X-ray diffraction, which was obtained by summing up several tens of frames acquired during a micro-beam scan along the radius of a banded spherulite of PTT shown with the yellow arrow (cf. Figure III.3.1, top left).

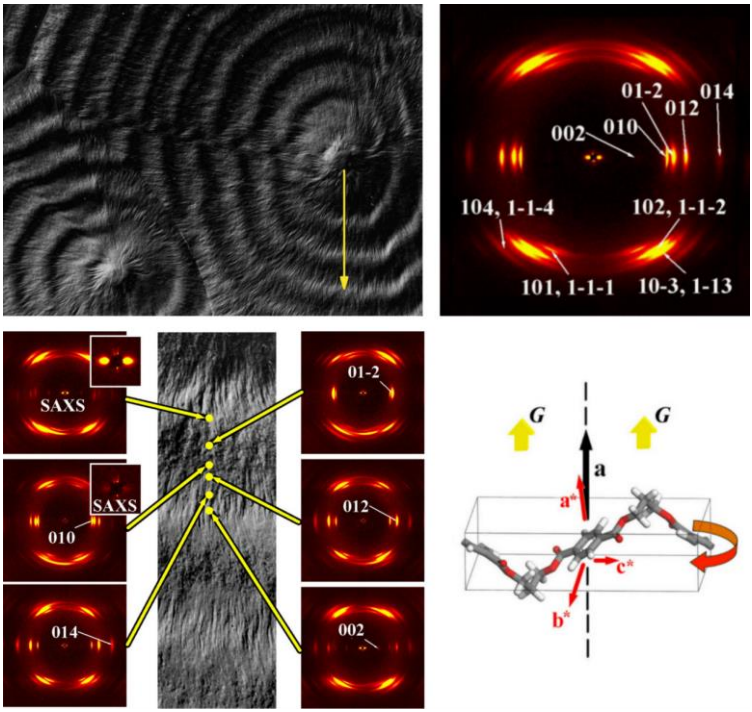

Figure III.3.1. Confocal scanning optical micrograph of a PTT free-standing film, as used for the microfocus X-ray experiments (**top left**). The film clearly shows the topographical features of a banded spherulitic texture. The direction of scanning is indicated by the yellow arrow. X-ray diffraction pattern summed up over the whole radial scan (**top right**). Set of X-ray diffraction patterns corresponding to the maximum intensity of the indexed reflection as a function of radial position relative to the banded morphology (**bottom left**). The radial direction of the spherulite is vertical. The fiber symmetry is formed by rotation of the growing crystal around its **a**-axis. The pattern exhibits numerous sharp reflections (**bottom right**). Their width and shape resemble more a diffractogram of a single crystal than that of a polycrystalline material such as an isotropic bulk sample of semicrystalline PTT. The azimuthal spread of the diffraction peaks is rather small, which signifies that, on the local scale, all the lamellae have essentially the same orientation [15].

By examining the indices of the peaks of the diffractogram it can be seen that the 0kl reflections are positioned on the equatorial direction, which means that the crystal growth direction (i.e., the meridian of the diffractogram) corresponds to the a-parameter of the PTT unit cell. This is in agreement with previous studies of PTT performed using SAED [16].Furthermore, the given averaged diffractogram (Figure III.3.1, top right) suggests a uniaxial symmetry as it is known for example for drawn fibers. However, in this case the rotation axis does not correspond to the chain axis of the polymer but to the crystallographic fast growth axis. A sketch of the corresponding model is given in Figure III.3.1 (bottom right) showing the orientation of the unit cell with respect to the uniaxial symmetry axis. Importantly, the WAXS patterns also allow observing the SAXS signal resulting from the PTT lamellar stacks in the edge-on orientation (Figure III.3.1). This is explained by a relatively small long period of the semicrystalline structure of PTT (i.e., less than 10 nm). The SAXS signal provides important additional information as to the orientation of the PTT chains with respect to the normal to the lamella basal plane.

Table III.3.1. Experimental and calculated Miller indices, distances, azimuthal and sagital angles (cf. Figure III.3.2 for the definition of φ) for the most intense reflections on the patterns in Figure III.1.1.

	h	k	l	dhkl Å	1/dhkl 1/ Å	1/dhkl* 1/ Å	azimuthal ρ deg	sagittal φ deg	sagittal φ* deg	
equator	0	1	0	5.692	0.1757	0.175	90.0	ref	ref	
	0	1	-2	5.185	0.1928	0.191	90.0	33.9	35	
	0	1	2	4.558	0.2194	0.220	90.0	28.8	29	
	0	1	4	3.352	0.2983	0.293	90.0	45.1	47	
	SAXS			-	-	0.03	-	-	84	
first layer line	1	0	1	4.170	0.239	0.243	27.2	31.2	n.a.	} doublet
	1	-1	-1	4.082	0.245		27.5	153.6		
	1	0	-2	4.024	0.249	0.252	29.9	56.8	54	} doublet
	1	-1	2	3.916	0.255		31.7	123.6		
	1	0	2	3.838	0.261	0.263	35.2	46.9	n.a.	} doublet
	1	-1	-2	3.778	0.265		35.0	136.6		
	1	0	-3	3.652	0.274	0.277	37.9	69.5	67	} doublet
	1	-1	3	3.563	0.281		39.4	111.4		
	1	0	-4	3.260	0.307	0.308	45.1	76.7	78	} doublet
	1	-1	4	3.191	0.313		46.3	104.3		

* experimentally measured values

The idea of a single-crystal-like texture of the lamellar stacks is supported by the crystal orientation probed on the local scale by the X-ray micro-beam given in Figure III.3.1 (bottom left). The set of X-ray diffraction patterns is representative of situations where the indicated reflections reach their maximum intensity in the course of the radial scan. In the first such point the SAXS signal has its maximum while the (010) reflection is almost undetectable. Approximately at halfway between the two edge-on regions where

the (010) reflection reaches its maximum, the SAXS signal completely disappears. This corresponds to the flat-on orientation of the PTT crystals. Generally, the periodic appearing and disappearing of diffractions peaks reflects the periodic change in the crystal orientation as a function of the radial distance, while in none of the patterns all reflections coexist.Among the observed reflections, the most intense ones are the (010), (01-2) and (012) lying on the equatorial direction and the doublets (102, 1-1-2), (10-3, 1-13) and (104, 1-1-4) located on the first layer line. The calculated and measured spacings are given in Table III.3.1.

The calculated spacings and the norm of the scattering vector **s** are given for the different peaks including the azimuthal angle $\boldsymbol{\rho}$**,** i.e. the angle between the arbitrary reciprocal-space vector **hkl** and the meridional **a**-axis, as well as the fiber angle $\boldsymbol{\varphi}$**,** i.e. the angle between the projections of the arbitrary reciprocal-space vector and the 010 vector in the plane normal to **a** (cf. Figure III.3.2). The Table shows that the measured values of the spacings and angles are in good agreement with the theoretical values.

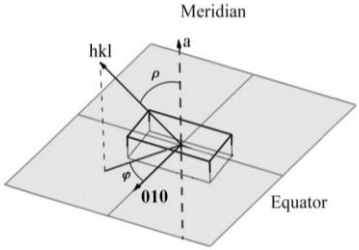

Figure III.3.2. Schematic drawing of an arbitrary reflection hkl and its angle with respect to the meridian **a** (azimuthal angle $\boldsymbol{\rho}$) and the angle between the projections the hkl vector on the plane normal to the meridian and 010 vector (fiber angle $\boldsymbol{\varphi}$).

Notwithstanding the triclinic symmetry of the PTT lattice, the layer lines can still be identified on the micro-diffraction patterns. The intense reflections visible on the first layer line appear in doublets with characteristic indices such as *h*0*l*, *h*-1-*l*. The doublets completely merge on reduced 1D diffraction curves (Figure III.3.4) because the *d*-spacings of the peaks of each doublet are very close. The azimuthal angle $\boldsymbol{\rho}$ (i.e., the angle between the reciprocal lattice vector and **a**-axis) of the duplets are identical, meaning that it is not possible to differentiate the peaks on a single 2D pattern neither. Upon examination of the two fiber angles $\boldsymbol{\varphi}$ it appears that they are supplementary, i.e. giving 180 deg when added up. This means that they are lying in one plane together with the rotation axis **a** as depicted in Figure III.3.3.

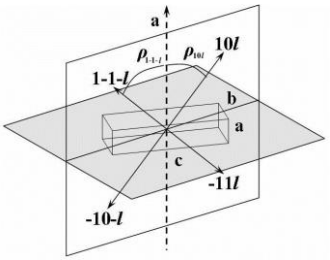

Figure III.3.3 Cartoon showing the position of the off-meridional doublets of the first layer line in respect to the **a**-axis (dotted arrow). The two corresponding vectors and the **a**-axis are lying in one plane (depicted in gray), while the azimuthal angle $\boldsymbol{\rho}$ is almost identical for the two corresponding vectors.

This fact directly stems from the unit cell parameters of PTT, and adds an additional quasi-symmetry element to the low-symmetry P-1 unit cell. Due to this fact, the two reflections cannot be analyzed separately, even being present on different 2D micro-diffraction patterns acquired during a radial scan. Therefore, the doublets will be considered as one peak in our further analysis, which is similar to the phenomenon of multiplicity for higher-symmetry lattices.

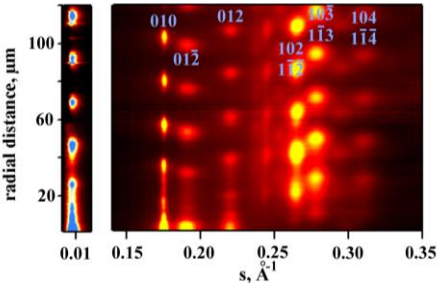

Figure III.3.4. Radially integrated scattering intensity for the SAXS (**left**) and WAXS (**right**) angular regions as a function of radial distance from the spherulite center for a PTT sample melt-crystallized at 170°C. The graph shows regular appearance of all the observed PTT reflections.

The reduced 1D-diffraction curves are given in Figure III.3.4 as a function of the radial distance and the norm of the reciprocal vector s. The Miller indices of the main diffraction peaks are indicated on the graph. The subsequent and repetitive appearances of the strong reflections throughout the scan are clearly visible. It is remarkable that the distance between two adjacent maxima is identical for all the peaks including the SAXS interference peak.

The normalized intensity of the most intense reflections belonging to the equator and first layer line are given in Figure III.3.5. When plotted as a function of the radial distance, the intensity of diffraction peaks exhibits a clear oscillation behavior for the peaks periodically enter and exit the reflection conditions.

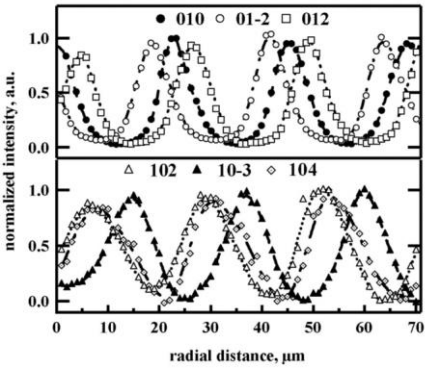

Figure III.3.5. 1D-plots of the radially-integrated diffraction intensity of the most intense equatorial (**top**) and first layer line (**bottom**) reflections as a function of the radial distance from the spherulite center. The graphs reveal a characteristic periodic behavior in the WAXS region resulting from rotation of the reciprocal-space vectors moving in and out of the reflection conditions.

The latter are reached at different positions for the different peaks, as it is expected for a single-crystal-like sample rotated about one of its crystallographic axes. The occurrences of the main diffraction peaks maxima are given in Figure III.3.6 (right).

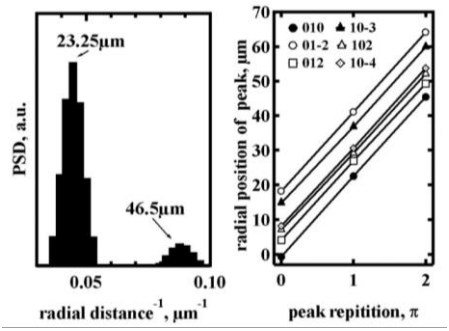

Figure III.3.6. Power spectral density function (PSD) computed for the integral diffraction intensity of selected peaks as a function of radial distance (**left**). The PSD shows a period of crystal rotation of 23.25μm. Radial positions of the reflection maxima for several intense PTT peaks as a function of rotation period clearly show linear behaviour (**right**). The latter provides support to the model of continuous rotation of the crystal and thus to a regular and uniform twisting of the lamella.

Plotting the radial peak position as a function of the number its cycle allows illustrating that the lamellar twisting is regular and uniform. The twist period given by the slope of the curves is identical for all the studied reflections.The power spectral density functions, PSD, calculated from the intensity dependences display a relatively sharp maximum at 23.25 microns (Figure III.3.6, left), which equals half period of the lamellar twist.The second weaker maximum corresponds to the second harmonics of the main peak, i.e. the full twist period of the lamella. The twisting period derived from the X-ray data is in full agreement with the pitches measured by optical microscopy which will be discussed further in chapter IV.

III.3.2 Determination of the growth axis polarity

By keeping in mind that the twist is regular and continuous, it is possible to calculate the phase shift of the different reflections using the twisting period and radial distance of the particular reflection.

The phase shift of the equatorial reflections as a function of the crystallographic angle relative to the (010) reflection (i.e., the fiber angle φ as given in Table III.3.1) are summarized in Figure III.3.7 (left).

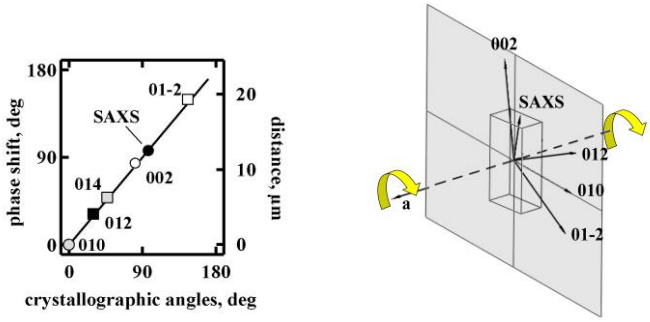

Figure III.3.7. Radial distance and phase shift of the different equatorial reflections as a function of the crystallographic angle of the corresponding reciprocal-space vectors with respect to the 010 peak (**left**). Sketch illustrating the lamellar crystal rotation about the crystallographic **a**-axis (**right**). The equatorial vectors of the 0kl reflections rotate in the **b*c***-plane. The sense of the crystal rotation is indicated by the yellow arrows.

The distinctly linear behavior of the curve shows that the lamellar stacks have indeed a single-crystal-like local-scale texture and uniformly rotate around the growth axis **a**. Thanks to the triclinic nature of the unit cell, it is possible to derive the sense of the crystal

rotation using the sequence of appearance of the equatorial peaks. Thus, the sequence of peak appearance of (01-2) → (010) → (012) indicates a **clockwise** rotation of the crystal when looking along **-a** (dashed line), as depicted in Figure III.3.7 (right). The equatorial reflections rotate in the **b*****c***-plane (gray parallelogram), which is normal to the **a**-axis. From this fact it follows, that the handedness of the growing lamellar stacks should be linked to the growth direction polarity, as it is originally proposed by *Keith* and *Padden* [17]. Therefore, to verify the *KP*-model it is compulsory to experimentally determine the correlation between the handedness of a particular lamellar stack and its growth-axis polarity.

Figure III.3.8 depicts the *Ewald* sphere construction showing the conditions of observation of an arbitrary diffraction peak. Thus, in this case the corresponding reciprocal space vector should make an angle θ (Bragg angle) with the plane (gray parallelogram) perpendicular to the incident X-ray beam direction (red arrow). During twisting of the crystalline lamella, the symmetric diffraction peaks (i.e., 0kl and 0-k-l) will enter the reflection conditions at different moments.

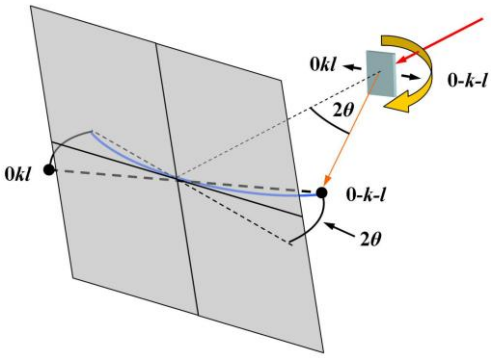

Figure III.3.8**.** Cartoon depicting the *Ewald* sphere construction, which allows determining the handedness of the lamellar helicoid from the positions of the maximum intensity of symmetric reflections, e.g., 0kl and 0-k-l. The equatorial section of the *Ewald* sphere is indicated by the blue arc. The position of the reciprocal space vector on the *Polanyi* sphere [18] is given by the black spheres. The rotation direction of the sample indicated in light blue is shown with the yellow arrow.

In particular, for a right-handed helicoid, which is scanned downwards, the peak on the right side of the detector should appear before its symmetric counterpart on the left side of the detector. The angular distance between the maxima of the two peaks should

equal twice the Bragg angle, i.e. 2θ. Thus, the finite curvature of the *Ewald* sphere provides a means to discriminate the lamellar helicoids according to their handedness.

Figure III.3.9 shows the peak intensity and azimuthal position of the equatorial 010 reflection as a function of the radial distance from the spherulite center corresponding to the scan shown in Figure III.3.4.

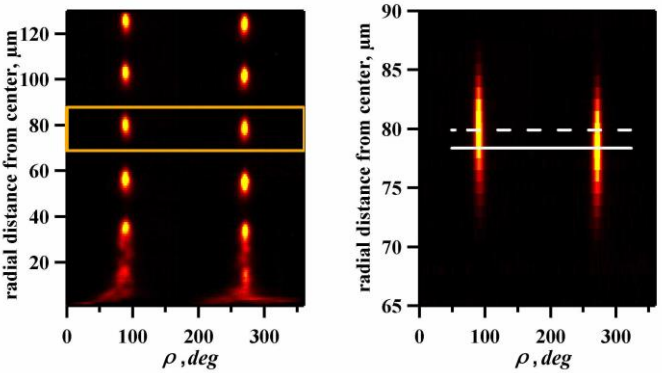

Figure III.3.9**.** Intensity and azimuthal position of the equatorial 010 reflection as a function of the radial distance from the spherulite center showing no azimuthal wagging (**left**). The reflection on the right side of the detector (i.e., at an azimuthal angle ρ of 270 deg) appears slightly before the left-side reflection (i.e., at ρ equal 90 deg). This indicates a right-handed rotation of the crystal about the **a**-axis (cf. Figure III.3.8) when the lamella grows downward (**right**). The relative phase shift in the peak appearance corresponds to twice the corresponding Bragg angle of the peak.

Besides the oscillation of the reflection intensity, the reflection position is strictly on the equatorial direction at 90 deg and 270 deg if the meridian corresponds to 0 deg. In the figure, the reflection at 90 deg corresponds to the one showing up on the right side of the detector while the left reflection appears at 270 deg when looking upstream the X-ray beam. The diffuse and not regular appearance close to the center is due to the finite thickness of the film of about 30 microns allowing the helicoids to grow inclined towards the film surface resulting in randomized azimuthal orientation of reflections. In addition the local variation of orientation drastically enhances close to the spherulite center. Since the focused beam has a finite size it detects all crystal orientations within the irradiated volume. The equatorial peaks do not show any wagging around the equator indicating that, within the precision limits of the measurement, the lamellar shape is not helical but helicoidal.

When examining in more detail the appearance of the left- and right-side reflections (cf. Figure III.3.9, right) it appears that on the right side of the detector the peak shows up slightly before its left counterpart, having a difference of 1.5 microns. When recalculated in terms of the phase angle (app. 10 deg), this difference corresponds to twice the Bragg-angle of the (010) reflection for the given wavelength. It also means that the studied helicoid is right-handed. Together with the rotation sense of the crystal it follows that growth axis polarity is (**-a**). The corresponding vector model is depicted in Figure III.3.10.

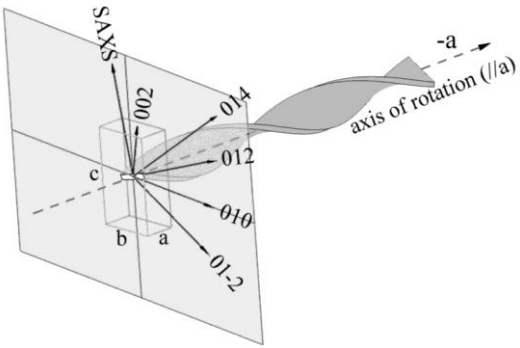

Figure III.3.10. Vector model of the lamellar crystal rotation allowing to correlate the crystal orientation and rotation direction with the growth direction.

If there would be no preferred growth-axis polarity, both polarities should be observable with the same probability, although not necessarily within the same spherulite. In order to check this, additional scans were performed on tens of PTT spherulites. The integrated 1D-diffraction curves for two whole spherulites scanned past the center are given in Figure III.3.11 as a function of the radial distance from the spherulite center.

Remarkably, when scanning from the spherulite center outwards, the most intense diffractions reveal the same sequence, i.e. the 01-2 peak is followed by 010 and then by 012 peaks. Thus, the crystal rotation direction within the **b*c*** plane is identical, independently of whether the crystal growth occurs in **a** or (**-a**) direction.

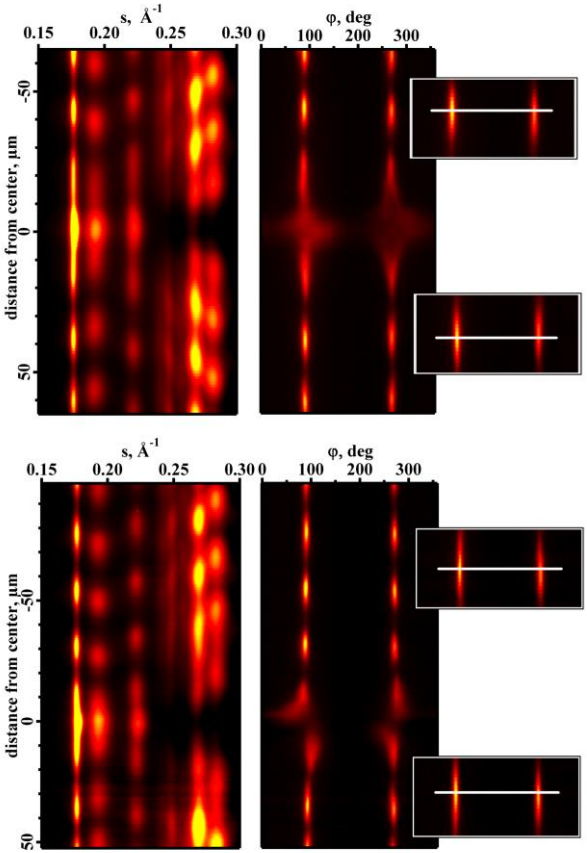

Figure III.3.11**.** Integrated 1D-diffractograms corresponding to two PTT spherulites crystallized from the melt at 170°C. The diffracted intensity is plotted as a function of the distance from the spherulite center. The lag between the equatorial 010 and 0-10 reflections allows determining the handedness of the lamellar twist. **Top**: The handedness is different in the upper and lower parts of the spherulite. Above the spherulite center, the lamellar helicoid is left-handed, while in the lower part it is right-handed. **Bottom**: The twist sense is left-handed in both parts of the spherulite.

The analysis of the helicoid's handedness using the *Ewald* sphere curvature (cf. Figure III.3.8) shows that in one of the cases the helicoids have different handedness above and below the spherulite center (cf. Figure III.3.11, top). By contrast, the handedness is identical in the other case (cf. Figure III.3.11, bottom). Therefore, the right-handed helicoids grow in the (-***a***)-direction, while for the left-handed helicoids the growth direction is ***a,*** as schematically depicted in Figure III.3.12.

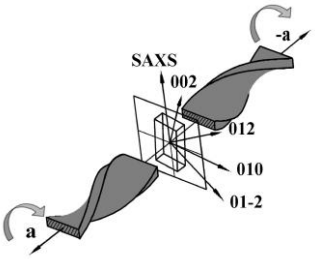

Figure III.3.12 Vector model illustrating the rotating unit cell. The axis of rotation corresponds to the crystallographic **a**-axis. All 0kl reflexes rotate about **a** in the plane perpendicular to **a**. The light gray arrows indicate the rotation direction of the unit cell. The sense of twist is right for growth along the negative growth direction (**-a**) while it is left for the positive direction (**a**).

III.3.3 Orientation of the unit cell within the lamellar ribbon

Having been able to discriminate the two growth axis polarities, it becomes now possible to check whether the second premise of the *KP*-model given in the introduction section of this chapter is valid for the case of PTT, i.e. that the chain tilt to the right induces right-handed lamellar twist when seen along the lamellar growth axis cf. Figure I.2.7. Therefore it is necessary to analyze the phase angle of the SAXS signal with respect to other equatorial reflections.

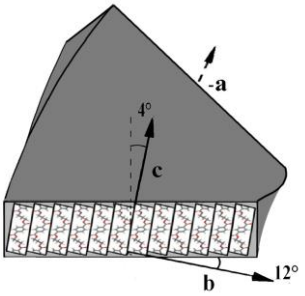

Figure III.3.13. Orientation of the unit cell relative to the lamellar basal plane showing the inclination of the chain stems of about 4 degrees along **b*** and inclination of the **bc**-plane for about 12°.

Figure III.3.7 (left) shows that the SAXS signal does not appear simultaneously with the (002) reflection indicating that the lamellar basal plane does not correspond to the **ab-** plane of the crystal, as was suggested in [16]. Instead it is inclined in the plane perpendicular to **a**. Recalling that the angle between **a** and **c** is close to 90 deg, the chain tilt in the **a**-direction can be neglected. Using the strong equatorial reflections it is possible to derive the inclination of the unit cell in the plane perpendicular to **a** and thus the chain tilt in this direction. Also, by considering not only the absolute value of the phase angles but in addition their direction deduced from the order of the peaks, it becomes possible to derive the direction of the chain tilt. The phase angle of the SAXS signal towards the (010) reflection is 84 deg (see Table III.3.1), which corresponds to inclination of the **ab-** plane for about 12 deg in the positive **b**-direction. Therefore, the chain tilt is about 4 deg in this direction, as depicted in Figure III.3.13.

III.4 Conclusions

The use of micro-beam X-ray diffraction to studies of the banded spherulites texture is discussed for poly(trimethylene terephthalate). It is shown that this technique allows identifying the crystal growth direction and characterizing the crystal orientation on the local scale. It is shown that the different diffraction peaks have the same periodicity as a function of the distance to the spherulite center, which means that the lamellar twist is strictly uniform and regular. The latter observation is more compatible with the model explaining the twist as a result of unbalanced surface stresses than the giant screw dislocations.

The regular band periodicity is the only morphology exhibited by homopolymers that has long-range order on a macroscopic spatial scale. Our data shows that non-chiral polymers are in fact not indifferent to the inversion of the lamellar handedness, and that a change in the handedness is necessarily accompanied by a change in the sign of the growth vector. Furthermore, the experimental observations appear to be consonant with the *KP*-model, namely that the lamellar twist is driven by surface stresses [1,5].

Further studies on the twisting crystalline lamellae including determination of the growth axis polarity and their exact 3D-shape [15] are expected to provide more insights into the nature of chirality in supramolecular objects formed by non-chiral polymers.

REFERENCES

1 Keith H. D. and Padden F.J. 1984 Polymer, 25, 8.
2 Bassett D.C., Hodge A.M. 1979 Proc R Soc Lond, A359,121.
3 Bassett D C and Hodge A.M. 1978 Polymer 19, 469.
4 Lotz B. and Cheng S.Z.D. 2005 Polymer 46, 577.
5 Keith H.D., Padden F.J., Lotz B. and Wittmann J.C. 1989 Macromolecules 22, 2230.
6 Ivanov D.A., Nysten B. and Jonas A.M. 1999 Polymer 40, 5899.
7 Basire C. and Ivanov D.A. 2000 Phys. Rev. Lett. 85, 5587.
8 Ivanov D.A., Amalou Z. and Magonov S.N. 2001 Macromolecules, 34, 8944.
9 Ivanov D.A., et al., 2008 Macromolecules 41, 9224.
10 Fujiwara Y. 1960 J. Appl. Polym. Sci. 4 10.
11 Gazzano M., et al., 2001 Macromol. Chem. Phys. 202 1405.
12 Tanaka T., et al., 2005 Polymer 46 5673.
13 Li C.Y., et al., 1999 Phys. Rev. Lett. 83 4558.
14 Hall I.H., Structure of crystalline polymers London: Elsevier Appl.Sci. 1984, p.39.
15 Luchnikov, V.A. and Ivanov, D.A. 2009 Journal of Appl. Cryst., 42, 673.
16 Ho R.-M., Ke K.-Z. and Chen M. 2000 Macromolecules 33 7529.
17 Keith H.D. and Chen W.Y. 2002 Polymer;43,6263.
18 Striebeck N. and Nöchel U., 2009 J. Appl.Cryst. 42, 295.

IV. HELICOIDAL LAMELLAR TWIST IN MELT-CRYSTALLIZED POLY(TRIMETHYLENE TEREPHTHALATE): MICRO-STRUCTURAL EVOLUTION AS A FUNCTION OF CRYSTALLIZATION TEMPERATURE

Martin Rosenthal[1], Denis V. Anokhin[1], Richard Davies[2], Manfred Burghammer[2], and Dimitri A. Ivanov[1]

1) Institut de Sciences des Matériaux de Mulhouse, CNRS LRC7228, 15 rue Jean Starcky, 68057 Mulhouse, France

2) European Synchrotron Radiation Facility (ESRF), 6 rue Jules Horowitz, 38043 Grenoble, France

Abstract

In this chapter, the chirality parameters required for the description of the twisting crystalline lamella at different spatial scales and exploring the correlations between them are identified. It was proposed in the literature that non-chiral polymers can form lamellar helicoids of both handedness, whereas chiral polymers are documented to form only one type of helicoids (i.e., either right- or left-handed). By performing an in-depth structural analysis on banded PTT spherulites with micro-focus X-ray diffraction, we show that the reality is more complex and that even non-chiral polymers are in fact not indifferent to the inversion of the lamellar handedness. As far as the KP-model is concerned, in this study we verify the correlations between the handedness of the lamellar helicoids and the chain tilt direction. In the course of discussion, it becomes clear that the model cannot explain certain features of the PTT spherulites banding behavior, where the handedness of the lamellar twist can inverse with crystallization temperature. Finally, we used the banded spherulites of PTT to explore the structural memory inherited by the lamellae. By designing a special experiment in which the crystallization temperature is changed stepwise, we identified the structural parameter that the lamellae transfer over hundreds of microns during their radial growth.

IV.2 Introduction

Spherulites of many melt-crystallized polymers reveal regularly-spaced concentric birefringent patterns (i.e., bands) when observed in polarized light. A great number of studies have been devoted to spherulitic banding in polymer crystallization, starting with pioneering works of *Point* [1], *Keith* and *Padden* [2] and *Keller* [3]. According to *Keith* and *Padden* [4], the concentric extinction patterns of synchronously twisting lamellar crystals were correlated to the torsional stresses within the lamella. If one recalls that the chains folds consume a larger cross-section than the crystalline stems [5], it would be logical to associate the origin of the torsional stresses in thin lamellar crystals with chain folding. Also, due to a presumably anisotropic direction of the chain folds, the surface stresses will be unbalanced, with preferred orientation according to the chain folding direction [6].

The model of the lamellar twist put forward by *Keith* and *Padden* (*KP*-model) [4] suggests that the torsional stresses result from the different congestion of the chain folds on the lamellar basal planes. This is generated in turn by the chain tilt which adds a chiral element to the lamella structure. The *KP*-model is discussed in more detail in Chapter I. *Keith* and *Padden* [7] suggested a gradient of the driving force of crystallization caused by the diffusion field at the growth front of the polymer crystal resulting in the possibility of a morphological instability, which causes the crystal branching. A model discussed by *Toda* [8] assumes, that the branching instability of the growth front and the reorientation of the branches driven by the torsional stresses results in helical twist of the lamellar crystals. However, the correlation between the chirality of the structure at different scales is still a matter of debate. It is often assumed that non-chiral polymers can form lamellar helicoids of both handedness, whereas chiral polymers are documented to form only one type of helicoids (i.e., either right- or left-handed). The reasons for the choice of the handedness of the lamellar helicoids are not yet understood.

Synchrotron micro- and nano-beam X-ray diffraction has been recently proven to be a powerful technique for morphological studies of polymer materials. In the case of polymer spherulites exhibiting bands, it allowed exploration of such local-scale morphological features as crystal growth direction, crystal orientation and degree of order [9,10].

In the present work, we are going to employ the micro-focus X-ray diffraction for in-depth analysis of the banded spherulites microstructure in view of identification of the twisted growth mechanisms. In particular, we will verify the correlations between the

chirality of the lamellar helicoids and the chain tilt direction, as stipulated by the *KP*-model. In the course of discussion, it will become clear that this model cannot explain certain features of the PTT spherulites banding behavior, where the chirality of the lamellar twist can inverse with temperature. In an attempt to explain our observations, we are going to correlate the complex temperature dependence of the banding behavior with the lamellar thickness.

IV.3 Experimental

IV.3.1 Sample preparation

Poly(trimethylene terephthalate) (PTT) (Corterra CP 509200, Mw = 35200 g/mol, M_w/M_n = 2) films were prepared by isothermal crystallization from the melt at 170, 180, 190, 210 and 215°C between cover glass slides resulting in films of approximately 40 µm thickness. In addition, non-isothermal crystallization experiments were conducted where the temperature programs contained temperature jumps from 170 to 190°C and *vice versa*. Free-standing films were obtained by floating off the films on water after immersion in 1% aqueous solution of HF for 24 hrs.

The unit cell of PTT is triclinic with the following parameters: a=4.60, b=6.22, c=18.36, α=97.8°, β=90.8°, γ=111.3° [11]. The space group is P-1 and the theoretical mass density of the unit cell is 1.35 g/cm^3.

IV.3.2 Micro-beam X-ray diffraction

Micro-focus X-ray diffraction experiments have been carried out using micro-beam facility at the ID13 beamline of the European Synchrotron Radiation Facility (ESRF) (Grenoble, France). The measurements were performed in transmission with the sample surface normal to the X-ray beam using the crossed-Fresnel optics and wavelength of 1.0 Å. A Frelon fast CCD, with a pixel size of 50 microns (not rebinned) and a 16-bit readout, was employed to record the 2D X-ray patterns. The spot size of the monochromatic X-ray beam at the focus point was about 1.0 micron along both axes. The norm of the scattering vector s (s=2sin(θ)/λ) was calibrated using diffraction pattern of corundum. The region of interest was selected with an on-axis optical microscope operated in reflection mode. Further refinement of the beam position on the sample was carried out using the azimuthal angles of the diffraction peaks on 2D diffractograms. A beam monitor installed upstream the sample provided dose-monitoring for online exposure normalization. The sample was scanned by means of an x-y gantry. The diffraction patterns were collected using a step of 1.0 µm. The data reduction and analysis including geometrical and background correction, visualization and the radial as well as azimuthal integration of the 2D diffractograms were performed using home-built routines designed in Igor Pro software (Wavemetrics Ltd.).

IV.3.3 Small-Angle X-ray Scattering

Small-angle X-ray scattering experiments were performed on the A2 beamline, at HASYLAB/DESY (Hamburg Germany). The measurements were conducted in transmission. The PTT films were wrapped in aluminum foil to provide good temperature contact. The bulk samples were melted at 250°C for 5 min and quickly cooled to the desired crystallization temperature. The sample was allowed to crystallize for 10 up to 40 min depending on the setpoint temperature. The 2D SAXS patterns were recorded using a MARRCCD positioned approximately 1.2 m downstream the sample. The sample stage including heating equipment was placed in vacuum to avoid parasitic air scattering. For calibration, eight orders of rat tail collagen diffraction were used. The data reduction and analysis including background correction, radial integration as well as calculation of the 1D-correlation (CF) and interface distribution (IDF) functions were performed using home-built routines. The calculation of the CF and IDF was performed using the approach described in detail in Chapter I.

IV.4 Results and Discussion

IV.4.1 Spherulite band spacing as a function of crystallization temperature

A set of polarized optical micrographs of PTT films crystallized at temperatures ranging from 130 up to 210°C are displayed in Figure IV.4.1. The colors in the images measured in crossed polarized light originate from the fact that PTT is characterized by a strong birefringence as reported by *Yun* and co-authors [12]. Due to this the PTT film can cause a phase shift on the order of $\lambda/4$ resulting in a circularly polarized light [13]. The amount of the phase shift obviously depends not only on the sample thickness but also on orientation of the optical indicatrix with respect to the incidence direction. Therefore the observed colors display important variations from one sample to another. To derive the correct band spacing from the optical micrographs it is important to analyze the original color images, since conversion to the grayscale can lead to misinterpretation.

Figure IV.4.1 shows a significant variation of the spherulite band spacing with crystallization temperature. The bands are very tight at 140°C, where the spacing is on the order of a few microns (cf. insert of the figure), while they increase up to several hundred microns at 175°C. It is noteworthy that below 140°C no banding is visible in optical micrographs. At around 180°C, one is unable to observe the bands as they exceed the spherulite diameter. Surprisingly, at higher temperatures the banding reappears.

The banded spherulite morphologies also differ in terms of the lateral coherence. Thus at low crystallization temperatures ranging from 140 up to 170°C, the bands show a strong lateral coherence of twisting, which is reflected by smooth concentric rings. With increase of crystallization temperature the jaggedness of the bands strongly increases. A simple explanation of this fact can be that the flatter are the lamellar ribbons the easier will be their radial offset relative to each other, resulting in a de-phasing of the bands at the lamellar boundaries. Thus the lateral correlation of the lamellar stacks weakens with increase of the band spacing. Starting from approximately 180°C, the band spacing starts to decrease again, being accompanied by improvement of the lateral correlation.

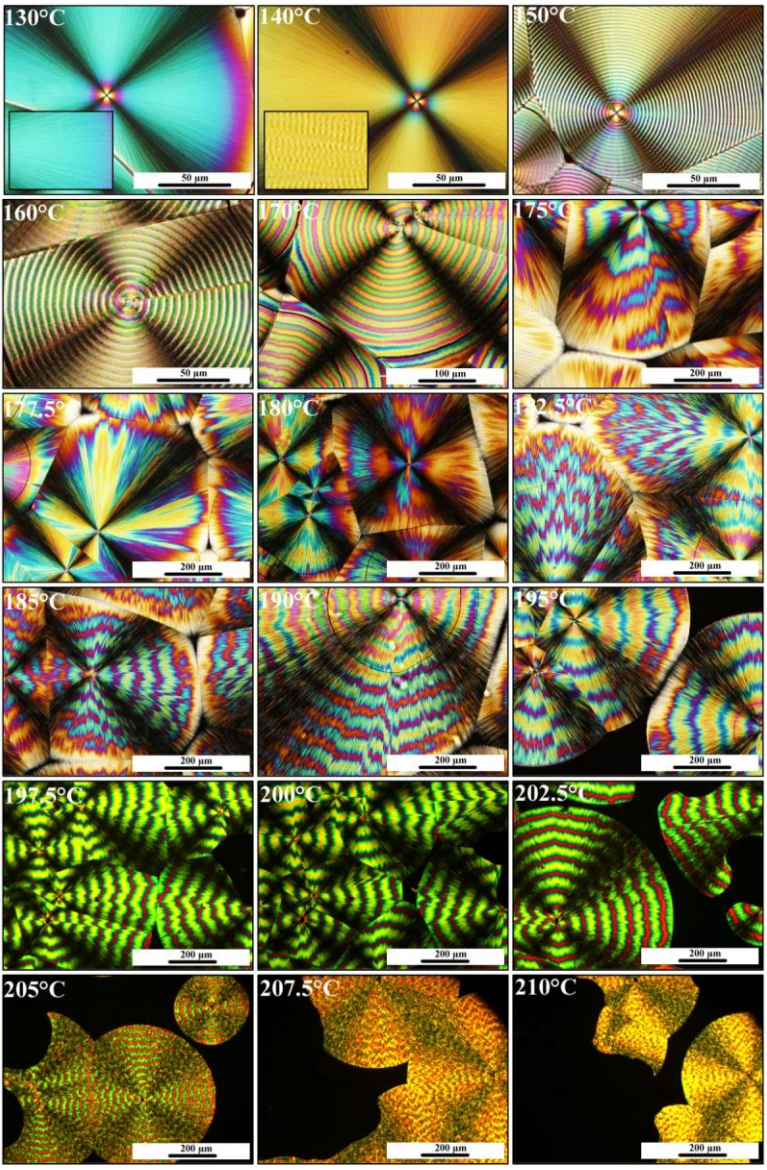

Figure IV.4.1. Polarized optical micrographs of PTT spherulites grown from the melt at various temperatures in the range of 130 to 210°C. The images are used to evaluate the crystallization temperature dependence of the band spacing.

At crystallization temperatures above 205°C, the banded spherulites texture abruptly changes when the spherulite colors turn brownish. This makes difficult the exploration of the spherulites bands based on the color contrast alone. The variation of the band spacing as a function of crystallization temperature obtained from the optical microscopy data is given in Figure IV.4.2.

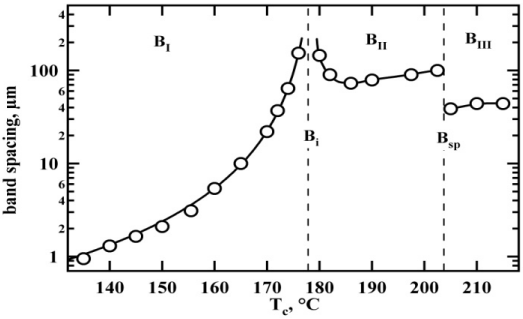

Figure IV.4.2**.** Band spacing of isothermally-crystallized PTT as a function of crystallization temperature plotted in semi-logarithmic coordinates. The graph reveals two singularity points at 178.5°C and 202.5°C. The first point can be mathematically identified as a pole of the function while the second one corresponds to a step-wise variation. The band spacing increases monotonically from 140 to 179°C following the power law. After reaching the singularity point, the band spacing starts to decrease up to 187°C, subsequently followed by a weak increase. At approximately 202.5°C the band spacing drops by about one half, followed again by a steady increase. Banding at crystallization temperatures below 135°C could not be observed using optical microscopy because of insufficient resolution.

Remarkably, the curve shows two singularity points of different nature. The first singularity point at around 179°C can be characterized as a mathematical pole of the function. In this work, it will be denoted as $\mathbf{B_i}$, where "i" stands for banding inversion, to be explained further in the text. The second singularity at 202.5°C simply shows a step-wise variation, and will be termed $\mathbf{B_{sp}}$, where "sp" stands for singularity point. It can be seen that starting from 140°C the band spacing drastically increases. Above the singularity point B_i the band spacing starts to decrease up to 185°C, followed by a weak increase. At approximately 202.5°C, the band spacing drops significantly by about one half followed by a steady increase. Banding at crystallization temperatures below 135°C cannot be observed using optical microscopy because of the resolution issue. The AFM images displayed in Figure IV.4.3 clearly show the twisted lamellar morphology for the film

crystallized at 140°C while there is no such feature for the film crystallized at 135°C. Thus, the onset of banding is between 135°C and 140°C.

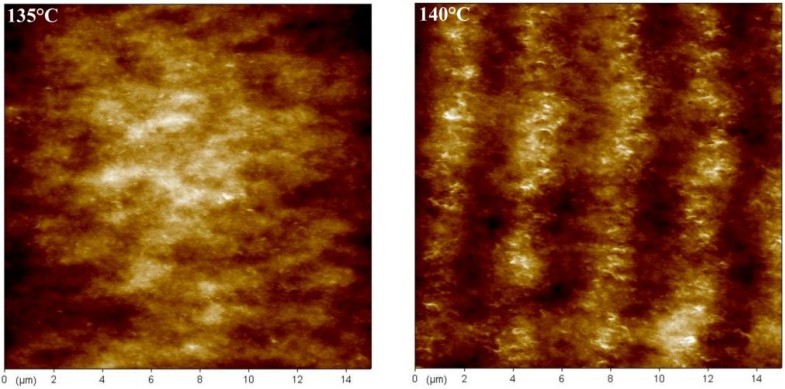

Figure IV.4.3. AFM images of the free-standing films of PTT crystallized from the melt at 135°C (**left**) and 140°C (**right**). The micrograph in the left panel does not reveal any banded spherulite morphology.

The initial increasing branch of the band spacing, i.e. the curve before temperature $\mathbf{B_i}$, can be nicely fit to the power law function as follows

$$p = \frac{A}{(T_{CR} - T)^n} \qquad \text{(E.IV.4.1)}$$

In equation (E.IV.4.1), p is the band spacing, T_{CR} is the temperature corresponding to $\mathbf{B_i}$ and A is a constant. The best set of parameters found from the fit are T_{CR} = 178.5°C and n=2. Interestingly, in the past, there were already attempts to describe the temperature dependence of the band spacing using the same type of function. Thus, *Chuang*, et al. [14] found that the critical exponent (i.e., n) equals 0.5, which, in his view, could be compared to the well-known critical exponent of the order parameter in the mean-field theory of the equilibrium phase transitions [15,16]. For unknown reasons, our results strongly differ from those of *Chuang*, this difference being not only in the value of *n* but also in the temperature window of the existence of banded PTT spherulites. Thus, these authors observed that the banded-nonbanded (BNB) transition for PTT occurs at 195°C on the low temperature side and at ca. 215°C on the high temperature side [17]. Compared to our data, the referenced low-temperature BNB transition occurs approximately 60°C higher.

Importantly, the results of *Chuang* and *Hong* [31, 34] are also strongly different from other reports on PTT. Thus, *Wu* and *Woo* [18] report the BNB transitions of PTT to occur at 150 and 215°C, which is closer to our findings. By contrast, in the work of *Wang*, et al. [19], the temperature window of the banded morphology is reduced, occurring within 135 and 165°C. Therefore for unidentified reasons the literature reports on the PTT banding are not consistent.

IV.4.2 Crystal growth rate and onset of banding

To correlate the band spacing behavior to the crystallization kinetics, similar to what was done by *Hong*, et al. [34] and *Chuang*, et al. [31], linear growth rate measurements were performed.

The temperature dependence of the linear growth rate G shows a typical bell-shaped curve in semi-logarithmic coordinates as shown in Figure IV.4.4. Fitting the temperature dependence of *G* using the *Hoffman-Lauritzen* approach could make it possible to extract important thermodynamic and kinetic parameters and determine the growth regimes. A general expression extensively used in the analysis of the linear growth rates [20] reads as follows

$$G_{(i)} = G_0 \exp\left[-\frac{U^*}{R(T-T_\infty)}\right]\exp\left[-\frac{K_{g(i)}}{T(\Delta T)f}\right] \qquad \text{(E.IV.4.2)}$$

In equation (E.IV.4.2) U^*corresponds to the activation energy of reputation, K_g denotes the activation energy of nucleation for a crystal with a critical size, which strongly depends on the undercooling, G_0 is a pre-factor that can be defined experimentally, T_∞ stands for the thermodynamic transition temperature where the reptation motion ceases completely. The index (i) indicates the particular growth regime, i.e. **I**, **II** or **III** as described in ref chapter I. The factor f is a correction coefficient for the temperature dependence of the enthalpy of fusion given as

$$f = \frac{2T_c}{(T_m^0 + T_c)} \qquad \text{(E.IV.4.3)}$$

The experimental linear growth rates were fit to the right hand of expression (E.IV.4.2) in the temperature range between 150°C and 190°C. It is noteworthy that prior

to the fit, the activation energy of reputation U^* was set to 2500 cal.mol^{-1} as proposed by *Hong* et al. [34]. For the equilibrium melting temperature the value of 272.5°C was used according to the non-linear determination performed by *Wu* and *Woo* [35], since the value of 245°C [34,36] is too close to the experimentally derived melting temperatures for this polymer. For T_∞, a value of $T_{\infty=} = T_g - 50°C$ was used.

The fit for crystallization regime **II** shown in Figure IV.4.4 properly reproduces the behavior at medium and high temperatures. However, some deviations can be found for temperatures below 140°C. The resulting activation energy K_{gII} equals 4.924 x 10^5 K^{2,} which is fitted in reasonable agreement to the literature data [31,34].

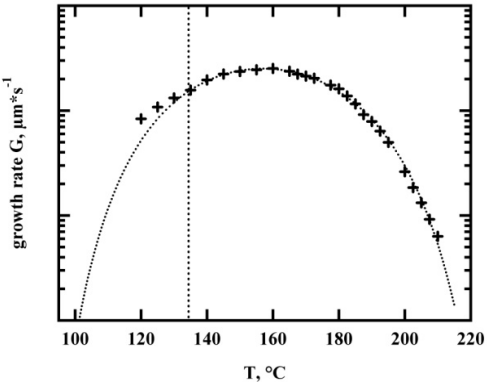

Figure IV.4.4**.** Linear growth rate of PTT as a function of crystallization temperature showing the classical bell-shaped curve. The fit of the data to the *Hoffman-Lauritzen* expression is shown in the dotted line. The maximum growth rate is reached at approximately 162°C.

Plotting the growth rates corrected for the mobility term as a function of $(T(\Delta T)f)^{-1}$ (cf. Figure IV.4.5) allows to examine the variation of $K_{g(i)}$, which is sensitive to the crystallization regime. It can be seen that the slope of the curve abruptly changes at about 135°C. The observed direction of the slope change indicates that there might be the growth regime transition **III** → **II**. The ratio of the corresponding values $K_{gIII}/K_{gII} = 2.017$ was derived, giving a value of 9.932 x 10^5 K^2 for K_{gIII}.

Importantly, this transition coincides with the onset of banding, as observed by optical microscopy and AFM. However, at singularity point $\mathbf{B_i}$ at around 180°C, where the band spacing becomes virtually infinite, no change of the growth regime can be detected. The

same holds for singularity $\mathbf{B_{sp}}$ at 202.5°C. This means that these two structural transitions are not correlated with the growth kinetics.

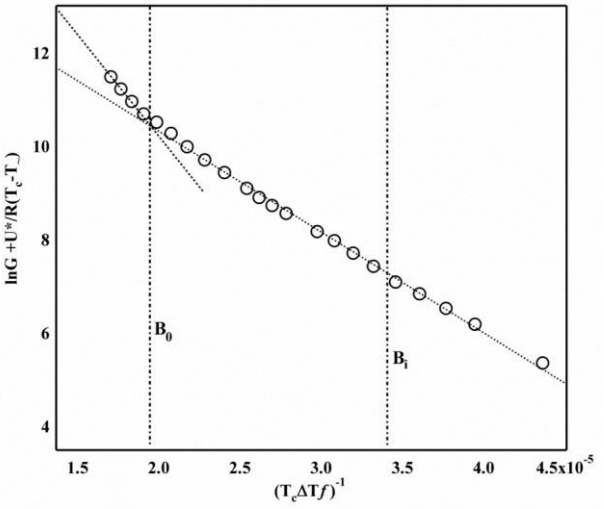

Figure IV.4.5**.** Hoffman-Lauritzen plot showing temperature dependence of the linear growth rate of PTT in the range between 130 and 210 °C.

Summarizing, it can be stated that the lamellar twisting does not occur in in the temperature range, which was tentatively assigned to crystallization regime **III**. This can be easily understood from the fact that, in this regime, the layer addition is mainly governed by nucleation. Thus, in the frame of the *KP*-model, this growth regime leads to only randomized and unorganized stress distribution on the lamellar surface, and is unable to generate synchronous lamellar twist.

IV.4.3 Spherulite microstructure formed at different crystallization temperatures

Averaged 2D X-ray diffraction patterns acquired on banded spherulites of PTT formed at three crystallization temperatures, which are chosen within temperature windows $\mathbf{B_I}$, $\mathbf{B_{II}}$ and $\mathbf{B_{III}}$ (Figure IV.4.2), are given in Figure IV.4.6.

The patterns are averaged over the full radial scans across the spherulites. In the integration, the central regions of the spherulites were skipped because within these regions the crystals are largely disoriented. The meridian of the patterns (vertical direction) corresponds to the crystal growth direction and thus to the crystallographic **a**-axis.

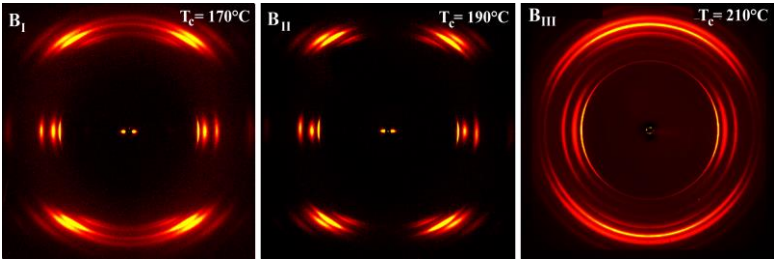

Figure IV.4.6**.** Averaged 2D X-ray diffraction patterns acquired on banded spherulites of PTT formed at the indicated crystallization temperatures. The radial direction of the spherulite is vertical. The patterns corresponding to the films crystallized within **BI** and **BII** temperature windows reveal pronounced crystal orientation while the latter is weak for the films crystallized within **BIII** temperature window.

In temperature regions $\mathbf{B_I}$ and $\mathbf{B_{II}}$, i.e. the left and middle panels of Figure IV.4.6, the azimuthal spread of the diffraction peaks is relatively small. By contrast, the peaks are significantly broadened for the pattern corresponding to temperature window $\mathbf{B_{III}}$. This change coincides with the change of the optical texture discussed previously.

IV.4.4 Inversion of the lamellar helicoid chirality

To clarify the nature of the first singularity point $\mathbf{B_i}$, a detailed analysis of the X-ray patterns was performed. Integrated 1D-diffractograms corresponding to two spherulites crystallized from the melt at 190°C are given in Figure IV.4.7. The diffracted intensity is plotted as a function of the distance from the spherulite center. The intensity and azimuthal position of the equatorial 010 reflection as a function of the radial distance from center allows determining the handedness of the lamellar helicoids using the *Ewald* sphere construction, as discussed in chapter III. It can be seen that for both spherulites the handedness of the lamellar helicoids is different in the spherulite sectors located above and below the spherulite center. Thus, the lamellar handedness is inversed when passing through the spherulite center. As explained in detail in chapter III, this is equivalent to the fact that the growth axis polarity changes its sign at the spherulite center. It is noteworthy that the 010 reflection stays strictly equatorial all along the radial micro-focus scan indicating that the direction of the **a**-axis is invariable in space. This unequivocally shows that the shape of the lamella is not helical but most likely approaches the classical helicoid, as was previously found for the lamellae formed at 170°C (cf. chapter III).

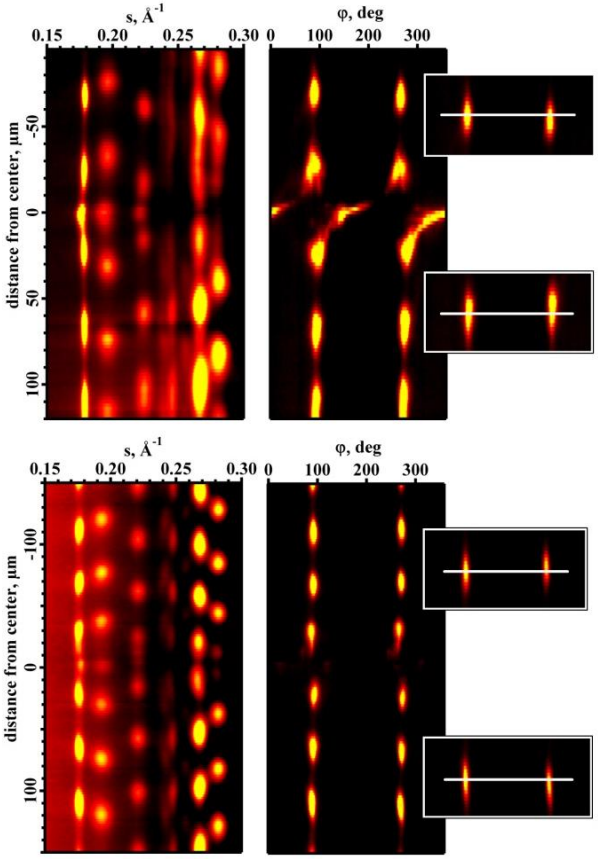

Figure IV.4.7. 2D representation of the integrated X-ray patterns recorded during radial micro-focus scans across two PTT spherulites (top and bottom panels) melt-crystallized at 190°C. The diffracted intensity is plotted as a function of distance from the spherulite center in the graphs of the **left column**. The **right column** gives the 010 peak intensity and azimuthal position as a function of the radial distance. The inserts give a closer view on the symmetric pair of 010 and 0-10 reflections showing that the lamellar handedness is different in the spherulite sectors above and below the spherulite center. Thus, in the sector above the spherulite center the lamellar helicoids are left-handed in the top panel and right-handed in the bottom panel, while below the spherulite center the situation is inversed for both spherulites (see text for more details).

To identify the correlation of the growth axis polarity and the lamella twist sense, a more detailed analysis of the 1D diffractograms has been carried out. The normalized intensities of selected equatorial reflections are given in Figure IV.4.8 as a function of the radial distance.

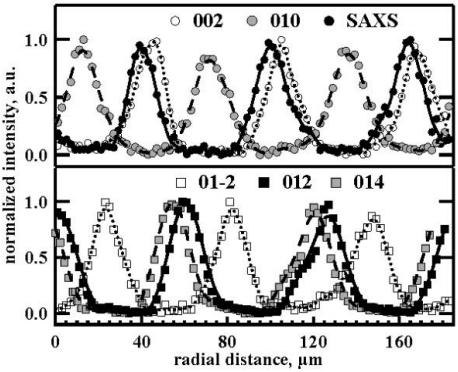

Figure IV.4.8. Integral intensities of several most intense equatorial reflections as a function of radial distance from the spherulite center.

The observed periodicity of the integral diffraction intensity as a function of radial distance shows that the lamellar twist is regular, as it was the case of melt-crystallization at 170°C. The power spectral density function (PSD) calculated from these curves reveals a characteristic spacing of 62.0 microns (cf. Figure IV.4.8), which is in good agreement with the band spacing evaluated from the optical micrographs (cf. Figure IV.4.9, left).

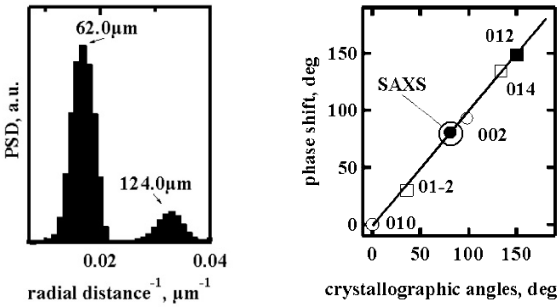

Figure IV.4.9. Power spectral density function calculated using the curves in Figure IV.4.8 reveals a characteristic twisting period of 62.0μm (**left**). Phase shifts of the different equatorial reflections with respect to the 010 peak as a function of the corresponding crystallographic angles of the reciprocal unit cell (**right**).

The phase shifts of the different diffraction peaks with regard to the 010 reflection are virtually identical to the crystallographic angles calculated for the PTT reciprocal unit cell (cf. Figure IV.4.9, right). Thus the lamellar twist is not only regular but also uniform. This conclusion is similar to the one drawn for the PTT films crystallized below $\mathbf{B_i}$.

However, now the order of appearance of the main equatorial peaks, i.e. (012) → (010) → (01-2), is opposite to the situation encountered at 170°C. Therefore the crystal rotation direction should be now inversed, as highlighted with the yellow arrow in Figure IV.4.10.

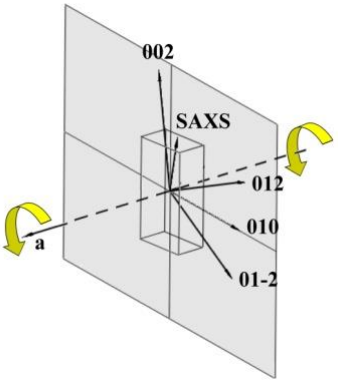

Figure IV.4.10. Crystallographic model of the lamellar twisting in a PTT film crystallized at 190°C. The rotation axis is parallel to the crystallographic **a**-axis. The vectors corresponding to the equatorial 0kl reflections rotate in the **b*c***-plane. The sense of the crystal rotation is indicated by the yellow arrows.

When looking along the positive **a**-axis, the sense of crystal rotation is right-handed for PTT crystallization within temperature window $\mathbf{B_{II}}$ (e.g., T_c=190°C). By contrast, it is left-handed for temperature window $\mathbf{B_I}$ (e.g., T_c=170°C) (cf. Figure III.3.7, right).

The comparative models showing the correlation of the crystal rotation with the handedness of the lamellar twist for the PTT melt-crystallization at 170 and 190°C are given in Figure IV.4.11. If the PTT film is crystallized above 178.5°C, i.e. in $\mathbf{B_{II}}$ temperature window, the lamella forms a right-handed helicoid when it grows in the **a**-direction, while it forms a left-handed helicoid when growing along the (**-a**)-direction.

To explore in some more detail the phenomenon of inversion of the lamellar chirality, additional studies have been performed on a PTT sample melt-crystallized at 180°C, i.e. very close to the singularity point. The radially-integrated diffractograms and integral intensity of the 010 reflection are given in Figure IV.4.12 (left). It is obvious that the exact temperature at which the lamellar twisting ceases would be almost impossible to catch, for the band spacing shows a diverging behavior in the vicinity of this temperature. This means that a very small variation in the setpoint temperature inevitably brings about a

large variation in the band spacing. At 180°C, slightly above critical temperature $\mathbf{B_i}$, only a weak change in the reflection intensity can be observed when scanning across the entire spherulite radius. In the acquired diffractograms not all usual reflections are visible showing that at this temperature, when the crystals are growing as almost planar ribbons, their single crystal texture is preserved.

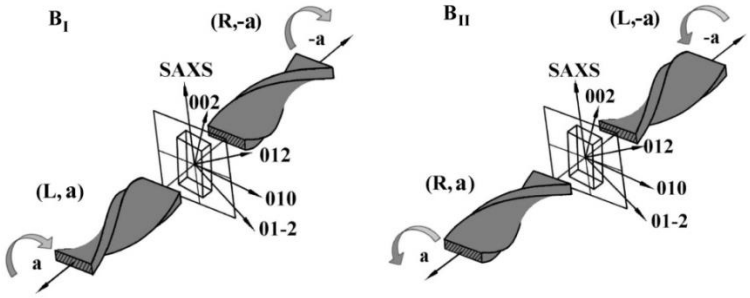

Figure IV.4.11. Sketches of the lamellar twist for the PTT samples melt-crystallized at 170 and 190°C, **left** and **right** respectively. The axis of rotation corresponds to the crystallographic **a**-axis, the 0kl reflections rotate around **a** in a plane perpendicular to it. The gray arrows indicate the rotation of the unit cell during linear growth in the direction indicated with thin black arrows.

Due to the quasi-planarity of the lamellae, it is difficult to identify the lamella handedness as it was done previously. Indeed, in this case not even a quarter of a full turn is observable when scanning along the lamellae for over more than 100 microns in each direction. However, the sequence of the main equatorial reflections in their appearance, i.e. (012) → (010) → (01-2), corresponds to the case of B_{II} temperature region. The structural model for this case is given in Figure IV.4.12 (right).

The observed correlation between the growth axis polarity (i.e., **a** versus **-a**) and handedness of the lamellar helicoid (*L* versus *R*) can be expressed in terms of the chirality parameter pairs. Thus, for temperature region $\mathbf{B_I}$, the PTT structure exhibits only the lamellar helicoids characterized by (*L*, **a**) and (*R*,**-a**), while in temperature region $\mathbf{B_{II}}$ the structure is composed of lamellae (*L*,**-a**) and (*R*, **a**). From this writing, it is evident that, when passing across the singularity point $\mathbf{B_i}$, one and only one of the two chiral parameters is necessarily inversed. Therefore, none of the parameter pairs can exist simultaneously in temperature regions $\mathbf{B_I}$ and $\mathbf{B_{II}}$. Apart from the chirality inversion, it is important to note that, in each temperature region, only two structural states out of the totally four are realized. The two discussed parameters can thus be viewed as a necessary and sufficient

basis of independent chirality parameters fully expressing the structural state of the lamellar helicoids at the spatial scales addressed in this work. The physical meaning of this chirality basis will be discussed in some more detail further in the text.

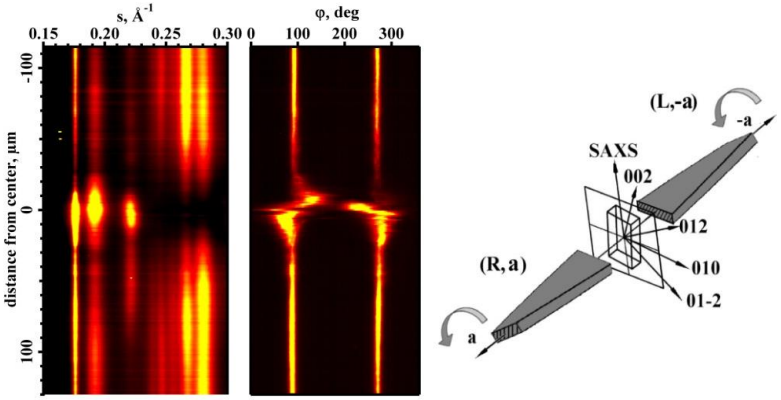

Figure IV.4.12. (**Left**) 2D representation of the integrated X-ray patterns acquired during a radial micro-focus scan across a PTT spherulite melt-crystallized at 180°C. The intensities are plotted as a function of distance from the spherulite center. (**Middle**) Intensity and azimuthal position of the 010 respectively to **Left**. The graph does not allow determining the handedness of the lamellar twist due to its very large band spacing. (**Right**) Sketch of the lamellar twist based on the data of the left and middle panels (cf. caption to Figure IV.4.11).

At this point, it is appropriate to revisit the band spacing dependence on crystallization temperature (cf. Figure IV.4.13, top). In consideration of this curve, one can ascribe a sign to the value of the band spacing, depending on the chirality of the objects. This is similar to what was suggested in the past for the cholesteric liquid crystals by *Samulski* and *Samulski* [21]. Using the obtained information on chirality of the lamellar helicoids, one can accordingly redraw the curve, for example as shown in Figure IV.4.13 (middle). In this case, the band spacing in the $\mathbf{B_{II}}$ region is represented in negative values. This modified representation of the structural data allows appreciating the chiral or non-chiral nature of the different transitions such as $\mathbf{B_i}$ and $\mathbf{B_{sp}}$. Also, since the band spacing diverges at $\mathbf{B_i}$, it is convenient to plot the reciprocal of this value (Figure IV.4.13, bottom), as it is common practice in the field of liquid crystals. Here the curve passes through zero at $\mathbf{B_i}$ exhibiting a rather smooth and continuous variation. By contrast, the transition at point $\mathbf{B_{sp}}$ shows a markedly different behavior, characterized by a stepwise variation.

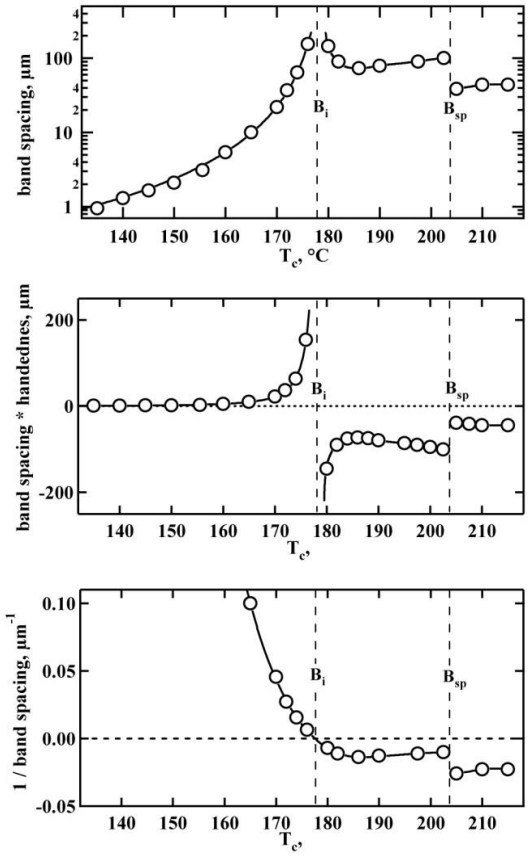

Figure IV.4.13**.** band spacing of isothermally melt-crystallized PTT spherulites as a function of crystallization temperature plotted in semi-logarithmic coordinates showing the structural transitions at **Bi** and **Bsp** (**top**). The same graph as in the top panel but taken with the sign reflecting the chirality of the lamellar helicoids (**middle**). Reciprocal signed band spacing as a function of crystallization temperature (**bottom**).

IV.4.5 Chain tilt versus lamellar twisting sense

In the seminal model of *Keith* and *Padden* accounting for the lamellar twisting [4], the origin of the unbalanced stresses on the lamellar surface was assumed to be the tilt of the crystalline stems with respect to the lamella normal. The direction of this tilt, which would be mainly responsible for the appearance of the stresses, was however not specified in

their work, to our knowledge. Unfortunately, the interpretation of the chain tilt may be different if one alludes to the lamellar crystals of PE or to those of any other crystallizable polymer.

The source of the ambiguity here is due to the fact that, in the classical literature, the authors were often used to extrapolate the single-crystal morphology of PE resulting from solution crystallization to the case of a melt-crystallized PE morphology exhibiting spherulites. Within the frame of such arbitrary and, to our opinion, sometimes unjustified analogy, one may infer that the schematic picture of *Keith* and *Padden* depicts the (110) growth faces of a single-crystal-like species converging at an apex corresponding to the **b**-direction of the PE unit cell (cf. Figure IV.4.14). It is appropriate to recall here that the **b**-axis is the fastest growth direction of PE in the bulk (but not in solution). Then one could think that the chain tilt dwelled upon in the work of *Keith* and *Padden* is not only the tilt of the stems in the plane perpendicular to the lamellar growth direction but also in the plane parallel to it.

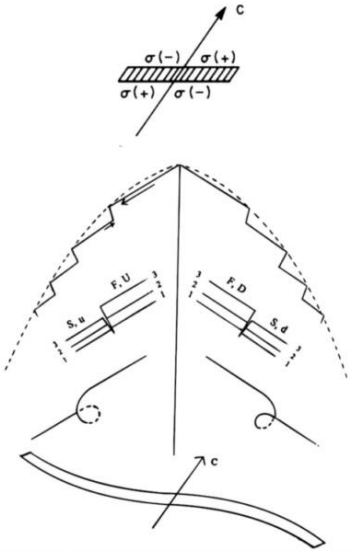

Figure IV.4.14. Flat lamellar crystal with canted chains according to the *KP*-model reprinted from [4] (**top**). Schematic representation of a symmetrical S-shaped polyethylene lamellar crystal in which chain tilt would result in a right-handed twist (**bottom**). Spreading layers produce re-entrant corners around which "shears" and subsequent overlapping growth generate embryonic giant screw dislocations as shown. It is worth to note that in this case dislocations so initiated would be right-handed on either side of the lamella reprinted from [22].

Whatever the exact meaning of the chain tilt referred to by *Keith* and *Padden* might be, their particular arguments used to link it to the picture of the surface stresses distribution were heavily criticized in the literature for their empiric character [23]. To our opinion, there could hardly be any trivial relationship between the lamellar micro-structure and distribution of stresses generated during crystallization at the crystal/amorphous interface.This rather pessimistic assumption is however in line with recent off-lattice simulations performed by *Rutledge* and co-authors [24-26].

By contrast, it is trivial that the tilt provides an additional chirality parameter to the lamellar crystal. Thus it is easy to grasp that, even for the case of a flat lamella, the chain tilt renders the object chiral given that the growth axis is a vector. Importantly, for the case of PTT only the chain tilt in the plane perpendicular to the growth axis renders the lamella chiral because the “up” and “down” chains of PTT cannot be distinguished. Although the chain tilt is an obviously chiral parameter, this fact was never discussed in the literature, to our knowledge.

The system studied in the present work, provides an excellent means to check the premises of the *Keith* and *Padden* model by correlating the observed chirality of the lamellar helicoids to the observed chain tilt. In order to do so, the orientation of the unit cell was identified for the PTT films crystallized in the temperature range from 170 to 200°C. The chain tilt was calculated using the radial offset of the equatorial reflections with regard to the main interference maximum in the SAXS region normalized by the twist period. The resulting values of the chain tilt with respect to **b***, i.e. in the plane perpendicular to the fast growth axis, are given in Figure IV.4.15 as a function of crystallization temperature.

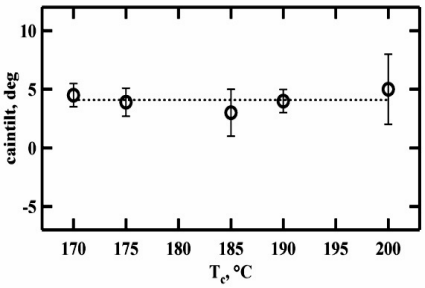

Figure IV.4.15. Chain tilt with respect to the lamella normal as a function of crystallization temperature. The graph shows no significant variation of the chain tilt across inversion point **Bi** and also in a broader temperature range.

It appears that the chain tilt is independent of crystallization temperature, being equal to ca. 4.0 deg with standard deviation of less than 2.0 deg. This means that the crystalline stems stay almost vertical in the lamellar crystal. Furthermore, the chain tilt does not appreciably change its value or switch its direction across chirality inversion point $\mathbf{B_i}$ (cf. Figure III.3.7, right, and Figure IV.4.10). Therefore one can conclude that, upon scrutiny, the premise of the *Keith* and *Padden* model linking the helicoids handedness with the chain tilt direction have not found experimental support for PTT.

It is appropriate to recall that the crystalline stem conformation of PE, which *Keith* and *Padden* mainly refer to in their works, is strongly different from that of PTT. First, in the case of PE the chain forms a planar *zig-zag* while the PTT chain adopts a complex conformation where successive monomers form parts of alternating right- and left-handed helices. Thus, globally the PTT chain does not exhibit chirality, and can be assimilated to a *zig-zag* conformation in both the **ac** and **bc** projections. Second, the crystalline stems of PE and PTT remarkably differ in their dimensions. Thus, the **c**-parameter of the PTT unit cell is more than seven times larger than that of PE while the typical crystal thickness of PTT is about four times smaller. Thus, in PE lamella many tens of *zig-zags* are present in one crystalline stem while this number is less than three for any melt-crystallized PTT. Therefore, considered statistically, the local inclination of a single segment in the PE lamellae won't play any role, while for PTT each segment of its *zig-zag* corresponds to more than 20% of crystalline stem length. From such a simple observation it follows that, even if the crystal thickness variation across the PTT sample is on the order of 10% [28], the segments of the crystalline stems protruding the lamella surface are still kept the same. Taking these facts into account, one can draw a molecular model explaining the origin of the chiral twist in the PTT lamellae. In this model, it will be logical to assume that the key parameter determining the surface stresses is the angle of the crystalline stem segment protruding the lamella surface rather than the overall chain tilt, as it was proposed previously for the case of PE.

IV.4.6 Lamellar twisting versus lamellar thickness

According to the above discussion, if one supposes that the unbalanced stresses on the lamella surface are correlated to the angle of the surface-protruding segment, one should be able to observe their variation with crystal thickness and, consequently, with crystallization temperature. To appreciate this effect, SAXS experiments on bulk samples

of melt-crystallized PTT have been conducted. The SAXS curves are given in Figure IV.4.16 (left). They exhibit the main interference maximum corresponding to the long period L_B slightly below 0.01Å^{-1}, which moves to smaller angles with increasing the crystallization temperature. These results are similar to the ones described by *Ivanov* and co-authors [27, 28].

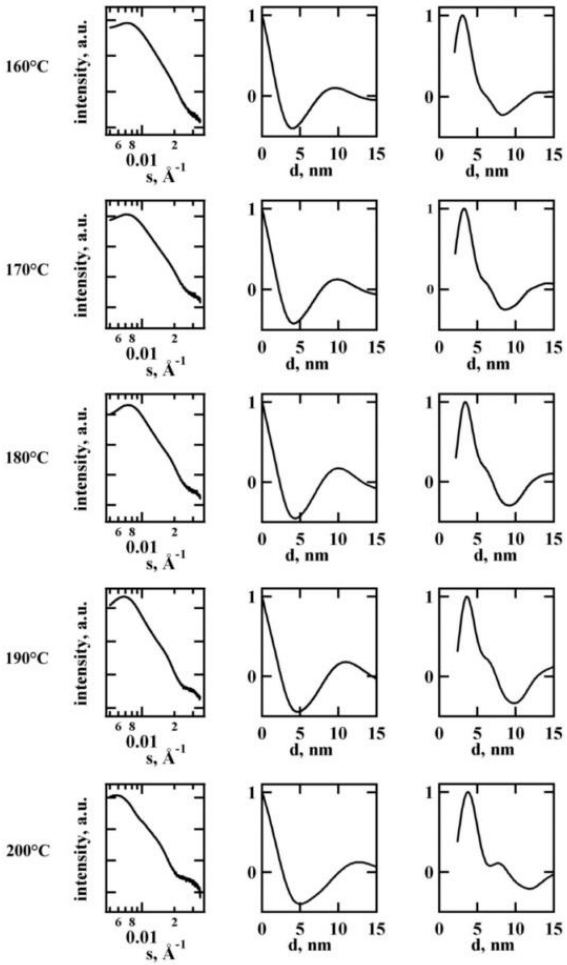

Figure IV.4.16. Experimental SAXS curves (**left column**), CF and IDF functions (**middle** and **right columns**, respectively) corresponding to bulk samples of PTT isothermally melt-crystallized at indicated temperatures.

The second feature of the SAXS curves visible as a weak shoulder appears at approximately 0.02 $Å^{-1}$. As discussed elsewhere [27,28] it corresponds to the form-factor of the PTT crystals, which are rather monodisperse in thickness. The form-factor becomes more pronounced with increasing crystallization temperatures while moving to smaller angles. The normalized correlation functions (CF) calculated as a real part of the Fourier-transform of the corrected scattering intensity [cf. chapter II] are given in Figure IV.4.16 (middle). The interface distribution functions (IDF) computed as a second derivative of the correlation functions are given in the right column of Figure IV.4.16. All IDFs exhibit either two positive maxima or one maximum and one shoulder close to the origin, which correspond to crystal thickness L_c and amorphous layer thickness L_a. The first negative maximum of the functions corresponds to long period L_B.

The crystal thicknesses values derived from the IDFs are plotted in Figure IV.4.17 as a function of crystallization temperature. They show an increment of about 20% in the temperature range from 160 to 200°C while an additional increment of 10% occurs in the range from 200 to 210°C.

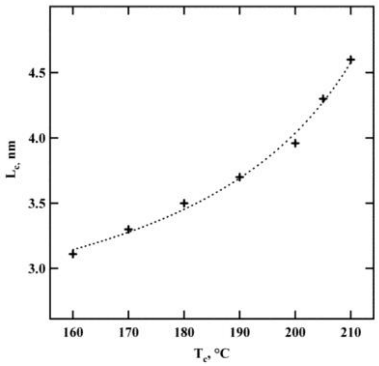

Figure IV.4.17. Lamellar thickness L_c as a function of crystallization temperature shows an increase by about 1.0 nm (or by ca. 20%) in the temperature range from 160 to 200°C. The dashed line is a guide for the eye.

At this point, it is interesting to check whether the experimentally derived correlation of the twisting period to the lamellar thickness is in agreement with the correlations proposed in the literature. In the frame of a simple mechanical model accounting for the energy of torsion [29], the lamellar twist period P can be described as a function of the

lamellar thickness l_c, elastic modulus G and the excess of the surface tension due to the inherent stress γ_e according to

$$P = \frac{\pi}{6}\left(\frac{G}{\gamma_e \delta}\right) l_c^2 \qquad \text{(E.IV.4.4)}$$

In equation (E.IV.4.4), δ stands for the thickness of the surface region in which the stress is acting. Assuming that δ is not a rapid function of crystallization temperature, one can visualize the dependence of γ_e on the lamellar thickness (cf. Figure IV.4.18). It can be seen that γ_e rapidly decays in the range of l_c-values comprised between 3.1 and 3.5 nm. Above this range, the stresses become negative but do not evolve much in terms of their absolute values. This result shows that, in modeling the twisting behavior of lamellar crystals, one cannot simply assume that the stress is a slowly changing function of the lamellar thickness, as it was done in [30].

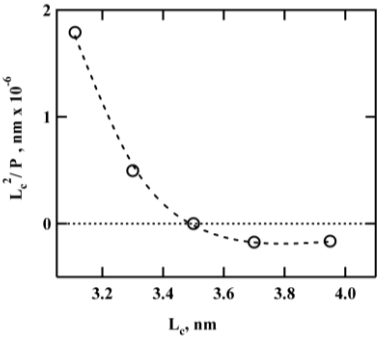

Figure IV.4.18. Reciprocal band spacing normalized by l_c^2 plotted as a function of the lamellar thickness.

It is also instructive to check whether the mechanism of the axial screw dislocation generation could be at the origin of the lamellar twisting in PTT, as it is the case of *Eshelby's* twist [31]. In this model, the sequential creation of screw dislocations of the same handedness evolves as macroscopic lamellar twist.If the dislocations are created by thermal fluctuations, the ring period, P, will be determined by the creation probability which is exponentially dependent on the strain energy in proportion to l_c^3. Then, the dependence of P on l_c will be given as [32]

$$P \propto \exp\left(\frac{C_{dis} l_c^3}{k_b T}\right) \quad \text{(E.IV.4.5)}$$

where C_{dis} denotes a coefficient proportional to the creation energy of the dislocation. The C_{dis} can be described as

$$C_{dis} = \frac{K}{4\pi} \ln\left(\frac{R}{r_0}\right) \quad \text{(E.IV.4.6)}$$

In equation (E.IV.4.6), the constant K is determined from the elastic modulus of the crystal. The R and r_0 represent the size of the area undergoing the elastic deformation and that of dislocation core, respectively. From even a superficial analysis of equation (E.IV.4.5), it is clear that this mechanism will never be able to explain a non-monotonic variation of P on l_c, such as observed for PTT. Therefore it can be disconsidered in the present work.

IV.4.7 Molecular-scale model of the lamellar twisting

To rationalize the observed twisting behavior of the PTT crystals, one can firstly consider the structure of the chain, which contains rigid terephthalic units alternating with flexible propyl units, as depicted in Figure IV.4.19. The rigid parts of the chain form straight segments as emphasized by the yellow ellipses. The soft segments including the semi-flexible ester bonds form alternating right- and left-handed helical sequences highlighted by the light-blue clouds.

If one neglects the small tilt of the chain stems derived above, the projection of one soft segment onto the **c** axis is estimated at ca. 24% of the **c**-parameter, while the hard segment covers the rest of the half of **c**-parameter, i.e., 26%. Taking into account the fact that one unit cell contains two hard and two soft segments, the crystal thickness variation observed between 160 and 202.5°C is comprised within the length of two flexible segments. One can speculate that the segments emanating from the crystal surface into the interlamellar amorphous region must be soft because they allow dissipating order more efficiently than the rigid segments.

Generally, it seems rather improbable that the same rigid segment can be shared by the crystal and adjacent disordered amorphous phase because the rigid segment will keep

the atoms in crystallographic register all the way through its length. Therefore it cannot dissipate order that efficiently and cannot create a sharp crystal-amorphous interface, as observed in SAXS. An idealized molecular model based on the above considerations is given in Figure IV.4.20 for crystallization temperatures comprised within $\mathbf{B_I}$ and $\mathbf{B_{II}}$ zones.

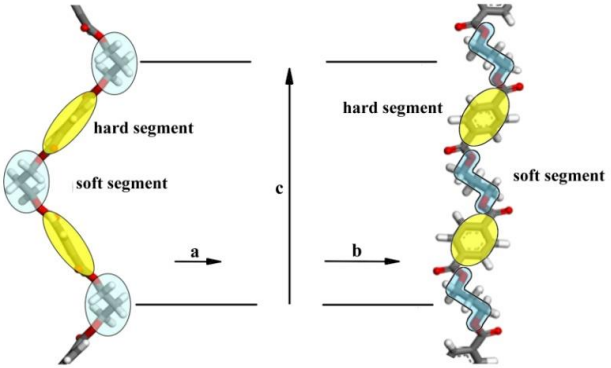

Figure IV.4.19**.** Cartoon depicting the chemical structure of PTT chain composed of rigid and soft sequences shown in projection on the **ac** (**left**) and **bc** plane (**right**).

One can notice that, when looking opposite to the growth direction **a,** the rigid segments are all inclined to the right. The middle part of the soft segment is tilted to the left, while the two parts of it which are closer to the neighboring hard segments, are both tilted to the right as it is the case for the rigid segment.

If one considers now a particular case of the PTT melt-crystallization at 170°C, the corresponding crystal thickness is about 33Å, i.e. ca. 1.75**.c**. Assuming a symmetrical situation at both basal planes of the lamella, the soft segments will be cut by the basal planes in their first parts (cf. Figure IV.4.20, left). According to the arguments of the *KP*-model, such inclination of the terminal segments should result in a left-handed twist when growing along the positive **a-**direction. This is indeed what is observed for PTT.

For the case of the PTT melt-crystallization at 190°C (cf. Figure IV.4.20, right), the crystal thickness reaches 37 Å. The basal planes of the lamella will now intersect the soft segments in their middle parts, resulting in the inversion of the tilt angles of the terminal lamellar segments and inversion of the expected lamellar twist. This is again in agreement with what is observed for PTT.

To understand what happens at the $\mathbf{B_{sp}}$ structural transition, the molecular models have to be viewed also in the projection parallel to the fast growth axis (cf. Figure IV.4.21). The molecular arrangement with respect to the crystal surfaces is given for the three temperature regions, i.e. $\mathbf{B_I}$, $\mathbf{B_{II}}$ and $\mathbf{B_{III}}$, in Figure IV.4.21 (left, middle and right) when viewed along the growth direction (top) and perpendicular to it (middle).

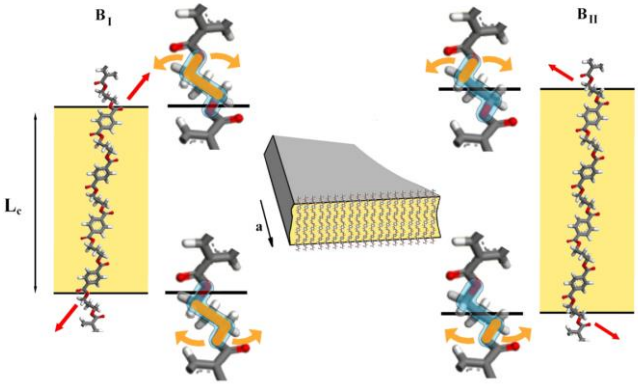

Figure IV.4.20**.** Cartoon depicting an idealized molecular model of the PTT lamellae formed in B_I and B_{II} temperature regions, e.g. at 170 and 190°C. It can be noticed that, at inversion temperature B_i, there is a significant change in the orientation of the molecular segments protruding the lamellar surface. The part of the sort segment protruding the crystal surface, which is in the amorphous phase, is indicated in orange. The conformational lability of the flexible segment is given by the orange arrows.

When the crystal thickness continuously increases above the $\mathbf{B_i}$ singularity point, the lamellar surface shifts more and more close to the next hard segment, the situation, which is presumably unfavorable for the lamella. At a certain thickness, the crystal copes for this problem by re-arranging in such a way that one more rigid segment is incorporated in the crystal while exposing the main parts of the flexible segments on both fold surfaces. To achieve this, the crystal has only two possibilities, namely, to incorporate the hard segment from the above or below the crystal. Both cases are identical from the point of view of the segment inclination projected on the growth face (cf. Figure IV.4.21, top right). However, they are not identical along the inclination direction, i.e., as seen from the side (cf. Figure IV.4.21, top bottom).

This change of molecular arrangement should happen at a particular temperature and should have the nature of a sharp structural transition, or “singularity”. It is expected that the micro-structure below and above this particular temperature significantly differ from

each other leading to an abrupt change in the surface stress distribution reflected in a jump of the band spacing. From the optical microscopy data, this rearrangement was identified to occur between 202.5 and 205°C (cf. Figure IV.4.1, bottom line). The coexistence of both types of lamellae having different surface stresses in the growth axis direction can lead to a disturbance in the lamellar packing, or to what we term here as "unlocking transition". We suppose that such lamellae cannot efficiently pack in stacks and therefore "unlock", which is clearly visible from the loss of the radial crystal orientation (cf. Figure IV.4.6, right). The micro-structure of the lamellar helicoids in this temperature region is described in more detail in the following.

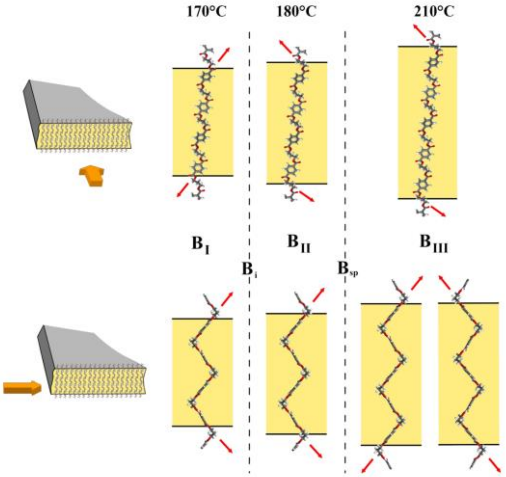

Figure IV.4.21. Cartoon depicting an idealized molecular model of the PTT lamellae below and above inversion temperature **Bi** and the unlocking temperature **Bsp**. Projections parallel (**top**) and perpendicular to (**bottom**) the crystal growth direction.

The 2D plots of the integrated 1D-diffractograms corresponding to PTT spherulites crystallized from the melt at 210 and 215°C are given in the top and bottom panels of Figure IV.4.22, respectively.

For the sample crystallized at 210°C, the diffraction intensity oscillations are still visible showing that the banding behavior persists at this temperature. Here, the band spacing drops down to about 30 microns, while the order of appearance of the main equatorial reflections indicates a clockwise rotation of the crystal while looking along a, as it is the case in temperature region $\mathbf{B_{II}}$.

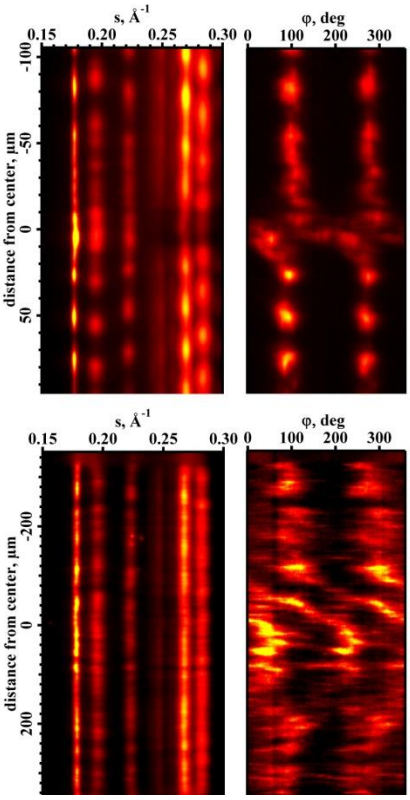

Figure IV.4.22**.** 2D plots of the integrated 1D-diffractograms corresponding to PTT spherulites crystallized at 210 (**top**) and 215°C (**bottom**). The diffracted intensity is plotted as a function of distance from the spherulite center. Peak intensity and azimuthal position of the equatorial 010 reflection as a function of the radial distance from the spherulite center does not allow determining t he handedness of the lamellae due to irregular twisting.

The azimuthal breadth of the 010 reflection is very large when compared to the patterns recorded for lower crystallization temperatures presumably due to the "unlocked" lamella growth described above. Also the diffraction peak appearance makes it impossible to identify the handedness of the twist using the *Ewald* sphere construction. These findings are in agreement with the molecular model proposed above.However, with further increasing the crystallization temperature the lamellar rotation becomes more and more irregular, while the radial orientation of the lamellar stacks worsens. For PTT crystallized at 215°C (Figure IV.4.22, bottom) no regular banding is visible anymore, and the diffractograms show an almost random variation of the refection intensity.

IV.4.8 Hierarchical levels of the lamella chirality

The correlation of the molecular chirality to that of the corresponding supermolecular structures, e.g. twisted lamellae, is extensively discussed in the literature [6]. However, there is still not much about how exactly the chiral molecules can build superstructures characterized by chirality on a much larger spatial scale. This discussion leads us to the question on how the different spatial levels of chirality interact with each other in the process of self-assembly. For an non-chiral semicrystalline polymer such as PTT, the different chirality levels are schematically depicted in Figure IV.4.23.

It is clear that, even intrinsically non-chiral molecules, are able to form chiral aggregates for example in the process of crystallization. Thus, the conformation of macromolecules in the crystalline state is generally helical, i.e. undoubtedly chiral [33]. A few exceptions might be considered here, including degenerated helices, as in the case of PE, which do not possess the conformational chirality upon crystallization. The next spatial level where the supramolecular chirality is present is the unit cell structure. Generally, all 3D unit cells are chiral by the very definition of their basis of direct-space vectors. However it is not always possible to separate the chirality of the crystalline conformation of an individual chain from that of the crystalline lattice formed by the same chain. Obviously, it can be done so only to the extent that the symmetry operations imposed on the repeating motif by the symmetry group of the crystal result in chirality, the spatial scale of which goes beyond that of a single chain. For the case of PTT, a triclinic unit cell with symmetry group P-1 implies for example that the chirality of (100) and (-100) faces of the unit cell is opposite for there is an inversion center. To understand what this actually means, and what are the chiral elements pertinent to the crystalline lattice, one has to look in detail on the unit cell structure. For the particular case of PTT, the elements inversing their chirality on the (100) versus (-100) crystal faces are the soft segments of the chain, to which alternating handedness can be assigned, as mentioned previously. Therefore, in this work, we have selected the growth axis polarity (i.e., **a** or (-**a**)) as one of the two independent chirality parameters of the PTT twisted lamellae.

Till now, the chirality of the supramolecular aggregates was considered at the scale of an Angström-nanometer. The next level of chirality, as far as we can identify it for the twisted lamellae, is due to a well-defined orientation of the unit cell within the lamellar ribbon, e.g. due to the tilt of the crystalline stems. Since the “up”- and “down”-chains of PTT cannot be distinguished (which is in contrast for example to the chains of

poly(vinylidene fluoride)), only the chain tilt in the plane perpendicular to the growth axis renders the PTT lamellae chiral. Finally, the highest spatial level of chirality of the twisted lamellae corresponds to the handedness of the lamellar ribbon (i.e., *R* or *L*). The spatial scale on which this chiral parameter operates exceeds hundreds of microns.

Interestingly, according to the results presented in this chapter, the chain tilt in the PTT lamellae is virtually invariant with crystallization temperature. Therefore the chain tilt value, as well as its direction, seems to be decoupled from the two other chiral parameters, which change their sign when passing across inversion point $\mathbf{B_i}$. We can thus state that the nature does not make use the chain-tilt-induced chirality to control the micro-structure of the twisted PTT lamellae.

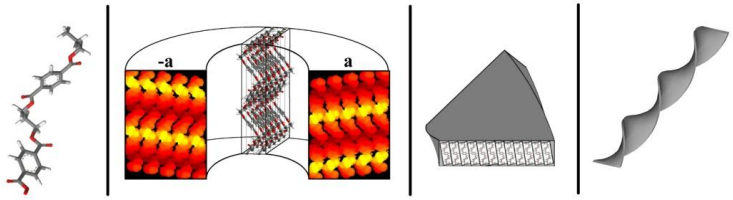

Figure IV.4.23. Cartoon depicting four different spatial levels of chirality of an intrinsically non-chiral polymer. (**Left** to **right**): chirality of the chain conformation in the crystalline state; chirality of the unit cell structure exemplified for the case of (-100) and (100) crystallographic planes of the PTT lattice; tilted molecular orientation in the lamella and, finally, the chiralitiy of the twisted lamella.

After exclusion of this parameter from consideration, we are left with only two chiral parameters, namely the growth axis polarity and handedness of the helicoid, because the chiral conformation of the chain in the unit cell is not subject to variation. At the present state, we can only guess about the exact physical interaction between the growth axis polarity and handedness of the PTT lamella. It would be thus of great interest to analyze other cases of banded spherulites formed by polymers for which the inversion center is not present in the unit cell. These examples could be triclinic lattices with P1 symmetry as well as monoclinic lattices that exhibit “monoclinicity” in the plane perpendicular to the growth direction, i.e. for example unit cells with angle α different from 90 deg if the fast growth axis is **a**. For all other cases, comprising unit cells with orthorhombic symmetry and higher, the determination of the growth axis polarity by crystallographic means becomes impossible.

IV.4.9 Structural memory transferred during spherulitic growth

Homogeneous and regular packing of twisted lamellar ribbons forming a spherulite is in clear conflict with the overall spherical symmetry of these objects. Since the size of the crystal superstructures such as lamellar stacks does not drastically change with radial distance, the so-called in-filling growth is required whereby the regions in-between the diverging lamellar stacks growing radially outward are continuously filled with newly-formed lamellae. In the classical view of the polymer spherulite, this in-filling growth is believed to happen through a non-crystallographic small-angle branching of the lamellae [34].

A sketch of this micro-structure is depicted in Figure IV.4.24 for a spherulite where the spherical symmetry is achieved only at some distance away from the spherulite center via continuous branching of the initial sheaf-like lamellar stack. The insufficient branching frequency leads to formation of the well-documented spherulitic eyes where the crystal orientation strongly departs from radial.

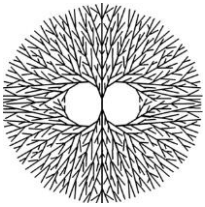

Figure IV.4.24. Classical model of the non-crystallographic lamellar branching occurring during spherulitic crystallization.

In the classical textbooks on solid-state polymer physics [34] it is believed that the local-scale texture of “normal” spherulites exhibits a fiber-like texture, i.e. all crystal orientations around the fast growth axis are equally probable. In this case, the structural information that one can hope to extract from micro-focus X-ray diffraction will be mainly limited to determination of the fast growth axis, which is not enough for debating on the exact lamella branching mechanisms. By contrast, the banded PTT spherulites do provide an appropriate object on which these long-standing issues can be tackled. We allude here to the fact that, at the local scale, the banded spherulites of PTT reveal a single-crystal-like texture, which is by far more informative for the X-ray structural analysis. Thus, we have previously seen that, in addition to determination of the fast growth axis, we were able to assess two chiral parameters of the twisted lamellae, i.e. the growth axis polarity and

lamella handedness. We have also seen that these parameters were unambiguously determined and invariable for each radial stack of lamellar helicoids. Using this information, one can address the lamella branching mechanisms to such detail, which was inaccessible in the past, to our knowledge.

To explore what is exactly the structural information that the lamellar crystals transfer with them, from the very beginning of their growth from a heterogeneous nucleus to the utmost lamellar tip, at the front with the quiescent melt, we designed an experiment in which the isothermal crystallization temperature was changed during the spherulite growth in a stepwise manner. In particular, we prepared temperature programs where the setpoint temperature passed through the $\mathbf{B_i}$ inversion point. As we have seen, the chirality of the lamella helicoids is inversed past this point, i.e. one and only one of the two chiral parameters has to be changed. The scientific question that we would like to address here is "which one of the two chiral parameters will be inversed for an individual lamellar stack during growth past the inversion point".

The polarized optical micrographs corresponding to spherulites melt-crystallized at 170°C-step-190°C and 190°C-step-170°C are given in the bottom left and bottom right panels of Figure IV.4.25, respectively.

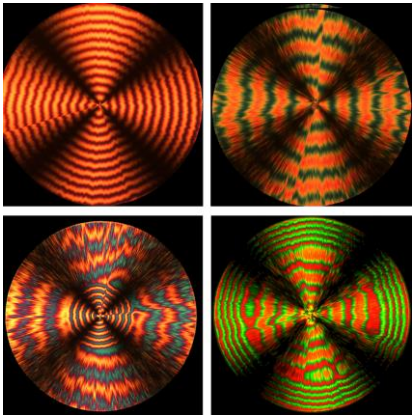

Figure IV.4.25**.** Polarized optical micrographs of the PTT film isothermally crystallized at 170 (**top left**) and 190°C (**top right**). and step crystallized (**bottom**) at first 170°C jump to 190°C (**left**) and vice versa (**right**) showing a jump like change of the banded morphology.

The spherulites isothermally crystallized at 170 and 190°C are given in the top panels of the same figure for the sake of comparison. For the spherulites grown past the inversion

point, the step in the temperature program corresponds to an abrupt change in the band spacing. Thus, the employed temperature programs did not impede the lamellar twisting after the passage across the inversion transition. Radial scans across the spherulites formed according to the temperature programs described above were performed using micro-focus X-ray scattering. The corresponding 2D plots of the integrated 1D-diffractograms are given in Figure IV.4.26 as a function of radial distance from the spherulite center.

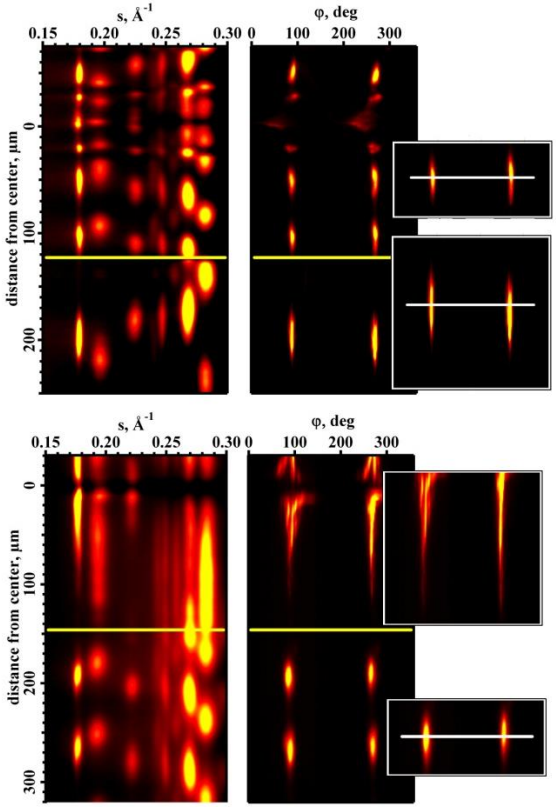

Figure IV.4.26. 2D representation of the 1D-diffractograms corresponding to PTT spherulites crystallized from the melt at 170°C-step-190°C (**top**) and at 190°C-step-170°C (**bottom**). The radial position corresponding to the temperature jump is indicated by the yellow line. The diffracted intensity is plotted as a function of distance from the spherulite center. The intensity and azimuthal position of the equatorial 010 reflection as a function of the distance from the spherulite center allow determining the handedness of the lamellar twist. The sequence of appearance of the equatorial reflections is inversed across the inversion transition. For both spherulites, the inversion transition corresponds to inversion of lamellar handedness.

For the case where the initial crystallization temperature is 170°C, the sequence of appearance of the equatorial peaks (cf. Figure IV.4.26, top) exactly matches our findings reported in the previous chapter. Moreover, the lamellar stack reveals a right-handed twist identified with the *Ewald* sphere construction. At the point of the temperature step, the crystal rotation direction is inversed, as seen from the inversion of the reflection sequence. This transition brings about the inversion of the lamellar handedness. Qualitatively the same conclusion can be drawn from the scan of the 190°C-step-170°C sample. Here the reflection sequence changes from the counter-clockwise to clockwise rotation when looking along (**-a**), while the handedness of the lamellar twist changes from left to right.

The vector models corresponding to the two cases are given in Figure IV.4.27. It can be seen that for both spherulites the growth axis polarity stays invariant throughout the whole crystallization, thereby keeping the growth axis direction parallel to (**-a**).

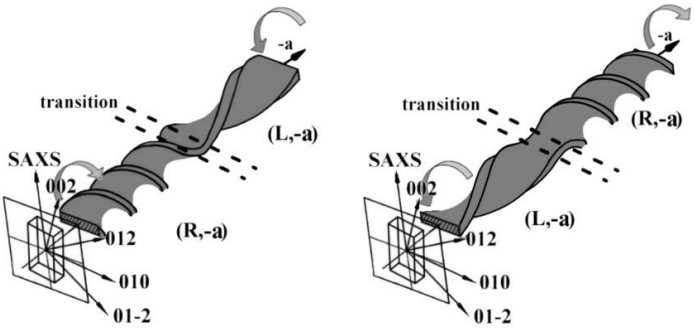

Figure IV.4.27**.** Vector models depicting the rotating unit cell for the step-crystallized films. The axis of rotation corresponds to the crystallographic **a**-axis, all 0kl reflections rotate around **a** in the plane perpendicular to it. The gray arrows indicate the rotation direction of the unit cell. The sense of the lamellar twist is inversed at the inversion temperature **Bi**, while the growth axis polarity is kept invariable.

From the described experiments, it follows that if there is any structural memory that the lamellar crystal could transfer during spherulitic growth, it is the growth axis polarity rather than the lamellar handedness. As far as the classical hypothesis of the non-crystallographic branching is concerned, it seems very unlikely that the growth axis polarity could be preserved through such an ill-identified process. Thus, one has to admit that in the case of PTT no such thing as “non-crystallographic” branching exists. Moreover, if one were able to imagine such “non-crystallographic” reproduction of the lamellae, it would probably keep invariable the lamellar handedness, as the newly-formed

lamella inserts would have to copy the handedness of their parent crystal in order not to crash on it after a fraction of a turn. There could be thus no solid arguments in favor of the inversion of the lamellar handedness. Instead, if from the very beginning one admits that the lamella branching occurs strictly according to crystallographic register, it becomes clear that the growth axis polarity could never be inversed. As we have seen previously, PTT crystallizes according to a triclinic symmetry and therefore the growth face should make an angle with the fast growth direction, which is not right but close to the crystallographic angle γ, which is 111 deg. A selected high-temperature AFM micrograph measured during growth of a PTT spherulite shows indeed an inclination of the growth face by approximately this angle as shown in Figure IV.4.28.

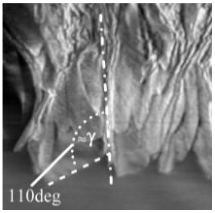

Figure IV.4.28**.** High-temperature AFM micrograph of a growth front of PTT-lamellar crystal at 210°C measured during growth of a PTT spherulite showing an inclination of the growth face by approximately the **γ** angle [28].

Therefore, if the growth axis polarity would ever have to be inversed, the crystal should incline its growth front in the other direction with respect to **a**, which means that there will be a crystal sector with undefined unit cell orientation, which seems problematic. A scheme of the lamellar branching during spherulitic growth where the polarity of the growth axis is invariant is given in Figure IV.4.29.

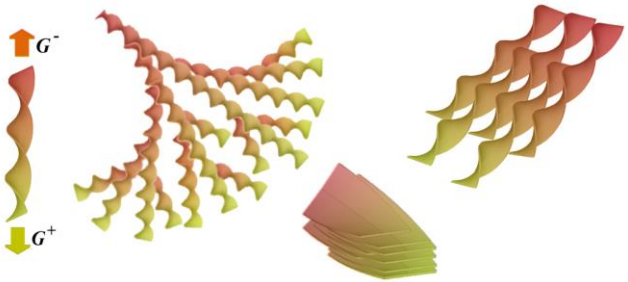

Figure IV.4.29**.** Scheme of the crystallographic lamellar branching during growth of a banded spherulite where the polarity of the growth axis stays invariant (**left**). Possible stacking of the helicoidal-shaped lamellae where all the lamellae twist synchronously and in phase (**right**).

The figure also sketches a possible stacking of the lamellae during the helicoidal twist where all the lamellae twist synchronously and in phase. The exact nature of the proposed crystallographic branching is not fully elucidated at present since the corresponding features cannot be accessed with micro-focus X-ray scattering. However, a qualitative model of the branching can be proposed, which is described in the following.

In the AFM micrograph given in Figure IV.4.30 (left), a splitted growth front is visible. The origin of such shape of the growth front has been assigned in [8] to giant screw dislocations where the edges of the lamella grow faster than the lamella tip for diffusion reasons. This will result in a dip in the center of the lamella, which becomes more and more pronounced with the continuing growth. This indentation in the growth front slows down the local growth rate resulting in a crystallographic defect eventually splitting the lamellar ribbon [35].

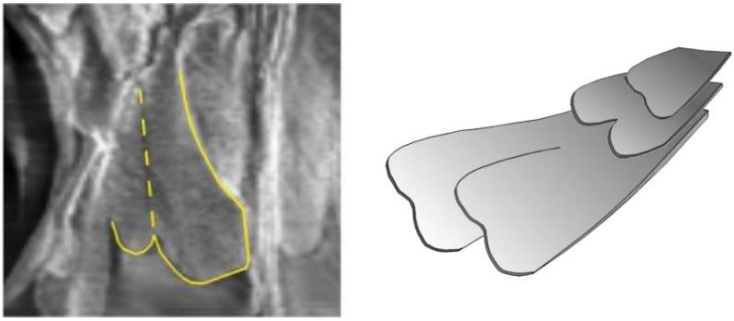

Figure IV.4.30**.** High-temperature AFM micrograph of a growth front of PTT-lamellar crystal at 210°C showing splitting of the lamella tip while growing radially [28] (**left**). Cartoon depicting the mechanism of crystal splaying due to surface stresses (**right**).

Since the completion of the crystal rows stops at this defect, the separated tips of the ribbon now start to splay and grow independently while keeping the same growth axis polarity. Assuming that the surface stresses are the origin of the helicoidal deformation of the crystal, both lamella tips should now bend in the same direction opening space for a growth sideways as schematically depicted in Figure IV.4.30 (right).

IV.5 Conclusions

To address the origin of the lamellar twisting, an in-depth micro-focus X-ray scattering study has been performed on banded spherulites of melt-crystallized polytrimethylene terephthalate (PTT). It is shown that, when scanned with a micro-focus X-ray beam along the spherulite radius, the diffraction peaks of the triclinic lattice of PTT show periodic intensity variations as a function of distance from the spherulite center. This indicates that the lamellar twist has a strictly uniform and regular nature. The latter observation is more compatible with the model explaining the twist as a result of unbalanced surface stresses than the giant screw dislocations.

Although previous literature reports demonstrated that for non-chiral polymers both left- and right-handed helicoids can be present in the same spherulite [36], our data shows that non-chiral polymers such as PTT are in fact not indifferent to the inversion of the lamellar handedness, and that a change in handedness is necessarily accompanied by a change in the sign of the growth vector. Therefore our experimental observations are consonant with the first premise of the *Keith* and *Padden* (*KP*) model, namely that the lamellar twist is driven by unbalanced surface stresses the distribution of which can be mirrored through the plane perpendicular to the growth axis and passing through the origin of the crystal, or the primary nucleus (cf. Figure I.2.8). At the same time, we demonstrate that the overall chain tilt (i.e., the inclination of the c-parameter of the unit cell in the plane perpendicular to the fast growth direction) does not affect the rate and sense of twisting. This calls into question the second premise of the *KP*-model. Instead, the local inclination of the terminal segment of the crystalline stem protruding the lamellar surface can be identified as the origin of the surface stresses. With variation of the crystal thickness as a function of crystallization temperature, the angle and direction of this terminal segment is changed, resulting in a change of the lamellar ribbon chirality.

Three different temperature regions of the lamellar twisting were identified, termed $\mathbf{B_I}$, $\mathbf{B_{II}}$ and $\mathbf{B_{III}}$. At crystallization temperature of 140°C, the first signature of spherulite banding was observed, marking this temperature as the onset of banding $\mathbf{B_o}$. This is likely to coincide with the crystallization regime transition **III** → **II**. The latter finding gives additional support to the origin of the surface stresses as proposed in the *KP*-model. Indeed, when crystallized in regime **III**, the growth rate is dominated by the secondary nucleation adding new nuclei onto the pre-existing growth face without any propagation,

which eliminates the unbalanced stresses at the lamellar surfaces. It is thus clear that the lamellae formed in this crystallization regime should not twist.

In temperature region B_I, the band spacing diverges with temperature following the power-law of the second order. Virtually infinite band spacing is reached at temperature $\mathbf{B_i}$ of 178.5°C, where the spherulite exhibits essentially flat single-crystal-like lamellae. At this point, the unbalanced surface stresses extinct, marking an inversion of the crystal rotation sense. Thus the lamellae formed in temperature regions $\mathbf{B_I}$ and $\mathbf{B_{II}}$ differ in their chirality.

Under assumption that the lamella surface is mainly composed of flexible segments of the PTT chain, a molecular model was built in which the lamellar thickness variation as a function of crystallization temperature is described in terms of the inclination angles of the soft segments protruding the crystal surface. The overall crystal thickness variation, which is comprised within the length of two flexible segments, allows to explain the inversion of the lamellar twist sense. Within temperature regions $\mathbf{B_I}$ and $\mathbf{B_{II}}$ the crystal contains an even number of rigid segments generating a center-symmetrical situation for the stresses on the lamellar surface. Furthermore, the model explains the higher temperature singularity $\mathbf{B_{sp}}$ at about 202.5°C where the band spacing drops by 50%. At this temperature, the crystal thickness approaches the situation where two hard segments are located close to the lamellar surfaces. We speculate that to avoid such unfavorable situation, the crystal incorporates one rigid segment more, which results in a stepwise change of the band spacing. Also, this last transition is accompanied by a decrease of the radial alignment of the fast growth axis (i.e., the **a**-vector of the PTT unit cell) due to unlocking of the lamellar helicoids packing.

Finally, we used the banded spherulites of PTT to explore the structural memory transferred by the lamellae during spherulitic growth. By designing an experiment in which the crystallization temperature was changed stepwise across singularity point B_i, we arrived at conclusion that the lamellae keep information about the growth axis polarity and that the handedness of the lamella helicoids is not preserved across the transition. This conclusion also signifies that the lamellar branching occurs in agreement with crystallographic register and the conventional hypothesis of a “non-crystallographic” branching should be discarded.

REFERENCES

1 Point, J.J., 1953 Bull. Acad. R. Bel., 41, 982.

2 Keith H. D. Jr., 1959 Pol. Sci., 39, 123.

3 Keller A., 1959 Pol. Sci., 39, 139.

4 Keith H. D. Jr. and Padden F J, 1984 Polymer, 25, 8.

5 Frank F.C., 1979 Discuss. Faraday Soc., 68, 7.

6 Lotz B., 2006 Polymer, 47, 3267.

7 Keith H. D. Jr. and Padden F J, 1963 J. Appl. Phys., 34, 2409.

8 Toda A., 2008 Macromolecules, 41, 2484.

9 Gazzano, M., 2000 Biomacromolecules, 1, 604.

10 Tanaka, T., 2005 Polymer , 46, 5673.

11 Hall I.H., "Structure of crystalline polymers" London: Elsevier Appl.Sci. 1984, p.39.

12 Yun J.H., Kuboyama K. and Ougizawa T., 2006, Polymer, 47, 1715.

13 Keith H.D., Padden F.J.Jr. 1959 J.Pol. Sci., 39, 101.

14 Chuang W.-T., Hong P.-D. and Chuah H.H., 2004 Polymer, 45, 2413.

15 Sornette D. "Critical phenomena in natural science" New York: Sprinter:2000 .

16 Auyang S.Y., "Foundations of complex system theories" New York: Cambridge University Press: 1998.

17 Hong P.-D., Chuang W.-T. and Hsu C.-F., 2002, Polymer, 43, 3335.

18 Wu P.-L. and Woo E.M., 2002 J. Pol. Sci. Part B: Pol. Phys. 40, 1571.

19 Wang B., et al., 2001, Polymer, 42, 7171.

20 Hoffman J.D., Davis G.T., Lauritzen Jr. J.I. In: Hannay NB, editor. Treatise on solid state chemistry. Vol 3. New York: Plenum Press, Chapter 7, 1976.

21 T.V. Samulski and E.T. Samulski, 1977 J. Chem. Phys., 66, 2748.

22 Keith H. D. Jr. and Padden F. J., 1996 Macromolecules, 29, 7776.

23 Lotz B., Cheng S.Z.D., 2005 Polymer, 46, 577.

24 M. Hütter, P.J. In't Veld and G.C. Rutledge, Lecture Notes in Physics, G. Reiter and G. Strobl, eds., Vol. 714, pp. 457-480, Springer Verlag, 2007.

25 Rutledge G.C. and Balijepalli S., 1998, J. Chem. Phys., 109, 6523.

26 Rutledge G.C. and Lacks D.J., 1994, J. Phys. Chem., 98, 1222.

27 Ivanov D.A., et al., 2004, Europ. Phys. J. E, 13, 363.

28 Ivanov D.A., et al., 2008, Macromolecules 41, 9224.

29 OkanoK., 1953 Jpn. J.Appl. Phys., 24,176.

30 Keith H.D., 1996 Macromolecules, 29, 7776.

31 Eshelby, J. D. 1964, J. Appl. Phys., 3, 351.

32 Schultz, J.M. and Kinloch D.R., 1969 Polymer, 10, 271.

33 Ye H.M. et al., 2009, Macromolecules, 42, 694.

34 Wunderlich B. Macromolecular Physics, Academic Press, New York, Chapter 3, 1973.

35 Toda A., et al., 2008 Macromolecules, 41, 2484.

36 Nouze Y., et al., 2004 Polymer, 45, 8299.

V. ACCESSING THE 3D-SHAPE OF TWISTED LAMELLA CRYSTALS WITH A COMBINATION OF MICRO-FOCUS X-RAY DIFFRACTION AND COMPUTER SIMULATION

Martin Rosenthal[1], Valeriy A Luchnikov[1], Houssam Hamie[1], Manfred Burghammer[2], Georg Bar[3], and Dimitri A Ivanov[1]

1) Institut de Sciences des Matériaux de Mulhouse, CNRS LRC7228, 15 rue Jean Starcky, 68057 Mulhouse, France

2) European Synchrotron Radiation Facility (ESRF), 6 rue Jules Horowitz, 38043 Grenoble, France

3) Applied Science & Technology/Analytical Sciences, Dow Olefin Verbund GmbH, Schkopau, D16/1.04, Germany

Abstract

In this section, an analytical and computer simulation approach introduced by Ivanov and Luchnikov is applied for the case of twisted crystalline lamellae built of triclinic unit cells of poly(trimethylene terephthalate) (PTT). The model has been developed in approximation of a purely geometric broadening of the X-ray reflections. The theoretical predictions are compared with experimental micro-diffractograms measured on banded spherulites of PTT.

Several features of the experimental diffractograms, namely the azimuthal and fiber-angle broadening, as well as the sequence of appearance of different diffraction peaks and their shape, will be found to be in good agreement with the experimental data. Thus it will be shown, that the cross-sectional profile of the PTT twisted lamellae is not a simple straight section but likely to have a more complicated S-shaped profile. An interesting observation will be described showing that the fiber-angle profile of the equatorial reflections of the PTT lamellar ribbon is invariant of the crystallization temperature.

V.2 Introduction

The structure of banded polymer spherulites has been one of the most intriguing and extensively discussed problems in polymer physics over the last decades starting from the early 1960s with the work of *Keith* an *Padden* [1,2] and the later works of *Lotz* and *Cheng* [3] and *Toda* [4]. Spectacular patterns of concentric extinction rings are revealed by polarized optical micrographs of banded spherulites being interpreted as a result of a highly correlated twisted growth of lamellar crystals [5-7]. In the seminal work of *Keith* and *Padden* [8] the unbalanced stresses appearing on the lamellar surface are suggested to be responsible for the lamellar twist. The twisted lamellar morphologies were studied in much detail on surfaces of chemically-etched spherulites of polyethylene by *Bassett* & *Olley* [9] or by surface-sensitive techniques such as Atomic Force microscopy (AFM) [10-13]. The latter studies in some cases allowed time-resolved imaging of the lamellar growth, and provided structural information as to the shape and spatial organization of the lamellar crystals.

Despite extensive morphological studies performed on banded polymer spherulites, many important issues remain unsolved yet. It is for example still unclear what the exact shape of the twisted lamella is and whether it can be described by the classical helicoid with a uniform twist around its screw axis. To address this question, a detailed micro-structural analysis of banded polymer spherulites in 3D is required, since the 2D micrographs provided by conventional microscopy techniques are insufficient to visualize the spatial lamellar organization in such complex hierarchical structures.

Micro-beam X-ray diffraction has been employed to address these problems, since the beginning of 1960s [14]. More recently, this technique has gained importance due to its enhanced, and continuously improving, spatial resolution achieved on modern synchrotron-based micro-beam setups [15,16]. X-ray micro-diffraction is a rather unique structural analysis tool because it can assess the microstructure of the samples, which are thick enough to exhibit spherulite banding, i.e. for polymer morphologies typical of the bulk. Such sample thicknesses are clearly out of range for conventional Selected-Area Electron Diffraction (SAED). The information on the shape and structure of the twisted lamellar crystals is encoded in the micro-diffraction pattern asymmetry and angular broadening (arcing) of reflections, as well as in the variation of the diffracted intensity as a function of radial distance. In the past, the angular broadening of the off- meridional diffraction peaks in the SAED patterns has been used to analyze the shape of isolated

helicoidal ribbons of a main-chain chiral polyester [17]. Based on this data, the authors concluded about the twist angles for both axes, i.e. the long and short, of the helicoid. However, a systematic approach for the analysis of micro-diffractograms of twisted lamellar crystals in view of a complete reconstruction of their shape in 3D is yet missing.

A theoretical and computer simulation approach was developed by *Ivanov* and *Luchnikov* [18,19] for modeling the micro-beam X-ray diffraction from twisted lamellar ribbons. They propose a peak broadening analysis applicable to studies of materials revealing banded spherulite morphology. Here the angular broadening of the diffraction peaks was attributed to the changing crystal orientation caused by the twisted deformation of the lamellae.

In this work, we describe an analytical and computer simulation approach allowing to comprehend the main features of the micro-diffractograms from twisted crystalline lamellae [18]. It has been developed in the approximation of a purely geometric broadening of the X-ray reflections, i.e. the diffraction peaks broadening due to a finite crystal size along different crystallographic was not taken into account. The theoretical predictions are compared with experimental micro-diffractograms measured on banded spherulites of poly(trimethylene terephthalate), PTT.

V.3 Experimental

Poly(trimethylene terephthalate) (PTT) (Corterra CP 509200, M_w = 35200 g/mol, M_w/M_n = 2) films were prepared by crystallization from the melt at 170°C between glass slides, resulting in films of 30 to 50µm thickness. Free-standing films were obtained by dissolving the glass slides in a dilute aqueous solution of HF. The 2D micro-focus X-ray scattering experiments were carried out on the ID13 beamline of the European Synchrotron Radiation Facility (Grenoble, France) using the wavelength of 1.0 Å. In the experiments, the crossed-Fresnel optics, with a spot size of 500 nm along both axes was used. A MARCCD 165, with a pixel size of 80 microns (not rebinned) was used to record the 2D X-ray pattern. The measurements were performed in transmission geometry with the sample surface normal to the X-ray beam. The region of interest was selected with an on-axis optical microscope operated in reflection mode using the topographic variation between the edge-on and flat-on lamellar crystals. A beam monitor installed upstream the sample provided dose-monitoring for online exposure normalization. The sample was scanned by means of an x-y gantry, the diffraction patterns were collected using a step of 1.0 µm.

V.4 Results and Discussion

V.4.1 The model

In the first approximation, the crystalline lamellae can be considered as quasi-2D objects, i.e. it can be assumed that their thickness is much smaller than their width and length. Therefore the description of the lamella can be reduced to parameterisation of vector $\mathbf{r}(u,v)$ corresponding to the points on the lamella surface

$$\mathbf{r}(u,v) = (x(u,v), y(u,v), z(u,v)) \qquad \text{(E.V.4.1)}$$

The global coordinate system (Ox, Oy, Oz) can be defined in such a way that, in the absence of the lamellar deformation transforming an ideally flat single-crystalline lamella (depicted in dotted line in Figure V.4.1 left) in a helicoid, the Oz axis is parallel to the longitudinal axis of the lamella and the Ox axis is lying in the plane of the lamella.

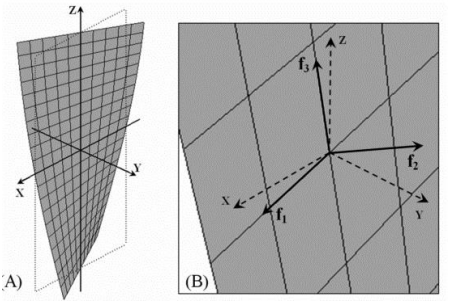

Figure V.4.1. Helicoidally-twisted lamellar surface formed from the initially planar rectangular-shaped lamella, the contour of which is shown with a dotted-line (**left**). The basis vectors of the global coordinate systems in direct space are (x, y, z), (or (x*, y*,z*) for the reciprocal space). The longitudinal axis of the helicoid is along the z-coordinate. A magnified region of the lamellar surface for which the direct-space local and global coordinate systems are indicated. Vectors $\mathbf{f}_1$, $\mathbf{f}_3$ are tangential and $\mathbf{f}_2$ is normal to the surface (**right**).

Since the twisted lamella surface is not planar, in addition to the global coordinate system, at each point of the lamella surface one can define a local orthonormal coordinate system $(\mathbf{f}_1, \mathbf{f}_2, \mathbf{f}_3)$ where $\mathbf{f}_1$ and $\mathbf{f}_3$ are tangential to the surface and $\mathbf{f}_2$ is normal to it (see Figure V.4.1, right). For convenience, the origins of both, the local and global coordinate systems, coincide. The reciprocal lattice vectors can be introduced using the usual crystallographic notation

$$\mathbf{f}_i^* = \left[\mathbf{f}_j, \mathbf{f}_k\right] / \left\langle \mathbf{f}_i, \left[\mathbf{f}_j, \mathbf{f}_k\right] \right\rangle \qquad \text{(E.V.4.2)}$$

where the angular and square brackets denote the scalar and vector products, respectively. The surface of the conventional helicoid obtained by roto-translation of a straight section along its longitudinal axis can be parameterized as follows

$$x = u\cos(\alpha v),\ y = u\sin(\alpha v),\quad z = v \qquad \text{(E. V.4.3)}$$

In equation (E. V.4.3), α is the angle of rotation of the horizontal section of the helicoid occurring upon a shift by a unit length along its longitudinal axis. It is related to the helicoid period P as $P = 2\pi/\alpha$.

The intensity of a diffraction peak with a maximum at $\tilde{\mathbf{q}}$ can be described as

$$I(\mathbf{q}) = \frac{A}{\left(\chi\sqrt{2\pi}\right)^3} \int \exp\left(-\frac{\left(\mathbf{q} - \tilde{\mathbf{q}}(u,v)\right)^2}{2\chi^2}\right) \cdot J(\mathbf{r}(u,v)) \cdot \left\langle \mathbf{m}, \mathbf{n}(u,v) \right\rangle du dv \qquad \text{(E. V.4.4)}$$

In equation (E. V.4.4) χ stands for the "natural" (i.e., pertinent to the initially planar lamella) half-width of the diffraction peak, A is a constant, $J(\mathbf{r}(u,v))$ is the incident beam intensity at point $\mathbf{r}(u,v)$ of the lamella, and $\left\langle \mathbf{m}, \mathbf{n}(u,v) \right\rangle$ is the scalar product of the unit vectors parallel to the incident beam direction $\mathbf{m}$ and the vector $\mathbf{n}$ normal to the lamellar helicoid at point $\mathbf{r}(u,v)$, respectively. To compute the total diffracted intensity $I(\mathbf{q})$, one has to sum up the contributions from all reflections having non-zero intensity at this point of the reciprocal space.

Using equations (E. II.2.1) to (E. V.4.4) one can numerically calculate the diffracted intensity distributions for the model helicoidally-twisted lamellae. For example, the geometrical broadening of reflections, i.e. the broadening which is only due to the curvature of the helicoid, is illustrated in Figure V.4.2.

In this case, the intensity of (111) peak is computed for a lamella with a cubic crystalline lattice oriented parallel to the axes of the local coordinate system. It can be seen that for the same size and position of the incident beam (cf. Figure V.4.2, left panels) the lamella with a higher rate of twist (Figure V.4.2, bottom) generates a broader diffraction peak. In this case, the intensity distribution is shown on the Polanyi sphere, i.e. the sphere

with radius equal to $\tilde{\mathbf{q}}$ [20]. The described numerical approach can be easily extended to any symmetry of the crystalline lattice and any orientation of the lattice with respect to the lamellar basal plane. It can thus be used as a tool to model the experimental micro-diffractograms.

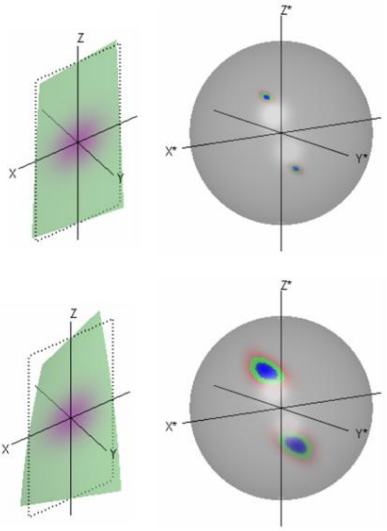

Figure V.4.2**.** The deviation of the lamellar shape from the flat planar shape (indicated by the dotted outline) due to the twisting deformation applied (**left**). The shape of the (111) reflection in the reciprocal space as projected on the *Polaniy* sphere for two rates of the helicoid twist(**right**): α = 0.25 (**top**) and α = 0.75(**bottom**).

The experimental part of the work was performed on "quasi-2D" banded spherulites of PTT composed of the lamellar helicoids growing radially outward from the center. In this case, the dimensionality of the spherulite reflects the simple fact that the spherulite diameter is much larger than its thickness. PTT forms a crystalline lattice of a low symmetry (space group P-1). The unit cell comprises two monomers of the same chain arranged in a complex *zig-zag* conformation.

V.4.2 Analysis of the azimuthal peak broadening for the equatorial peaks

The numerical approach described above can help understanding the experimentally observed variation in the azimuthal peak width for the equatorial peaks, as well as variations of the diffracted intensity and asymmetry of non-equatorial reflections such as

the 102/1-1-2 doublet. Thus the asymmetry of the non-equatorial peaks intensity distribution results in an azimuthal shift of the reflection on the diffractogram, while the peak passes through the reflection conditions, i.e. it intersects the *Ewald* sphere.

The azimuthal width of diffraction peaks from a twisted lamellar crystal strongly depends on the direction of the corresponding reciprocal space vector with respect to the axis of rotation and with respect to the crystal surface, as illustrated in Figure V.4.3. Thus, the equatorial peak (010) is the broadest among the three peaks displayed in the figure.

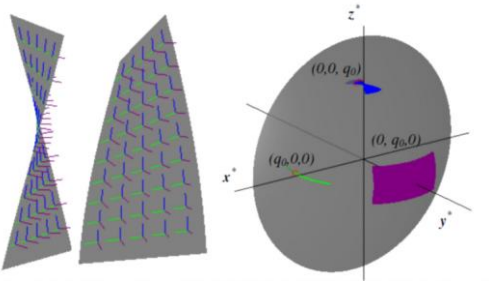

Figure V.4.3. Views of the twisted lamellar crystal, with the axes of the local coordinate system indicated (**left**). The half-width to period ratio equals 0.05. Schematic representation of the Ewald sphere and the calculated shapes of the (h00), (0k0) and (00l) reflections (**right**).

The other equatorial peak, i.e. (100), merges on a thin equatorial arc, while the most unusual behaviour is exhibited by the meridional (001) peak, which has a "bowtie" shape. It should be noted, that here the peaks are given for the case of a cubic lattice, meaning that the axes of the reciprocal- and direct-space local coordinate system are collinear.

It is instructive to estimate the angular broadening of different diffraction peaks, as this is a measurable value in micro-beam X-ray diffraction experiments. The position of a peak can be described in polar coordinates by angles $\boldsymbol{\rho}$ and $\boldsymbol{\varphi}$, where $\boldsymbol{\rho}$ is the angle with the z*-axis (azimuthal angle), and φ is the angle between the projection of the peak on the x*,y* plane and the x*-axis (fiber angle). Accordingly, the broadening of the peaks can occur in both directions.

As far the azimuthal broadening is concerned, it is given as $\Delta\rho = \rho_{\max} - \rho_{\min}$, where $\rho_{\max}$ and $\rho_{\min}$ are the maximal and minimal angles of the diffraction peak with the z*-axis measured during scanning of the micro-beam along the helicoidal axis. A simple calculation for the case of an orthorhombic lattice reported elsewhere [18], is given by

$$\Delta\theta \approx 2\alpha W k \Big/ \sqrt{h^2 + k^2} \qquad \text{(E.V.4.5)}$$

In equation ((E.V.4.5)), W stands for the width of the lamellar ribbon. The equatorial (010) diffraction peak has the maximum width $\Delta\rho \approx 2\alpha W = 4\pi W/P$. When the direction of the reciprocal space vector peak inclines with respect to the crystal surface its angular width decreases. Thus, for the (100) diffraction peak, no azimuthal broadening is expected, i.e. $\Delta\rho \approx 0$.

For the case of a triclinic unit cell, where the axis of rotation coincides with the crystallographic **a**-axis, the fraction $k/\sqrt{h^2 + k^2}$ should be replaced by $\cos(\varphi)$ where φ corresponds the angle between the considered reflection and the normal of the lamellar ribbon i.e. the main interference maximum in SAXS. Thus, the azimuthal broadening of the equatorial peaks depends linearly on $\cos(\varphi)$.

$$\Delta\rho \approx 2\alpha W \cos(\varphi) \qquad \text{(E. V.4.6)}$$

The equatorial diffraction peak, which is normal to the lamellar surface, has the maximum possible width, i.e. $\Delta\rho \approx 2\alpha W = 4\pi W/P$. When the direction of the equatorial peak inclines with respect to the crystal surface its azimuthal width decreases (cf. Figure V.4.4). For diffraction peaks whose reciprocal space vectors are tangential to the lamellar ribbon, no azimuthal broadening is expected i.e. $\Delta\rho \approx 0$.

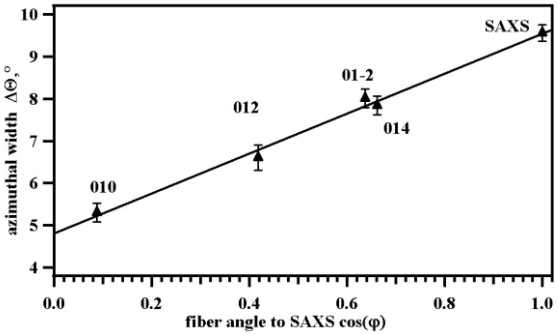

Figure V.4.4. Azimuthal half-width of the main equatorial peaks of PTT as a function of the cosine of the fiber angle **φ** measured with respect to the lamellar ribbon normal, i.e. the SAXS interference maximum.

The estimation of the fiber-angle broadening of the peak, $\Delta\rho = \rho_{\max} - \rho_{\min}$, is less straightforward. Generally, no explicit analytical formula for $\Delta\varphi$ can be found. However, from the screw-axis symmetry of the system it follows that the fiber-angle width of the equatorial peaks should be proportional to the height of the illuminated part H of the helicoid: $\Delta\varphi \approx \alpha H$. Thus, if $H \geq P$, i.e. the height of the beam is larger than the helicoid's period, so that $\Delta\varphi = 2\pi$.

V.4.3 Analysis of the azimuthal peak shift

To reproduce the experimental diffractograms, the calculations have been performed for the model helicoid built using the triclinic lattice of PTT correctly oriented with respect to the helicoidal axes. The intensity recorded on a 2D-detector for each angular position of the lamellar crystal can be found at the intersection between the *Polanyi* sphere with the radius equal to the norm of the scattering vector of a particular reflection and the *Ewald* sphere corresponding to the observation conditions (Figure V.4.5).

Scanning the micro-beam along the spherulite radius is in this case equivalent to rotation of the *Polanyi* sphere about the longitudinal axis of the helicoid while keeping the position of the *Ewald* sphere invariable. It is noteworthy that the situation here is more complicated than the one encountered in a conventional fiber tilting experiment where the intensity of all the peaks is uniformly distributed along the parallels of the *Polanyi* sphere. By contrast, in our case the intensity distribution for the non-equatorial reflections has a particular drop-like shape (cf. Figure V.4.5, A).

This shape can account for the observed variation of the azimuthal position of the reflections during radial scans. Indeed, the simulation (cf. Figure V.4.5, B) reproduces the main features of the experimental diffractograms (cf. Figure V.4.5, C) such as the sequence of appearance and asymmetry of the off-meridional reflections.

More specifically, it can be observed that the azimuthal position of the reflections is not constant and that, when the peaks exit the reflection conditions, on the 2D-detector it moves down, toward the equatorial plane (cf. solid and dotted white radial lines in Figure V.4.5, C).

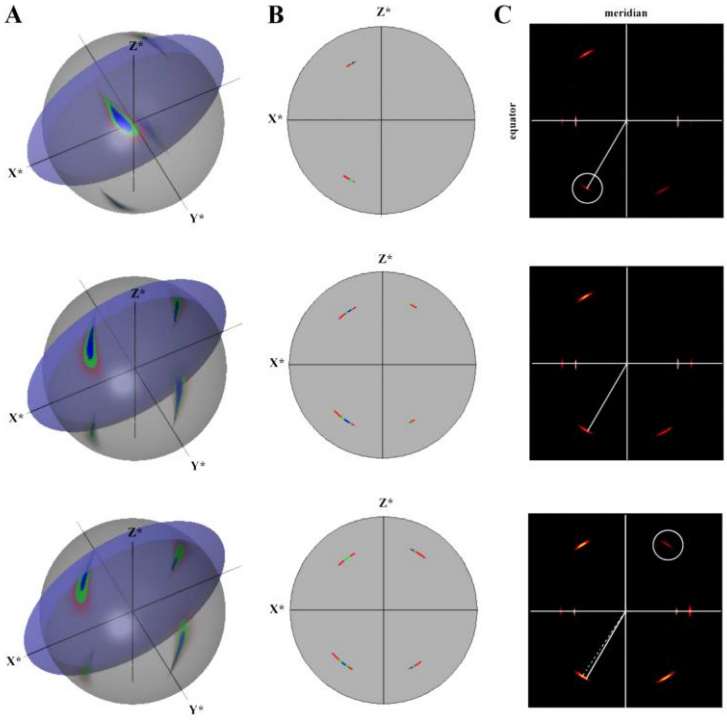

Figure V.4.5. Calculated peak intensity distribution of the 102 reflection visualized on the *Polani* sphere (gray) and its intersection with the *Ewald* sphere (violet) in z-projection (**A**). Planar projection of the intersection of the *Polani* and Ewald spheres showing the calculated azimuthal intensity distribution for the 102 reflection (**B**). Experimental 2D-diffractograms recorded during a radial micro-focus scan for a PTT spherulite melt-crystallized at 170°C(**C**). The 102 peak (encircled in red) enters the reflection conditions in the bottom left quadrant (**top panel**). The reflection moves azimuthally toward the equator (**middle panel**). The reflex reaches its maximum intensity while still moving upward (**bottom panel**). Simultaneously, the -10-2 peaks enters the reflection conditions in the top right quadrant (encircled in red).

V.4.4 Detailed shape of the lamellar ribbon

The question on a possible correlation between the chirality of the polymer chain and handedness of the lamella helicoids, which was mentioned in the Introduction section, can be addressed for the case of PTT using the Scanning Electron Microscopy images (Figure V.4.6).

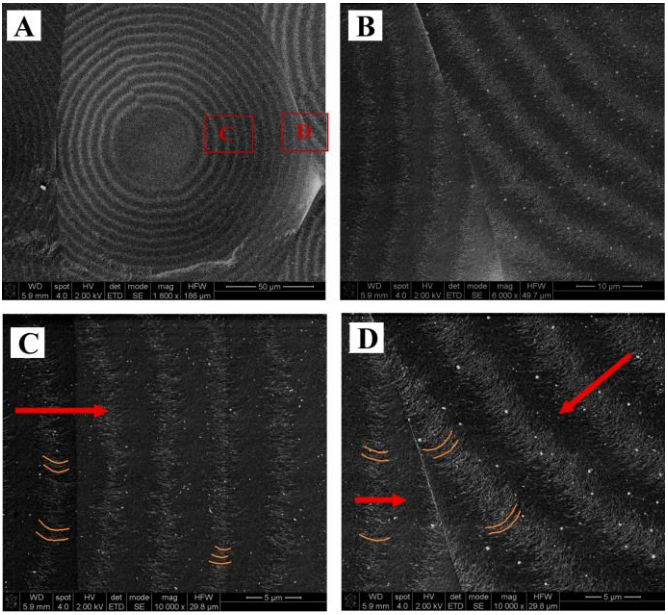

Figure V.4.6**.** Scanning electron micrographs of a melt-crystallized film of PTT revealing the banded texture (**A,B**). Close-up of the region located to the right from the spherulite center where inversed C-shaped lamellae, as viewed from the center, are observed (marked by the orange arcs) (**C**). This shape corresponds to a left-handed twist. Close-up of the region located to the left (middle) from the spherulite center showing C-shaped lamellae, as viewed from the center (**D**). This shape corresponds to a right-handed twist. The radial direction is indicated by the red arrow.

According to the literature [21], the handedness of the lamellar helicoids can be easily deduced from orientation of the C-shaped crystals observed on the spherulite surface. The sketches given in Figure V.4.7 displays right- and left-handed helicoids sliced with a plane crossing the helicoid axis.

The bending direction of the resulting C-shaped crystals, when viewed along the growth direction, is to the right and left side, respectively. It is noteworthy that, when the slicing plane is parallel or nearly parallel to the longitudinal axis of the helicoid, the crystal cross-sections are S-shaped. Therefore in order to exhibit the C-shaped crystals at the surface, the spherulite should nucleate at a certain depth, within the film. For the PTT spherulites, both orientations of the C-shaped crystals are observed (Figure V.4.6. C, D), which means that it forms left- and right-handed helicoids. This result is in agreement with a previous report [22] suggesting that non-chiral polymers are able to form both left- and right-handed lamellar helicoids.

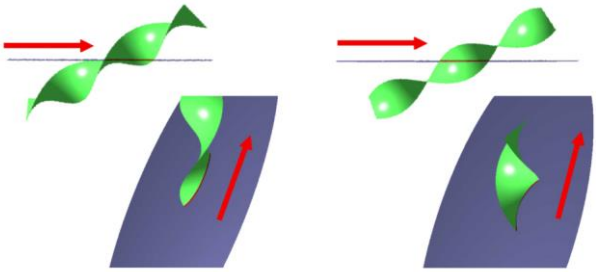

Figure V.4.7. schematic illustration explaining the origin of the observed lamellar profiles for the left- and right-handed helicoids.

V.4.5 Exploring the lamella cross-section

Generally, there exist no trivial reasons why the twisted crystalline lamellae should adopt the shape of the classical helicoid, which has straight cross-section profiles in the planes perpendicular to the main axis. Rather, it can be well assumed that other types of cross-section profiles exist, such as S- or C-shapes reported for the case of PE [9] or for PTT [23], being of particular importance for the present study. A surface with an S-shaped profile can be constructed for instance by a screw-axis operation on two adjacent arcs (cf. Figure V.4.8).

Figure V.4.8. Helicoidally-twisted lamella with an S-shaped cross-section.

It is clear that the convexity of the S-shape profile directly affects the fiber-angle width of the reflections. Thus, with more and more convex S-profiles, the equatorial reflections will be more often in the reflection conditions. For the limiting case of S-shape consisting of two adjacent semi-circles, all reflections will be observed permanently.

As outlined by *Keith* and *Padden* [8] for the case of PE, there are two possibilities of how the crystalline stems can be arranged in the S- or C-shaped lamellar crystals (cf. Figure V.4.9 (2) and (3)).

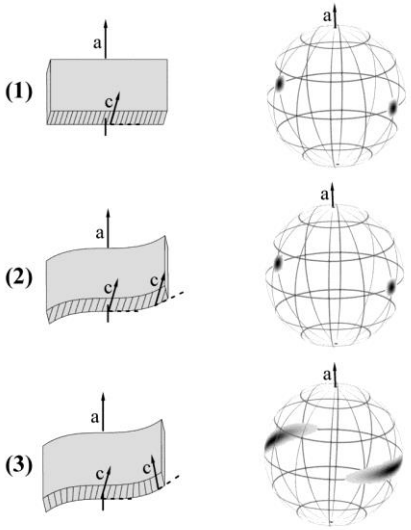

Figure V.4.9. Schematic drawing of twisted lamellar crystals with the corresponding pole figures drawn for an arbitrary equatorial, i.e. 0kl, reflection. The **c**-vector coincides with the crystalline stem orientation. (1) Undeformed lamellar crystal is given for the sake of comparison. (2) Lamella with a curved cross-section in which the crystalline stem directions are all parallel, as described by *Bassett* and *Hodge* [24]. (3) Elastically-bent lamella in which the local tilt angle of the crystalline stems is invariable due to the molecular shearing. This results in varying orientation of the **c**-vector along the lamella cross-section [8].

For the case depicted in Figure V.4.9 (2), the molecular orientation is uniform all the way across the lamellar cross-section, which exhibits curvature toward the lateral outer edges. Thus, the direction of the **c**-axis is invariable everywhere. Since all constitutive unit cells are organized in a strictly parallel way, the equatorial crystallographic reflections won't broaden in the fiber-angle direction. Obviously, the cross-sectional shape with parallel crystalline stems is indistinguishable from a plain flat lamellar ribbon by means of micro-focus diffraction alone, as the diffraction patterns can basically reveal only point-like reflections having natural width, as it is the case of single crystal diffraction (cf. Figure V.4.9, right). In contrast, for another type of the curved lamellar shape where the crystalline stems keep the same local tilt angle to the lamella normal (cf. Figure V.4.9, 3), the equatorial diffraction peaks broaden along φ.

The experimental data on the fiber-angle broadening of the 010 peak for the melt-crystallized PTT spherulites are shown in Figure V.4.11 (left). After normalization of the maximum integral intensity to unity, it can be seen that the half width of the peaks exceeds 45 deg. Therefore it can be conjectured that the real lamella shape is closer to an S-shaped helicoid than to the classical helicoid with a straight section for the width of the peak is by far larger than its natural width (cf. Figure V.4.11, left, and Figure V.4.10).

Interestingly, there are no significant differences in the peak width with crystallization temperature, whereas the band spacing varies quite significantly. This leads to the assumption that the shape of the helicoid's cross-section is invariant with crystallization temperature.

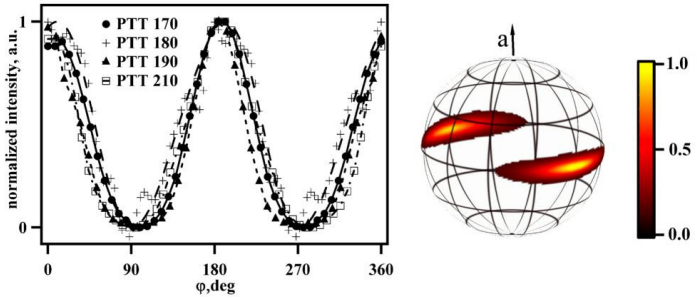

Figure V.4.11. Normalized integral intensity of the 010 refection as a function of the fiber angle φ for different crystallization temperatures of PTT indicated on the graph (**left**). The curves reveal virtually no variation of the fiber-angle broadening with crystallization temperature. Pole figure corresponding to the 010 reflection (**right**).

Furthermore, the width of the lamella relative to the band spacing should be also constant in this case. The temperature evolution of the lamellar shape can thus be viewed as a homothetic transformation proportional to the band spacing. The particular shape of the S- can be conjectured since the shape of the fiber angle broadening corresponds to the histogram of the orientation variation of the stems. The modeling of a real experiment will require another modification to be added. One should take into account possible azimuthal broadening of the reflections which is not directly related to the helicoidal shape. Such broadening can originate, for instance, from non-perfect alignment of the twisting axes or a de-phasing of the twisted ribbons.

The cross-sectional shape was modeled starting with infinite radius applied to the half width of the ribbon. The results of the simulation are given for the ratio of 0.35 and 0.2 for

the circular S-shape in Figure V.4.12 (bottom). The fiber-angle distribution broadens with increasing the strength of the S-shape, which is in-line with the qualitative consideration given above.

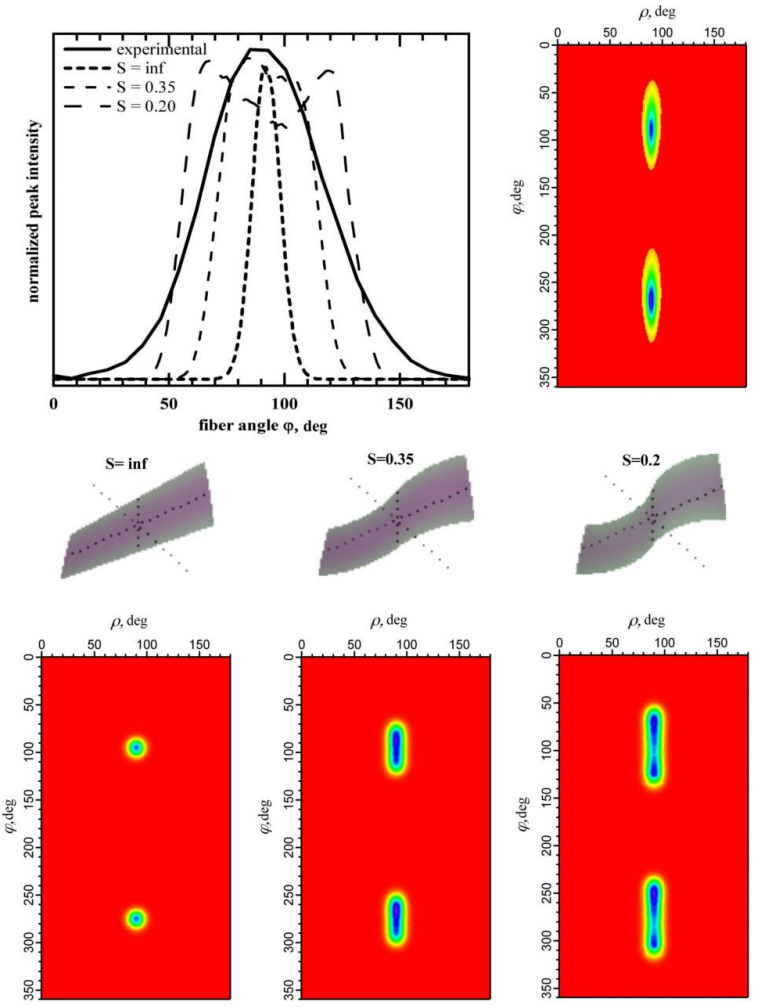

Figure V.4.12. Comparison of the simulated and experimental peak broadening. (**Top left**) The fiber-angle profile of the equatorial 010 reflection for the experiment (solid) and simulation (dashed). (**Top right**) Experimental 2D-profile of the 010 reflection. (**Middle row**) Cartoons of the lamellae with different S-shape parameter indicated above the diagrams and the corresponding 2D plots (**bottom row**) of the simulated 010 reflection intensity.

A surface with an S-shaped profile can be constructed for instance by a continuous screw symmetry translation of two adjacent circular arcs. Parametrically such a surface can be described as

$$\begin{aligned} x &= \left(\pm x_0 + R\cdot\sin\left(\beta u+\varphi\right)\right)\cdot\cos(\alpha\cdot v) - \left(\mp y_0 \mp R\cdot\cos\left(\beta u+\varphi\right)\right)\sin\left(\alpha v\right) \\ y &= \left(\pm x_0 + R\cdot\sin\left(\beta u+\varphi\right)\right)\cdot\sin(\alpha\cdot v) + \left(\mp y_0 \mp R\cdot\cos\left(\beta u+\varphi\right)\right)\cos\left(\alpha v\right) \\ z &= v \end{aligned} \qquad \text{(E. V.4.7)}$$

In equation (E. V.4.7) x_0 and $y_0$correspond to

$$\begin{aligned} x_0 &= R\sin\left(W/\left[2R\right]\right) \\ y_0 &= -R\cos\left(W/\left[2R\right]\right) \end{aligned} \qquad \text{(E. V.4.8)}$$

and $\beta = 1/R$, $\varphi = -W/(2R)$, R is the curvature radius of the branches of the S-shape. The varying signs in equation (E. V.4.7) apply to the "left" and the "right" halves of the S-shape. Although the derivation of the formulae for the local coordinate system vectors is straightforward, they are too bulky to be given here. It is clear that the convexity of the S-shape directly affects the saggital width of the reflexes. For more convex S-profiles, a reflection will be more often in the diffraction conditions. For the limiting case of the S-shape consisting of two adjacent semi-circles, all equatorial reflections will be observed permanently.

The peak broadening observed in the experiment was modeled by simulation using a circular segment S-shaped lamellar helicoid (Figure V.4.12). The parameter describing the circular lamellar deformation is the quotient of the circular radius normalized by the lateral half width of the lamellar ribbon. However, a sufficient approximation the exact profile of the distribution derived from the experiment, as shown in Figure V.4.12 (top), has not been reached with the circular S-shape. The reasons for this could be several, starting from fact that the exact profile of the S-shape could be much more complicated than a simple circle. A mechanical model taking into account the bending moments of the ribbon due to its finite thickness leads to the mechanical bending line corresponding to higher order polynoms. Another reason could be underestimation of the growth axis miss-orientation and other factors leading to convolution effects not accounted for by the model.

V.5 Conclusions

A computer simulation approach introduced by *Ivanov* and *Luchnikov* was applied for the case of the twisted lamellae built of triclinic unit cells of PTT. Several features of the experimental diffractograms, namely the azimuthal and fiber-angle broadening, as well as the sequence of appearance of different diffraction peaks and their shape, was in good agreement with the experimental results.

It was shown that the cross-sectional profile of the PTT twisted lamellae is not a simple straight section but likely to have a more complicated S-shaped profile. Furthermore, the fiber-angle profile of the equatorial reflections was shown to be invariant of the crystallization temperature indicating that the width of the lamellar ribbon increases homothetically with the band spacing.

REFERENCES

1 Keith H.D., Padden Jr. F.J, 1964 J.Appl. Phys., 35, 1270.
2 Keith H.D., Padden Jr. F.J, 1984 Polymer, 25, 8.
3 Lotz B, Cheng SZD, 2005 Polymer 46, 577.
4 Toda A., et al., 2008 Macromol. 41,2484.
5 Keller A., Polym. Sci. 1959, 39, 139.
6 Price FP. J Polym Sci 1959, 39, 139.
7 Keith H.D., Padden Jr. F.J., 1959 J Polym Sci, 39, 123.
8 Keith H.D., Padden Jr. F.J., 1984 Polymer 25, 28.
9 Bassett D.C., Olley R.H., 1984 Polymer 25, 935.
10 Ivanov D A; et al., 1999 Polymer 40, 5899.
11 Basire C., Ivanov D. A., 2000 Phys. Rev. Lett. 85, 5587.
12 Ivanov D. A., et al., 2001 Macromolecules 34, 8944.
13 Ivanov D. A., et al., 2008 Macromolecules 41, 9224.
14 Fujiwara Y., 1960 J. Appl. Pol.Sci. 4, 10.
15 Gazzano M., et al., 2001 Macromol. Chem. Phys. 202, 1405.
16 Tanaka et al., 2005 Polymer 46, 5673.
17 Li C.Y., et al., 1999, Phys. Rev. Lett. 83, 4558.
18 Luchnikov V.A. and Ivanov D. A., 2009 J. Appl. Cryst 42, 673.
19 Luchnikov V.A. and Ivanov D. A., 2010 J. Appl. Cryst 43, 578.
20 Stribeck N. 1921 Acta Cryst. A 65 46.
21 Lotz B., et al., 1989 J. Pol. Sci. B Pol. Phys. 27, 561.
22 Nozue Y, et al., 2004 Polymer 45, 8299.
23 Ikehara T., et al., 2007 J. Pol. Sci. B Pol. Phys., 45, 1122.
24 Bassed D.C., Hodge A. M., 1978.

VI. GENERAL CONCLUSIONS

In this last chapter of the manuscript, the results of previous topic chapters are summarized. The most important findings will be confronted with the literature data.

In the first part, the use of micro-focus X-ray scattering is evaluated in terms of its capacity to address the morphological features of twisted lamellar crystals. In the second part, a molecular model accounting for the lamellar twist in PTT is proposed and critically compared with the models found in the literature. Furthermore, the results of a computer simulation approach to address the 3D lamellar shape are discussed.

VI.1 Analyzing banded polymer spherulites using micro-focus X-ray scattering

To address the origin of the lamellar twisting phenomenon in polytrimethylene terephthalate (PTT), an in-depth micro-focus X-ray scattering study has been conducted. The aim of the work was first to check whether the two main postulates of the *Keith* and *Padden* (*KP*)-model are applicable to the lamellar twisting in PTT, or if other models can be envisaged as well, e.g. the successive giant screw dislocations model.

The *KP*-model postulates that (1) the lamellar twisting stems from unbalanced surface stresses rather than from successive giant screw dislocations. (2) The origin of the unbalanced surface stresses is due to differential chain fold congestion on the lamellar basal surfaces due to the crystalline stem tilt along the lateral direction of the crystal.

A direct consequence from the second premise of the *KP*-model is that the sense of the lamellar twisting has to be opposite for the positive and negative growth directions. This comes from the fact that the chirality introduced by the lateral inclination of the stems is mirror-symmetric about the plane normal to the growth vector.

The system studied in the present work, provides an excellent means to check the premises of the *Keith* and *Padden* model by correlating the observed chirality of the lamellar helicoids to the observed chain tilt. In order to do so, the orientation of the unit cell was identified for the PTT films crystallized in the temperature range from 170°C to 200°C. The chain tilt was calculated using the radial offset of the equatorial reflections with regard to the main interference maximum in the SAXS region normalized by the twist period.

VI.1.1 Twist sense and growth axis polarity in helicoidal lamellar crystals

It has been shown in the work that the micro-focus X-ray scattering is an appropriate tool to address the local morphological features of twisted lamellar crystals with a high spatial resolution. Importantly, quasi-bulk samples are amenable to analysis, as it is the case of the studied PTT films having a thickness of several tens of microns. When scanning along the radial direction of a spherulite, the fast crystal growth direction could be identified as the axis of twisting. Furthermore, it was observed that the diffraction peaks of the triclinic lattice of PTT show a periodical pattern as a function of the distance from the spherulite center. This indicates that the lamellar twist has a strictly uniform and

regular nature. The latter observation is more compatible with the model explaining the twist as a result of unbalanced surface stresses than the giant screw dislocations.

Using the *Ewald* sphere construction the handedness of the lamellar twist could be derived using for example any equatorial reflection and its symmetric counter-part. It was shown that both senses of rotation are present in the spherulites. However, spherulitic sectors with the same handedness are observed showing a strong lateral correlation of the twisted lamellar ribbons. Together with the azimuthal and sagittal intensity distributions of the reflections a vector model of the twisting crystal could be generated allowing calculating the rotation of the unit cell as a function of the radial distance. Due to the low symmetry of the unit cell of PTT (triclinic, P-1) it is possible to differentiate between the growth along the negative and positive growth vector. This is not possible for crystals having a high symmetry as it is the case for PE being characterized by an orthorhombic unit cell.

Therefore it was shown that non-chiral polymers are in fact not indifferent to the inversion of the lamellar handedness, and that a change in handedness is necessarily accompanied by a change in the sign of the growth vector. Our experimental observations are consonant with the first premise of the *Keith* and *Padden* (*KP*) model, namely that the lamellar twist is driven by unbalanced surface stresses. Starting from this, chirality parameters were introduced correlating the sense of the lamellar twist; positive (***G***) or negative (***-G***) growth vector vs. left-handed (*L*) or right-handed (*R*) sense of twisting. The set of chiral parameters for the twisting PTT lamella crystallized below 180°C was identified as (***G*** / *L*) or (***-G*** / *R*) respectively.

VI.1.2 Addressing the chain tilt in a bulk sample

Since scanning along the helicoidal axis corresponds to a tilting measurement as it is performed in conventional crystallography work, the inclination of the crystalline stems in the PTT crystal can be addressed in a quasi-bulk samples using a combination of SAXS and WAXS. The chain tilt was identified to be about 4 deg in the positive **b*** direction with standard deviation of less than 2 deg. The identification of the chain tilt in bulk isotropic samples has not been done before to our knowledge.

VI.2 Crystallization temperature dependence of lamellar twisting

VI.2.1 Banding and the crystal growth regimes

The PTT twisting behavior was investigated as a function of crystallization temperature. Three different temperature regions of the lamellar twisting were identified, termed $\mathbf{B_I}$, $\mathbf{B_{II}}$ and $\mathbf{B_{III}}$. At crystallization temperature of 140°C, the first signature of spherulite banding was observed, marking this temperature as the onset of banding $\mathbf{B_o}$. This is likely to coincide with a change in the crystallization regime **III** → **II**. The latter finding gives support to the origin of the surfaces stresses as proposed in the *KP*-model. Indeed, when crystallized in regime **III**, the growth rate is dominated by the secondary nucleation adding new nuclei onto the pre-existing growth face, which eliminates unbalanced stresses at the lamellar surfaces. It is thus clear that the lamellae formed in this crystallization regime should not twist.

VI.2.2 Inversion of chirality

In temperature region $\mathbf{B_I}$, the band spacing diverges with temperature following the power-law of the second order. Virtually infinite band spacing is reached at temperature $\mathbf{B_i}$ of 178.5°C, where the spherulite exhibits essentially flat single-crystal-like lamellae. At this point, the unbalanced surface stresses extinct, marking an inversion of the crystal rotation sense. This corresponds to inversion of the chirality parameters sets discussed above. Thus the set of chiral parameters for the twisting PTT lamella crystallized above $\mathbf{B_i}$ was identified as (***G*** / *R*) and (***-G*** / *L*), respectively. Thus the lamellae formed in temperature regions $\mathbf{B_I}$ and $\mathbf{B_{II}}$ are opposite in their chirality.

VI.2.3 Chain tilt vs. twisting: the second premise of the Keith and Padden model

We have shown that the overall chain tilt (i.e., the inclination of the **c**-parameter of the unit cell in the plane perpendicular to the fast growth direction) does not change its value and direction with crystallization temperature. From this finding it is obvious that the ***chain tilt does not affect the rate and sense of twisting***. This calls into question the second premise of the *KP*-model. Instead, the local inclination of the terminal segment of the crystalline stem protruding the lamellar surface can be identified as the origin of the surface stresses. With variation of the crystal thickness as a function of crystallization

temperature the angle and direction of this segment is changed, resulting in a change of the lamellar ribbon chirality.

Generally, the crystalline stem conformation of PE, which *Keith* and *Padden* mainly refer to in their works, is strongly different from that of PTT. First, in the case of PE the chain forms a planar *zig-zag* while the PTT chain adopts a complex conformation where successive monomers form parts of alternating right-and left-handed helices. Thus, globally the PTT chain does not exhibit chirality, and can be assimilated to a *zig-zag* conformation in the **ac** and **bc** projections. Second, the crystalline stems of PE and PTT remarkably differ in their dimensions. Thus, the **c**-parameter of the PTT unit cell is more than seven times larger than that of PE while the typical crystal thickness is about four times smaller. Thus, in PE lamella many tens of *zig-zags* are present in one crystalline stem while this number is less than three for any melt-crystallized PTT. Therefore statistically the local inclination of a single segment in PE lamellae won't play any role, while for PTT each segment of its *zig-zag* corresponds to more than 20% of crystalline stem length. From such a simple observation it follows that, even if the crystal thickness variation across the PTT sample is on the order of 10%, the segments of the crystalline stems protruding the lamella surface will still be the same.

In order to address the surface stresses on the lamellar surfaces, variation of the twisting periods was correlated to the crystal thickness in the frame of a simple mechanical approach where the twisting period is proportional to the square of the crystal thickness. From this it can be seen that the unbalanced surface stresses rapidly decay in the range of crystal thickness values comprised between 3.1 and 3.5 nm marking the inversion temperature $\mathbf{B_i}$. Above this range, the stresses become negative but do not evolve much in terms of their absolute values. This result shows that, in modeling the twisting behavior of lamellar crystals, one cannot assume that the stress is a slowly changing function of the lamellar thickness.

The observed lamellar twisting in PTT was also compared to the mechanism of axial screw dislocation generation, where a sequential creation of screw dislocations of the same handedness will evolve in a macroscopic twist. To this end, the observed variation of the twisting period was correlated to the model of screw dislocations generated by thermal fluctuations. In this case, the logarithm of the twisting period should be proportional to the cube of the lamellar thickness. Starting from this assumption it is clear that this model does not allow the twisting period to decrease with increasing temperature as it is the case in

temperature region $\mathbf{B_{II}}$. Therefore, the explanation for the origin of the lamellar twist based on the idea of successive screw dislocations is not appropriate for the case of PTT.

VI.2.4 Molecular model accounting for the origin of surface stresses

Under assumption that the lamella surface is mainly composed of flexible chain segments, a molecular model was built in which the lamellar thickness variation as a function of crystallization temperature is described in terms of the inclination angles of the soft segments protruding the crystal surface. The overall crystal thickness variation, which is comprised within two flexible segments length, allows explaining the inversion of the lamellar twist sense. Within temperature regions $\mathbf{B_I}$ and $\mathbf{B_{II}}$ the crystal contains an even number of rigid segments generating a center-symmetrical situation for the stresses on the lamellar surface.

Furthermore, the model explains the higher temperature singularity $\mathbf{B_{sp}}$ at about 202.5°C where the band spacing drops by 50%. At this temperature, the crystal thickness approaches the situation where two hard segments are located close to the lamellar surfaces. To avoid this unfavorable situation, the crystal might include one rigid segment more by simultaneously changing the symmetry of the top and bottom stress distributions, which results in a stepwise change of the band spacing. Also, this last transition is accompanied by a decrease of the radial orientation of the fast growth axis (i.e., the **a**-vector of the PTT unit cell) due to unlocking of the lamellar helicoids packing.

VI.2.5 Structural memory transferred during crystal branching and splaying

Finally, we used the banded spherulites of PTT to identify the structural memory transferred by the lamellae during spherulitic growth. By designing an experiment in which the crystallization temperature was changed stepwise across singularity point $\mathbf{B_i}$, we arrived at conclusion that the lamellae keep information about the growth axis polarity and that the handedness of the lamella helicoids is not preserved across the transition. This conclusion also signifies that the lamellar branching occurs in agreement with crystallographic register and the conventional hypothesis of a "non-crystallographic" lamellar branching should be discarded.

VI.3 Simulation of scattering from twisted helicoids

To deepen the understanding of the crystal twist and gain additional insights about the 3D-shape of the lamellae, a computer simulation approach introduced by *Ivanov* and *Luchnikov* was applied for the case of the twisted lamellae built of triclinic unit cells of PTT. Several features of the experimental diffractograms, namely the azimuthal and fiber-angle broadening, as well as the sequence of appearance of different diffraction peaks and their shape, was shown to be in good agreement with the experimental results. It was shown that the cross-sectional profile of the PTT twisted lamellae is not a simple straight section but likely to have a more complicated S-shaped profile. Furthermore, the fiber-angle profile of the equatorial reflections was shown to be invariant of the crystallization temperature indicating that the width of the lamellar ribbon growths homothetically with the band spacing.

RÉSUMÉ

Dans cette section, nous allons présenter brièvement nos résultats les plus marquants obtenus au cours de ce travail. Ces résultats seront situés dans le contexte plus général des recherches effectuées dans le domaine de la cristallisation des cristaux polymères.

Dans la première partie du résumé, nous allons évaluer le potentiel de la technique de microfaisceau de rayons-X pour l'étude morphologique des cristaux lamellaires tordus. Ensuite, nous allons introduire notre modèle moléculaire expliquant l'origine de la torsion lamellaire lors de la croissance : ce modèle sera confronté avec les modèles de la littérature. Enfin, nous allons discuter les résultats d'une simulation sur ordinateur que nous avons faite pour analyser la forme des cristaux lamellaires dans l'espace 3D.

VI.4 Etude des sphérolites à bandes avec un microfaisceau de rayons X.

Pour comprendre l'origine de la torsion lamellaire dans le poly(triméthylène téréphthalate) (PTT), nous avons effectué une étude structurale approfondie en utilisant un microfaisceau de rayons-X. L'objectif de cette étude est tout d'abord de vérifier si les deux postulats principaux du modèle de *Keith* et *Padden* (*KP*) sont applicables au cas des cristaux de PTT ou si d'autres modèles peuvent aussi être valides tels que par exemple le modèle de dislocation vis géantes.

Le premier postulat du modèle *KP* admet que la torsion des cristaux lors de la croissance est une conséquence d'action transitoire des contraintes surfaciques qui apparaissent sur les plans basales des lamelles. L'origine de la torsion lamellaire dans les contraintes mécaniques est donc préférée par rapport au modèle des dislocations vis isochirlales géantes. Le second postulat suppose que la torsion lamellaire est provoquée par l'encombrement stérique différent des plis de chaînes se trouvant sur les deux surfaces basales de la lamelle. Cela est dû à l'inclinaison des chaînes en état cristallin (les « stems ») par rapport à la normale de la surface lamellaire. Il est à noter que seule l'inclinaison des stems dans le plan perpendiculaire à l'axe de croissance lamellaire est importante dans l'apparition des contraintes surfaciques.

Une conséquence directe du premier postulat du modèle *KP* est que le sens de la torsion lamellaire doit être différent pour la croissance cristalline dans la direction positive et négative par rapport au germe initial. Cela s'explique par la chiralité de la lamelle induite suite à l'inclinaison des stems. Il est donc facile à démontrer que, dans ce cas de figure, le germe initial peut être également considéré comme le centre de symétrie de l'objet.

Le système étudié dans ce travail présente un excellent moyen pour vérifier les postulats du modèle *KP* en comparant la chiralité des lamelles tordues avec l'inclinaison des stems. A cette fin, l'orientation de la maille a été déterminée pour les films de PTT cristallisés à partir de l'état fondu dans la gamme de températures comprises entre 170°C et 200°C. L'angle d'inclinaison des stems a été calculé à partir de la distance radiale séparant les maxima des pics équatoriaux et celui du signal SAXS après normalisation par la période de torsion.

VI.4.1 Le sens de torsion et la polarité de l'axe de croissance des cristaux lamellaires

Nous avons démontré que le microfaisceau de rayons X est un outil adéquat pour explorer la microstructure des lamelles tordues avec une résolution spatiale suffisante. Il est important à noter que cette technique permet d'étudier des échantillons massiques tels que par exemple des films de PTT autosupportés de plusieurs dizaines de microns en épaisseur. Lors d'un balayage radial au sein d'un sphérolite avec un microfaisceau, la direction de la croissance cristalline dominante peut être assimilée à l'axe de torsion des lamelles. A partir de nos mesures avec le microfaisceau, nous avons trouvé que les pics de diffraction de la maille triclinique de PTT se succèdent périodiquement sur les clichés de diffraction en fonction de la distance. Cela indique que la torsion lamellaire est strictement uniforme et régulière. Cette observation est plus en accord avec le modèle expliquant la torsion comme résultat des contraintes surfaciques qu'avec celui des dislocations vis géantes.

En utilisant la construction de la sphère d'*Ewald*, le sens des hélicoïdes lamellaires peut être déterminé à partir de déphasage entre les maxima symétriques de la même réflexion équatoriale. Grâce à cette possibilité, nous avons trouvé que les lamelles ayant des sens opposés de torsion sont parfois présentes au sein du même sphérolite. Néanmoins, les hélicoïdes ayant le même sens de torsion sont typiquement groupés en secteurs sphérolitiques et présentent des corrélations à longue portée le long du rayon sphérolitique. En analysant la largeur des pics en fonction de l'angle azimuthal ou de l'angle de la fibre, nous avons proposé un modèle complet de la lamelle tordue dans l'espace directe et réciproque. Grâce à la symétrie basse de la maille de PTT (maille triclinique avec le groupe de symétrie P-1), il est possible de distinguer les vecteurs de croissance cristalline ayant les signes positif et négatif. Cette distinction importante pour notre analyse n'est pas faisable pour les cristaux de symétries plus hautes comme par exemple le PE qui a une maille orthorhombique.

Nous avons observé que les polymères achiraux comme par exemple le PTT ne sont en fait pas indifférents à l'inversion du sens de la torsion lamellaire. Cette dernière est donc toujours accompagnée par un changement de signe du vecteur de croissance cristalline. Nos résultats sont en accord avec le premier postulat du modèle *KP* stipulant que l'inversion du sens de la torsion lamellaire est corrélée avec la polarité de l'axe de croissance. En se basant sur ces observations, nous pouvons introduire une paire des paramètres chiraux indépendants, à savoir l'axe de croissance positive (***G***) ou négative (-

G), ainsi que le sens d'hélice gauche (*L*) ou droite (*R*). Les paramètres chiraux qui décrivent l'état des hélicoïdes lamellaires de PTT formées dans l'intervalle de températures $\mathbf{B_I}$ sont donc (***G*** / *L*) or (***-G*** / *R*).

VI.4.2 Mesure de l'angle d'inclinaison des chaînes dans des lamelles cristallines pour des polyméres semicristallins en volume

Le balayage avec un microfaisceau le long du rayon sphérolitique correspond exactement à la géométrie des mesures cristallographiques conventionnelles où l'échantillon est incliné aux différents angles par rapport au faisceau incident : La microstructure de PTT peut donc être étudiée dans le volume en combinant les données SAXS et WAXS. Ainsi l'inclinaison des « stems » cristallins de PTT a été déterminée pour les films autosupportés de plusieurs dizaines de microns en épaisseur. Ils sont inclinés de 4 deg (déviation standard inférieure à 2 deg) dans la direction positive de **b***.

A notre connaissance, c'est la première fois que l'orientation des chaînes dans le cristal a été déterminée pour un échantillon isotrope volumineux.

VI.5 Torsion lamellaire en fonction de température de cristallisation

VI.5.1 Torsion lamellaire et régimes de croissance cristalline

Le comportement de torsion lamellaire dans le PTT a été étudié en fonction de la température de cristallisation. Trois régimes de torsion lamellaire notés $\mathbf{B_I}$, $\mathbf{B_{II}}$ et $\mathbf{B_{III}}$ ont été identifiés. La température de cristallisation de 140°C marque le début de torsion lamellaire (noté ici comme $\mathbf{B_o}$) où les sphérolites de PTT deviennent annelés. Cette transition entre les sphérolites classiques vers les sphérolites à bandes coïncide avec un changement du régime de cristallisation de type **III → II**. Cette dernière observation est en accord avec l'hypothèse de *Keith* et *Padden* concernant les contraintes surfaciques considérées comme l'origine de la torsion lamellaire. Ainsi la cristallisation dans le régime **III** procède essentiellement par ajout des germes sur la surface cristalline préformée car la vitesse de propagation est inférieure par rapport à la vitesse de nucléation. Dans ce cas, les contraintes surfaciques telles que décrites dans le modèle *KP* ne peuvent pas avoir lieu, et donc les cristaux lamellaires ne peuvent pas se tordre lors de croissance.

VI.5.2 Inversion de la chiralité

Dans l'intervalle de températures $\mathbf{B_I}$, la période de torsion diverge avec la température de cristallisation selon une loi de puissance d'ordre deux. A la température de 178.5°C désignée ici comme $\mathbf{B_i}$ (le "i" venant de l'inversion), la période de torsion lamellaire atteint des valeurs pratiquement infinies, ce qui signifie que les cristaux lamellaires sont essentiellement plans. A ce point particulier, les contraintes surfaciques s'éteignent complètement, et nous observons une inversion du sens de la torsion lamellaire. Les paramètres chiraux des hélicoïdes lamellaires de PTT au-dessus du point $\mathbf{B_i}$ ont été identifiés comme ($\boldsymbol{G}$ / R) et ($\boldsymbol{-G}$ / L). Il en résulte que les lamelles formées dans les intervalles de températures $\mathbf{B_I}$ et $\mathbf{B_{II}}$ ont la chiralité opposée.

VI.5.3 L'inclinaison des stems cristallins par rapport à la torsion lamellaire: le premier postulat du modèle de Keith et Padden

Nous avons démontré que l'inclinaison globale des stems cristallins dans la lamelle (c. à d. l'inclinaison du paramètre **c** de la maille dans le plan perpendiculaire à l'axe de croissance cristalline) ne varie pratiquement pas en fonction de température de

cristallisation. Nous pouvons donc en déduire que **l'inclinaison des stems n'affecte ni l'intensité ni le sens de la torsion lamellaire**. Cette dernière conclusion met en question le second postulat du modèle *KP*. En essayant de rationaliser nos observations, nous avons proposé de corréler la torsion lamellaire non pas avec l'inclinaison globale de la chaîne mais avec celle des segments terminaux qui sortent de la surface basale. Dans le cadre de cette hypothèse, la variation de l'épaisseur cristalline avec la température de cristallisation doit impérativement affecter la direction dans l'espace de ces segments et donc la chiralité résultante de la lamelle.

De façon générale, le modèle *KP* fait surtout allusion à la morphologie et à la structure de PE. Néanmoins, si l'on considère en détail la conformation des chaînes de PE en état cristallin, elle est très différente par rapport aux chaînes de PTT. Tout d'abord, la chaîne de PE forme un *zig-zag* planaire tandis que le PTT adopte un *zig-zag* plus complexe dans lequel les séquences ayant le sens de l'hélice gauche et droite s'alternent. Donc globalement la chaine de PTT ne présente pas de chiralité et peut être assimilée par une conformation *zig-zag* ayant des projections différentes sur les plans **ac** et **bc** de la maille. Deuxièmement, les « stems » cristallins de PE et PTT sont très différents au niveau de leurs dimensions. Par exemple, le paramètre de maille **c** de PTT est environ sept fois plus grand que celui de PE tandis que l'épaisseur cristalline de ce dernier est typiquement quatre fois plus petite. Il s'en suit donc que dans le cas de PE la lamelle cristalline contient plusieurs dizaines de *zig-za*gs moléculaires tandis que pour le PTT ce nombre est toujours inférieur à trois. On peut donc supposer que pour le PE l'inclinaison locale du segment terminal n'aura aucune importance sur la structure car elle sera moyennée sur la distribution des cristaux en épaisseur. Par contre, ce paramètre peut être très important pour le PTT car chaque segment représente plus de 20% de l'épaisseur cristalline typique. Ainsi même si la largeur réduite de distribution des cristaux en épaisseur est de l'ordre de 10%, nous allons retrouver les mêmes segments terminaux sur la surface basale des lamelles.

Afin de se faire une idée sur les contraintes mécaniques qui agissent sur la surface lamellaire, nous avons corrélé la période de la torsion lamellaire avec l'épaisseur cristalline. Dans le cadre d'un modèle mécanique très simple où la période de torsion est proportionnelle à l'épaisseur lamellaire au carré, nous avons évalué l'intensité des contraintes mécaniques. Nous avons observé donc que dans la gamme des épaisseurs cristallines comprises entre 3.1 et 3.5 nm, l'intensité des contraintes décroit drastiquement marquant ainsi le point d'inversion $\mathbf{B_i}$. Au-dessus de cet intervalle de températures, les

contraintes changent de signe mais n'évoluent plus beaucoup au niveau de leur valeur absolue. Ce résultat montre que dans la considération du comportement de torsion, on ne peut pas supposer que les contraintes présentent une fonction lente de l'épaisseur lamellaire.

Le comportement de torsion lamellaire dans le PTT a été aussi comparé avec celui prédit par le model de génération des dislocations vis géants. Dans le cadre de ce modèle décrivant la génération des dislocations comme des fluctuations thermiques, l'apparition permanente des nouvelles dislocations isochirales donne lieu à une torsion macroscopique de la lamelle. Ce modèle prédit la dépendance linéaire du logarithme de la période de torsion en fonction de l'épaisseur lamellaire au cube. Il est clair que ce modèle n'est pas capable d'expliquer la décroissance de la période de torsion observée dans la gamme de températures $\mathbf{B_{II}}$. Nous pouvons donc conclure que l'idée des dislocations géantes successives n'est pas appropriée pour le cas de PTT.

VI.5.4 Modèle moléculaire expliquant l'origine des contraintes surfaciques

Dans l'hypothèse que la surface lamellaire est composée essentiellement des segments flexibles de la chaîne de PTT, nous avons élaboré un modèle moléculaire qui met en relation l'inclinaison des segments terminaux de la lamelle avec son épaisseur. Puisque toute la variation de l'épaisseur lamellaire observée expérimentalement correspond à la longueur de deux segments flexibles de la chaîne, l'inversion du sens de la torsion lamellaire trouve une explication. Dans les intervalles de température $\mathbf{B_I}$ et $\mathbf{B_{II}}$ le cristal contient un nombre paire des segments rigides ce qui crée des distributions des contraintes mécaniques sur les deux surfaces basales qui sont liées par l'opération de symétrie centrale.

De plus, notre modèle explique la nature du point de singularité à haute température, c'est-à-dire le point $\mathbf{B_{sp}}$ qui se trouve à peu près à 202.5°C où la période de torsion chute d'environ de moitié. A cette température, l'épaisseur du cristal s'approche à la situation où deux segments rigides doivent se trouver au voisinage de la surface lamellaire. Pour éviter cette situation qui n'est pas favorable, le cristal peut incorporer un segment rigide en plus, ce qui changera la symétrie des distributions des contraintes sur les surfaces basales de la lamelle. A son tour, ce changement résulte en une diminution de la période de torsion. En outre, cette transition est accompagnée par une dégradation de l'orientation radiale des

axes de croissance rapide (c'est à dire l'axe **a** de la maille) suite à un « déboitement » des hélicoïdes lamellaires.

VI.5.5 La mémoire structurale transmise lors du branchement lamellaire

Enfin, nous avons utilisé les sphérolites à bandes de PTT pour identifier la mémoire structurale qui pourrait être transmise au cours de la croissance sphérolitique. En faisant une expérience lors de laquelle la température de cristallisation a été changé brusquement en passant par le point de singularité $\mathbf{B_i}$, nous sommes arrivés à la conclusion que les lamelles gardent l'information sur la polarité de leur axe de croissance et non pas sur le sens de la torsion. Cela signifie que le branchement lamellaire se procède en accord avec le registre cristallin et que l'image conventionnelle de la morphogénèse sphérolitique impliquant le branchement non-cristallographique des lamelles doit être rejetée.

VI.6 Simulation sur ordinateur de la diffraction à partir des lamelles tordues

Afin d'améliorer la compréhension de la morphologie des sphérolites à bandes et d'obtenir des informations supplémentaires sur la forme des lamelles dans l'espace 3D, nous avons utilisé la méthode de simulation de diffusion de rayons X introduite précédemment par *Ivanov* et *Luchnikov* pour le cas des lamelles contenant la maille triclinique de PTT. Dans nos simulations, nous avons reproduit quelques traits des clichés de diffraction expérimentaux tels que l'élargissement des pics en fonction de l'angle azimuthal et de l'angle de la fibre, ainsi que la séquence d'apparition des pics et leur forme. Nous avons démontré que le profil des lamelles tordues n'est pas une section linéaire mais peut présenter une forme plus complexe telle que par exemple la forme en « *S* ». En outre, nous avons trouvé que la largeur des pics équatoriaux en fonction de l'angle de la fibre ne varie pas avec la température de cristallisation, ce qui signifie que la largeur des lamelles tordues augmente proportionnellement avec leur période de torsion.